



Assessment and Improvement of Fission Product Transport Predictions of Particle Fuel in BISON

September 2022

Technical Report

Aysenur Toptan¹, Wen Jiang¹, Gyanender Singh¹, Som
Dhulipala¹, Yifeng Che¹, Jason D. Hales¹, and Stephen R.
Novascone¹

¹Idaho National Laboratory



*INL is a U.S. Department of Energy National Laboratory
operated by Battelle Energy Alliance, LLC*

DISCLAIMER

This information was prepared as an account of work sponsored by an agency of the U.S. Government. Neither the U.S. Government nor any agency thereof, nor any of their employees, makes any warranty, expressed or implied, or assumes any legal liability or responsibility for the accuracy, completeness, or usefulness, of any information, apparatus, product, or process disclosed, or represents that its use would not infringe privately owned rights. References herein to any specific commercial product, process, or service by trade name, trade mark, manufacturer, or otherwise, does not necessarily constitute or imply its endorsement, recommendation, or favoring by the U.S. Government or any agency thereof. The views and opinions of authors expressed herein do not necessarily state or reflect those of the U.S. Government or any agency thereof.

Assessment and Improvement of Fission Product Transport Predictions of Particle Fuel in BISON

Technical Report

Aysenur Toptan¹, Wen Jiang¹, Gyanender Singh¹, Som Dhulipala¹, Yifeng Che¹, Jason D. Hales¹, and Stephen R. Novascone¹

¹Idaho National Laboratory

September 2022

**Idaho National Laboratory
Computational Mechanics and Materials Department
Idaho Falls, Idaho 83415**

<http://www.inl.gov>

**Prepared for the
U.S. Department of Energy
Office of Nuclear Energy
Under U.S. Department of Energy-Idaho Operations Office
Contract DE-AC07-05ID14517**

Page intentionally left blank

ABSTRACT

The U.S. Department of Energy's Nuclear Energy Advanced Modeling and Simulation (NEAMS) program aims to develop predictive capabilities by applying computational methods to the analysis and design of advanced reactor and fuel cycle systems. This program has been providing engineering-scale support for the development of BISON, a high-fidelity and high-resolution fuel performance tool.

This study was motivated by the need to incorporate more physics-based models in BISON in order to foster tri-structural isotropic (TRISO) applications. This document details the integration of new modeling capabilities in BISON, including (1) development of pyrolytic carbon (PyC) and silicon carbide (SiC) layer anisotropic thermal and mass transport capabilities, (2) verification of the mass diffusion solution in TRISO modeling, (3) calibration of fission product diffusivity using Advanced Gas Reactor (AGR) experiments, (4) improved fission product release modeling by developing compact diffusion modeling capabilities, and (5) documentation of accelerated failure analysis on the BISON website. Improvements made to the diffusion models and parameters were documented and validated against AGR-1 and -2 experiment data.

ACKNOWLEDGMENT








This report was authored by a contractor of the U.S. Government under contract no. DE-AC07-05ID14517. Accordingly, the U.S. Government retains a non-exclusive, royalty-free license to publish or reproduce the published form of this contribution, or allow others to do so, for U.S. Government purposes.

This research made use of the resources of the High Performance Computing Center at Idaho National Laboratory (INL), which is supported by the Office of Nuclear Energy of the U.S. Department of Energy and the Nuclear Science User Facilities under contract no. DE-AC07-05ID14517.

DECLARATION OF COMPETING INTEREST

The authors declare that they have no known competing financial interests or personal relationships that could appear to have influenced the work reported in this technical report.

ORCID

Yifeng Che		0000-0003-1841-9937
Som Dhulipala		0000-0002-0801-4250
Jason D. Hales		0000-0003-0836-0476
Wen Jiang		0000-0001-6978-9159
Stephen R. Novascone		0000-0002-3938-4326
Gyanender Singh		0000-0003-1828-4438
Aysenur Toptan		0000-0003-4250-6336

CONTENTS

ABSTRACT	iv
LIST OF FIGURES	viii
LIST OF TABLES	xi
List of Listings	xi
ACRONYMS	xii
I INTRODUCTION	2
II ANISOTROPIC THERMAL AND MASS TRANSPORT	4
II-A Anisotropic Thermal Behavior	4
II-B Anisotropic Diffusion	11
II-C Summary	13
III VERIFICATION OF THE MASS DIFFUSION SOLUTION	14
III-A Background	14
III-B Exercise 1: In-pile Production, Transport, and Decay of Short-lived Isotopes	16
III-C Exercise 2: In-pile Production and Transport of a Stable Fission Product	16
III-D Exercise 3: Out-of-pile Conditions for the Transport and Decay of Preexisting Isotopes	18
III-E Summary	19
IV DIFFUSION COEFFICIENT ESTIMATES BASED ON THE AGR-1 AND -2 INTEGRAL RELEASE EXPERIMENTS	20
IV-A Calibration Technique	21
IV-B AGR-1 and -2 Experiments	22
IV-C Calibration Settings	28
IV-D Results & Discussion	32
IV-E Summary	54
V EFFECTIVE DIFFUSIVITY COEFFICIENT	55
V-A Methods	55
V-B Results & Discussion	57
V-C Summary	60
VI COMPACT DIFFUSION MODELING	61
VI-A Convergence Study on Point Source Calculation Using Dirac Kernels	61
VI-B Two-Way Coupling between TRISO Particles and the Matrix	62
VI-C TRISO Diffusion Modeling with Discontinuous Galerkin	65
VI-D Sorption Isotherm Implementation for AGR 3/4 Rings	69
VI-E AGR-1 Fission Product Release Calculation with Compact Modeling	72
VI-F Summary	72

VII	ACCELERATED STATISTICAL FAILURE ANALYSIS OF MULTI-FIDELITY TRISO	
MODELS		74
VII-A	Preliminaries	74
VII-B	Methods for Accelerated Failure Analysis	74
VII-C	Usage in BISON with Parallel Computing and BISON Website Documentation . .	78
VII-D	Results	82
VII-E	Summary	84
VIII	CONCLUSION	88
REFERENCES		89

LIST OF FIGURES

1	Thermal conductivity tensor components and their orientation in the local coordinate system. The k_{33} component's direction is into the plane of the TRISO figure.	5
2	Temperature distribution in the TRISO particle and fuel kernel for the aspherical case. . . .	6
3	Temperature distribution in the PyC layer for the aspherical particle.	7
4	Comparison of temperature profiles along the radial direction in an aspherical particle for cases involving isotropic and anisotropic thermal conductivities.	7
5	Variation in maximum radial stress with fluence in the IPyC, SiC, and OPyC layers of a spherical TRISO particle and an aspherical TRISO particle.	8
6	Variation in maximum tangential stress with fluence in the IPyC, SiC, and OPyC layers of a spherical TRISO particle and an aspherical TRISO particle.	9
7	Variation in Weibull failure probability with fluence in the IPyC and SiC layers of a spherical TRISO particle and an aspherical TRISO particle.	10
8	Comparison of the concentration of silver for its three different diffusivity values in the tangential direction	12
9	Comparison of the concentration of silver for its three different diffusivity values in the radial direction	12
10	Comparison of the analytical and the computed concentration, release rate over birth rate, and fractional release as a function of dimensionless diffusion time, for the in-pile production, transport, and decay of short-lived isotopes.	17
11	Comparison of analytical and computed concentration, release-rate over birth-rate, and fractional release as a function of dimensionless diffusion time for in-pile production and transport of a stable fission product.	18
12	Comparison of analytical and computed concentration, release-rate, and fractional release as a function of dimensionless diffusion time for out-of-pile conditions for the transport and decay of pre-existing isotopes.	19
13	AGR-1 and -2 compacts at the end of irradiation as a function of burnup, fast neutron fluence, and time-and-volume averaged temperature	24
14	BISON-predicted release fractions using the IAEA-reported diffusion coefficients for Ag, Cs, and Sr are compared to the measured release fractions at the AGR-1 base irradiation with the intact particles.	25
15	BISON-predicted release fractions using the IAEA-reported diffusion coefficients for Cs and Sr are compared to the measured release fractions at the AGR-1 base irradiation with the failed particles.	25
16	BISON-predicted release fractions using the IAEA-reported diffusion coefficients for Ag, Cs, and Sr are compared to the measured release fractions at the AGR-2 base irradiation with the intact particles.	26
17	BISON-predicted release fractions using the IAEA-reported diffusion coefficients for Cs and Sr are compared to the measured release fractions at the AGR-2 base irradiation with the failed particles.	27
18	Heating plan for AGR-1 safety test.	27

19	BISON-predicted release fractions using the IAEA-reported diffusion coefficients for Ag, Cs, and Sr are compared to the measured release fractions during the AGR-1 safety heating tests with the intact particles.	29
20	BISON-predicted release fractions using the IAEA-reported diffusion coefficients for Ag, Cs, Kr, and Sr are compared to the measured release fractions during the AGR-1 safety heating tests with the failed particles.	29
21	BISON-predicted release fractions using the IAEA-reported diffusion coefficients for Ag, Cs, Kr, and Sr are compared to the measured release fractions during the AGR-2 safety heating tests with the intact particles.	30
22	BISON-predicted release fractions using the IAEA-reported diffusion coefficients for Ag, Cs, Kr, and Sr are compared to the measured release fractions during the AGR-2 safety heating tests with the failed particles.	30
23	Ag diffusion coefficients in the kernel.	33
24	Ag diffusion coefficients in PyC.	34
25	Ag diffusion coefficients in SiC.	35
26	Comparison of the measured and the computed Ag release fractions during the AGR-1 base irradiation with intact particles.	36
27	Comparison of the measured and the computed Ag release fractions during the AGR-2 base irradiation of intact particles.	36
28	Comparison of measured and computed Ag release fractions during the safety heating tests with intact particles.	38
29	Comparison of measured and computed Ag release fractions during the safety heating tests conducted on the failed particles.	38
30	Cs diffusion coefficients in the kernel.	39
31	Cs diffusion coefficients in PyC.	40
32	Cs diffusion coefficients in SiC.	41
33	Comparison of the measured and the computed Cs release fractions during the base irradiation with intact particles.	42
34	Comparison of the measured and the computed Cs release fractions during the safety heating tests with intact particles.	43
35	Comparison of measured and computed Cs release fractions during the base irradiation with failed particles.	43
36	Comparison of measured and computed Cs release fractions during the safety heating tests with failed particles.	44
37	Sr diffusion coefficients in the kernel.	45
38	Sr diffusion coefficients in PyC.	46
39	Sr diffusion coefficients in SiC.	47
40	Comparison of the measured and the computed Sr release fractions during the base irradiation with intact particles	48
41	Comparison of the measured and the computed Sr release fractions during the safety heating tests with intact particles.	49
42	Comparison of the measured and the computed Sr release fractions during the base irradiation with failed particles.	49

43	Comparison of the measured and the computed Sr release fractions during the safety heating tests with failed particles.	50
44	Kr diffusion coefficients in the kernel.	51
45	Kr diffusion coefficients in PyC.	52
46	Kr diffusion coefficients in SiC.	53
47	3-D constructed computational domain.	56
48	Concentration profile contours obtained from the unidirectional diffusion process in x-, y-, and z-direction at fixed volume fraction for $\alpha < 1$	58
49	Concentration profile contours obtained from the unidirectional diffusion process in x-, y-, and z-direction at fixed volume fraction for $\alpha > 1$	59
50	D_e/D_1 predictions with respect to v_1 for $\alpha < 1$ and $\alpha > 1$	60
51	Convergence studies for the smooth test problems.	62
52	Convergence studies for the non-smooth test problems.	63
53	Convergence studies for the non-smooth test problems using a graded mesh.	64
54	Convergence rates for the 2-D non-smooth test problem for the domain away from the point.	64
55	BISON pebble modeling illustration.	65
56	BISON compact modeling with two-way coupling.	66
57	Particle temperature and SiC stress history.	67
58	Three compact modeling.	67
59	Compacts with packing fractions of 25, 40, and 48%. The particle locations are directly read from x-ray computed tomography measurement.	68
60	Particle species diffusion through the matrix. Top row: monolithic approach; bottom row: multi-app approach.	69
61	Species release from the matrix with different particle diffusivities.	70
62	Cesium concentration along the radial direction at time = 6, 20, 100, and 400 days.	70
63	AGR 3/4 BISON representation. The four regions of the BISON model are the fuel compact, matrix ring, graphite ring, and graphite sink.	71
64	Radial (r in m) cesium concentration profile of the COMSOL benchmark, as compared to BISON.	72
65	Silver release of AGR-1 compacts.	73
66	Cesium and strontium release of AGR-1 intact compacts.	73
67	Schematic of the AIS method for accelerated failure probability estimation.	75
68	Schematic of the PSS method for accelerated failure probability estimation.	76
69	Pair grid plot of failure-causing input parameter distributions for TRISO Model 1 (1-D), using the PSS and MC methods.	85
70	Pair grid plots of the SiC failure conditional on IPyC distributions of failure-causing input parameters for TRISO Model 1, in light of PSS for 1-D and 2-D models.	87

LIST OF TABLES

I	Mass diffusion coefficients	20
II	AGR-1 safety tests	28
III	Summary of the data points from the AGR-1 and -2 experiments.	31
IV	Correspondence between elastic and conductive problems	55
V	Recommended analytical methods for the ETC	56
VI	Input parameters for the four TRISO models considered.	82
VII	Irradiation temperatures in the nuclear reactor for the four TRISO fuel models.	83
VIII	Failure probabilities, COVs, and number of 1-D TRISO evaluations for four different statistical methods across four models.	84
IX	Failure probabilities, COVs, and number of 2-D TRISO evaluations for the PSS and Weibull methods across four models.	86

LISTINGS

1	Main input file block for transferring the QoI from the sub file to the main file.	78
2	The <code>Samplers</code> block in the main input file for defining the AIS method.	79
3	The <code>Reporters</code> block in the main input file for using the AIS method.	80
4	The <code>Executioner</code> block in the main input file for using the AIS method.	80
5	The <code>Samplers</code> block in the main input file for defining the PSS method.	80
6	The <code>Reporters</code> block in the main input file for using the PSS method.	81
7	The <code>Executioner</code> block in the main input file for using the PSS method.	81
8	The <code>WeibullFailureProbability</code> postprocessor block in the sub input file for using the Weibull approach. The main file will be a Monte Carlo driver that randomizes the TRISO geometry and material parameters.	82

ACRONYMS

Ag	silver
AGR	Advanced Gas Reactor
AIS	Adaptive Importance Sampling
CCCTF	Core Conduction Cooldown Test Facility
COV	coefficient of variation
CRP-6	Coordinated Research Program
Cs	cesium
CVD	chemical vapor deposition
CG	continuous Galerkin
D-EMT	differential effective medium theory
DG	discontinuous Galerkin
DOE	U.S. Department of Energy
DTF	designed-to-failed
EDC	effective diffusivity coefficient
EMT	effective medium theory
ETC	effective thermal conductivity
Eu	europium
FACS	Fuel Accident Condition Simulator
FCC	face-centered cubic
FEA	finite-element analysis
FEM	finite-element method
FIMA	fissions per initial metal atom
FP	fission product
HC	hexagonal close
IAEA	International Atomic Energy Agency
INL	Idaho National Laboratory
IPyC	inner PyC
Kr	krypton
LLS	lower-length scale
MCMC	Markov Chain Monte Carlo
MC	Monte Carlo
MOOSE	Multiphysics Object-Oriented Simulation Environment
M&S	modeling and simulation
NEAMS	Nuclear Energy Advanced Modeling and Simulation
OLS	ordinary least square
OPyC	outer PyC
ORNL	Oak Ridge National Laboratory
PARFUME	Particle Fuel Model
PDE	partial differential equation
PIE	post-irradiation examination
PSS	parallel subset simulation

PyC	pyrolytic carbon
QoI	quantity of interest
R/B	release-rate over birth-rate
RHS	right-hand side
SC	simple cubic
SiC	silicon carbide
SNL	Sandia National Laboratories
Sr	strontium
TAVA	time-average volume-average
TRISO	tri-structural isotropic
UCO	uranium oxycarbide
UO₂	uranium dioxide
1-D	one-dimensional
2-D	two-dimensional
3-D	three-dimensional

I. INTRODUCTION

The TRISO capability originally implemented in BISON assumed isotropy for certain material models (e.g., the elasticity, thermal, and mass transport models for PyC and SiC). However, as reported in Evans et al. (2022), TRISO layers can exhibit anisotropic thermophysical properties as a result of the manufacturing process. The ability to account for anisotropic elastic properties was already added (Jiang et al., 2022), and the present work extends this capability to account for anisotropic thermal and mass properties in BISON. This capability to account for anisotropy in thermal and mass transport is demonstrated in Section II, using example problems involving both spherical and aspherical TRISO particles.

A one-dimensional (1-D) model is typically used to predict fission product diffusion in TRISO particles. Code verification must be performed to ensure that BISON can generate accurate predictions. In this study, the code verification process was applied to 1-D spatiotemporal problems that exercise a partial differential equation (PDE) governing the conservation of fission product species. Numerical experiments were performed in BISON to evaluate its predictive capability under various TRISO reactor conditions (see Section III).

BISON comparisons to AGR-1 and -2 post-irradiation examination (PIE) data closely match the Particle Fuel Model (PARFUME) results, yet both codes tend to overpredict the experimental data. There is a clear need for data calibration to be optimized for improved release predictions. This study aims to investigate the availability and reliability of diffusion coefficients for key radioactive species in the particle. The diffusion coefficients were estimated based on the data obtained in the AGR-1 and -2 experiments during both base irradiation and safety heating tests. The diffusion coefficients estimates, and the surveyed empirical coefficients of the key radioactive species in the kernel, PyC, and SiC layers are discussed in Section IV.

The effective diffusivity coefficient (EDC) is needed to simulate fission product diffusion through a homogenized compact. In this study, we extended our previous studies (Toptan et al., 2021) in order to examine the validity of models for making effective diffusivity calculations, obtained from the Fickian diffusion. These numerical results establish the regimes in which these analytical formulations can be applied with a high degree of confidence to the applications of interest, particularly in regard to estimation of EDC from the Fickian diffusion for the TRISO applications (see Section V).

The capability of modeling fission product diffusion in compacts via classical Monte Carlo (MC) was extended to enable two-way coupling between TRISO particles and the compact. In this method, particles are simplified as point sources in each compact. A convergence study was performed to assess the accuracy of point source calculations. At the particle level, a discontinuous Galerkin method was explored to ameliorate the solution oscillation associated with the large diffusivity contrasts across different layers in TRISO. The BISON compact modeling capability was applied to the modeling of AGR-1 and -3/4 experiments. For AGR-3/4, sorption isotherm conditions were implemented to account for the concentration jump across the different “rings” in a capsule. Using daily as-run irradiation conditions, the 1-D BISON model calculated the fission product concentration profiles across selected capsules’ rings and compared them to the measured PIE data. For AGR-1, fission product release was calculated using the compact diffusion modeling capability. Retention of the fission product species in a graphite compact was accounted for. Ultimately, BISON’s new prediction capability showed better agreement with the PARFUME results (see Section VI).

Recently implemented methods for conducting accelerated failure analysis of TRISO, their documentation on the BISON website, and application to the failure analysis of several 1-D and two-dimensional (2-D) models are all discussed in this report. Several examples were included to explain the usage of those new capabilities in regard to BISON TRISO statistical failure analysis (see Section VII).

II. ANISOTROPIC THERMAL AND MASS TRANSPORT

The manufacturing process for TRISO particles involves deposition of PyC and SiC layers onto fuel kernels via chemical vapor deposition (CVD) in fluidized beds. The hydrocarbons and SiC precursors decompose at high temperatures during the deposition process. The reactant gas mixture and temperature are carefully controlled to obtain the desired coating properties. The CVD process is known to produce polycrystalline material layers with crystallographic textures (López-Honorato et al., 2009; Meadows et al., 2009; Zhang et al., 2015). Due to this texture, the CVD-deposited layers can exhibit anisotropic thermophysical properties (Wang et al., 2018). A detailed discussion on the anisotropic properties of TRISO particles is presented in Evans et al. (2022).

These anisotropic properties may or may not significantly affect the stress state in the TRISO layers, and thus also affect the structural integrity of TRISO particles (Jiang et al., 2021b, 2022). To understand how anisotropy in the thermophysical properties of TRISO particles impacts the performance of TRISO fuel, the code must be able to account for the anisotropic material properties. Such a capability has been added (Jiang et al., 2021b), and the present work extends it to account for anisotropic thermal and mass transport properties in BISON. Although this capability is presented here in the context of TRISO fuel, it is widely applicable to other fuel forms and core components.

A. Anisotropic Thermal Behavior

Due to the crystallographic texture, the radial and tangential thermal conductivities can differ from each other. To incorporate this anisotropy in a TRISO particle, the thermal conductivity property should be defined as a second-order tensor whose components are the magnitudes of the thermal conductivity in the corresponding directions. In BISON, thermal conductivity k is represented as a rank two tensor:

$$\begin{bmatrix} k_{11} & k_{12} & k_{13} \\ k_{21} & k_{22} & k_{23} \\ k_{31} & k_{32} & k_{33} \end{bmatrix}, \quad (1)$$

where subscripts 1, 2, and 3 correspond to the vectors of orthonormal bases in the local coordinate system, which rotates according to layer orientation, as shown in Figure 1. In a local system, the off-diagonal elements of this tensor are zero. Since the solve is performed in a global coordinate system, the thermal conductivity tensor is rotated to obtain its components. In the global coordinate system, the off-diagonal components of the tensor can be non-zero. The model is capable of applying automatic differentiation if needed.

The capability to model anisotropic thermal behavior in BISON is demonstrated through an example problem in which the fuel performance of TRISO particles with both spherical and aspherical geometries is evaluated by considering two cases of PyC thermal conductivity: (1) isotropic thermal conductivity, with a value of 4 W/m-K, and (2) anisotropic thermal conductivity, with a value of 0.28 W/m-K in the radial direction and 11.5 W/m-K in the tangential direction, as per Wang et al. (2018). Two different operating conditions are also considered: the exterior surface of the TRISO particle is considered to be at 973 and 1273 K. The results of the analysis are shown in Figures 2–7. These results indicate that the anisotropic thermal properties of PyC layers significantly affect the temperature distribution in the TRISO particle; however, the impact on the structural integrity of TRISO particles appears insignificant. This example problem demonstrates BISON’s capability to model anisotropic thermal behavior, which can aid in understanding the extent of thermal anisotropy’s effect on fuel performance.

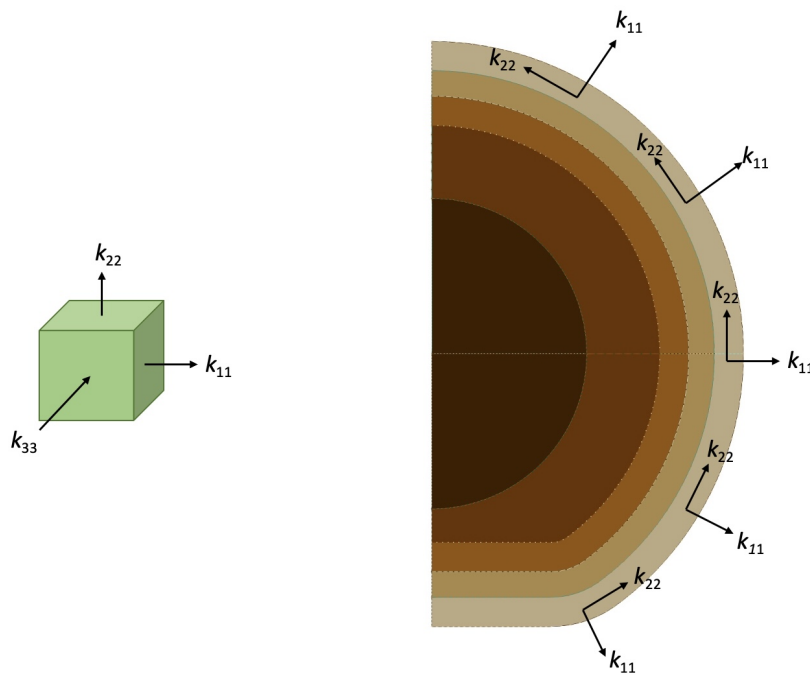


Fig. 1. Thermal conductivity tensor components and their orientation in the local coordinate system. The k_{33} component's direction is into the plane of the TRISO figure.

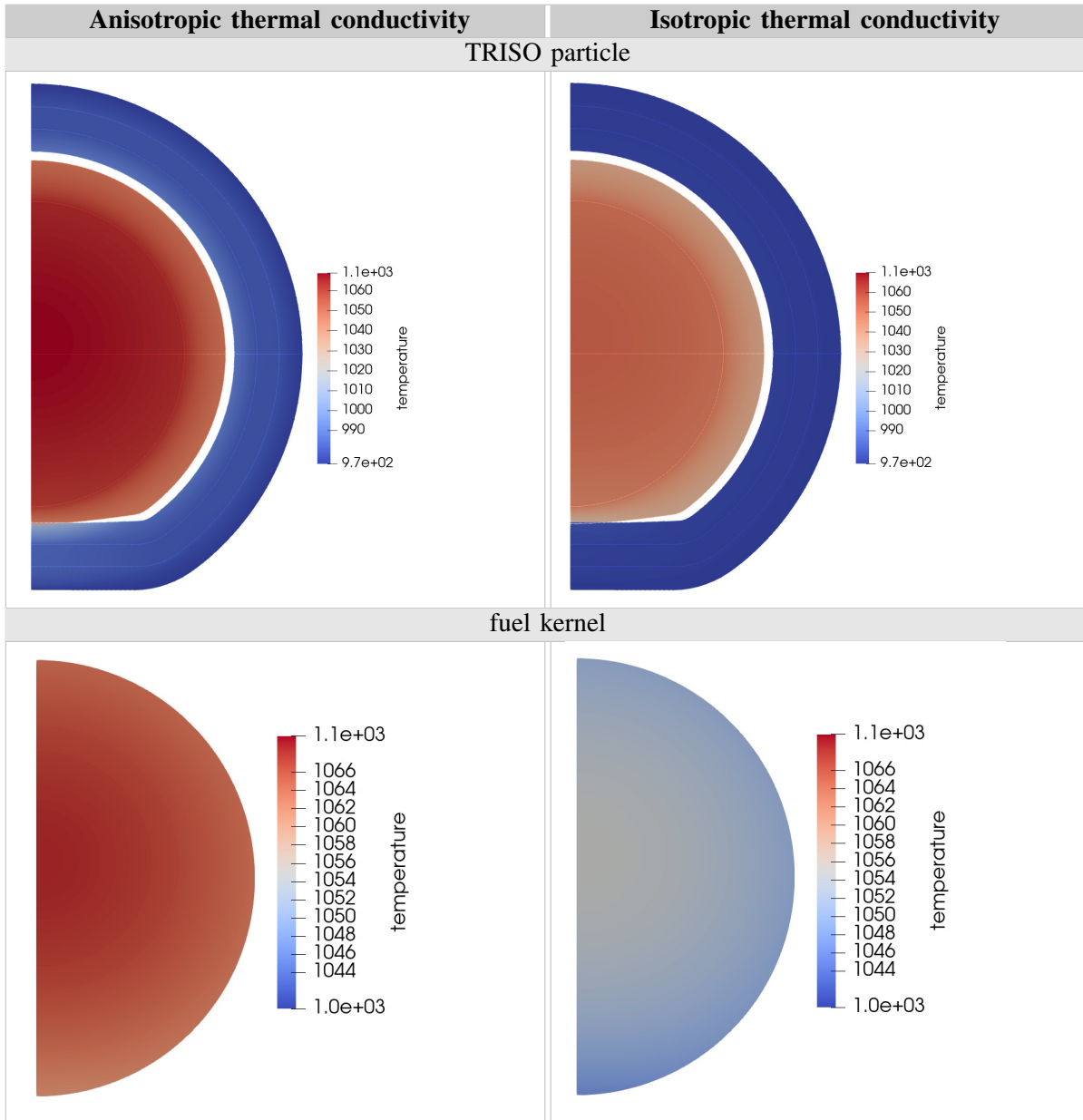


Fig. 2. Temperature distribution in the TRISO particle and fuel kernel for the aspherical case (units: Kelvin).

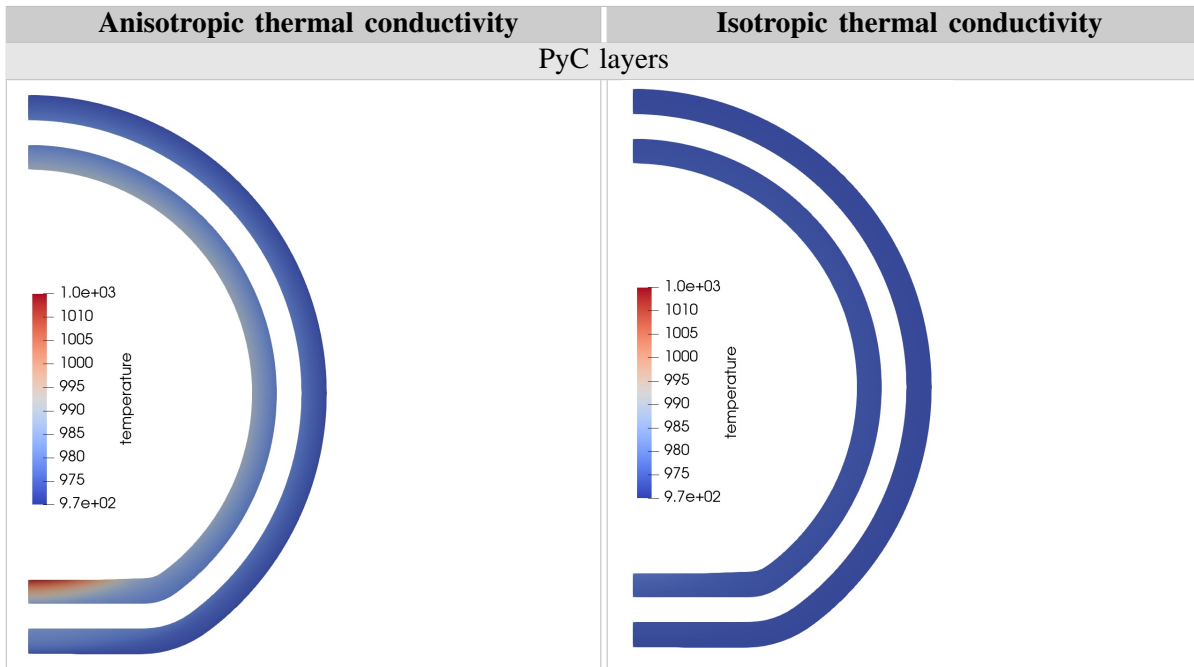


Fig. 3. Temperature distribution in the PyC layer for the aspherical particle (units: Kelvin).

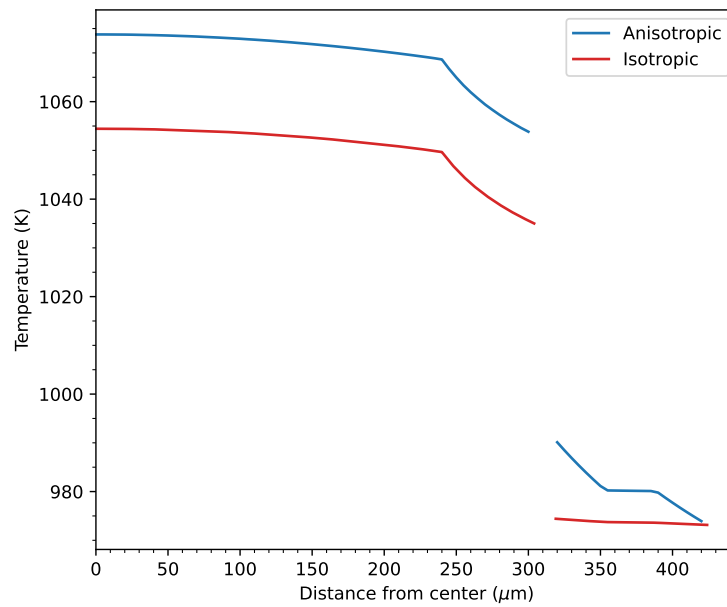


Fig. 4. Comparison of temperature profiles along the radial direction in an aspherical particle for cases involving isotropic and anisotropic thermal conductivities.

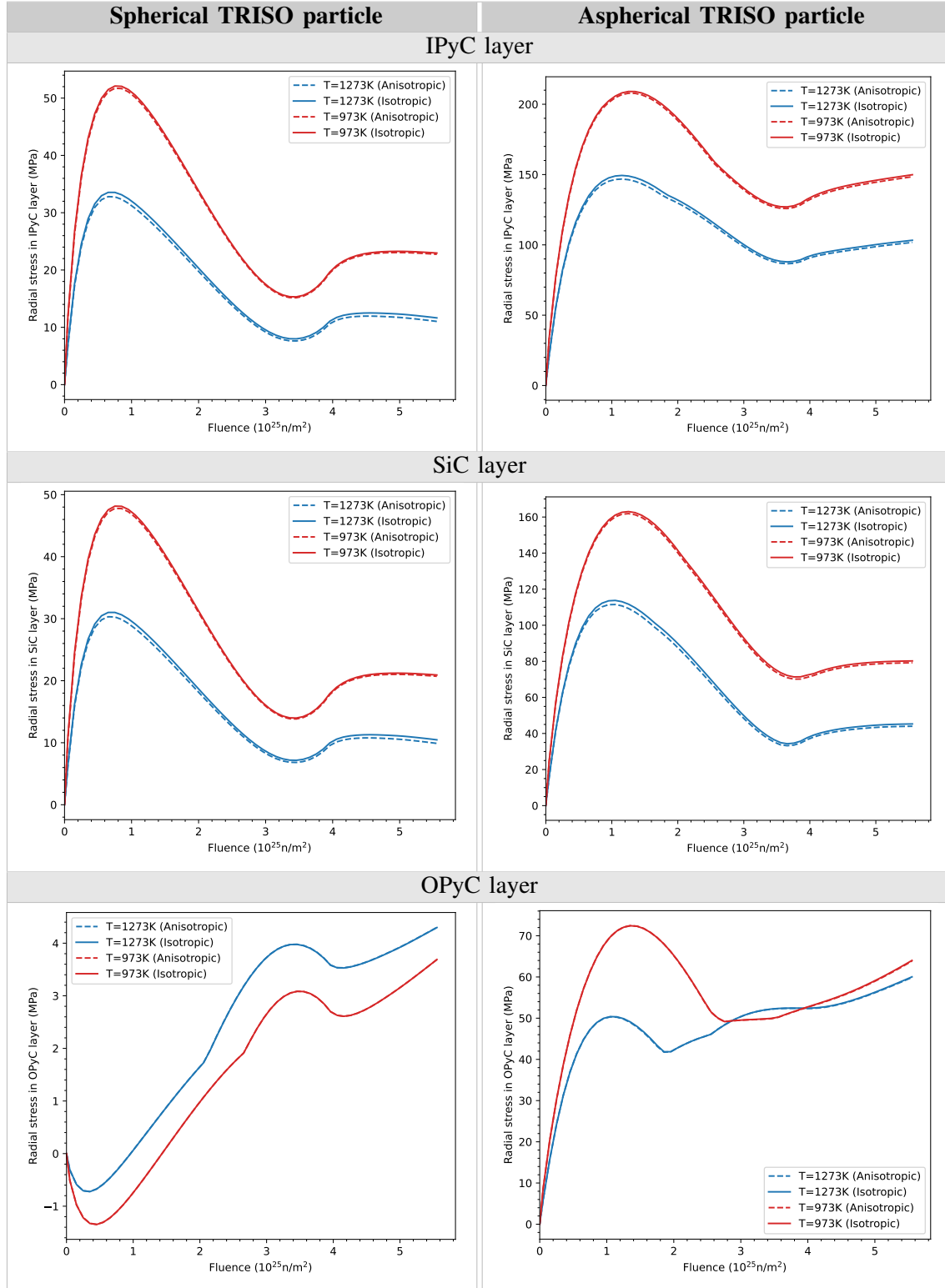


Fig. 5. Variation in maximum radial stress with fluence in the IPyC, SiC, and OPyC layers of a spherical TRISO particle (left column) and an aspherical TRISO particle (right column).

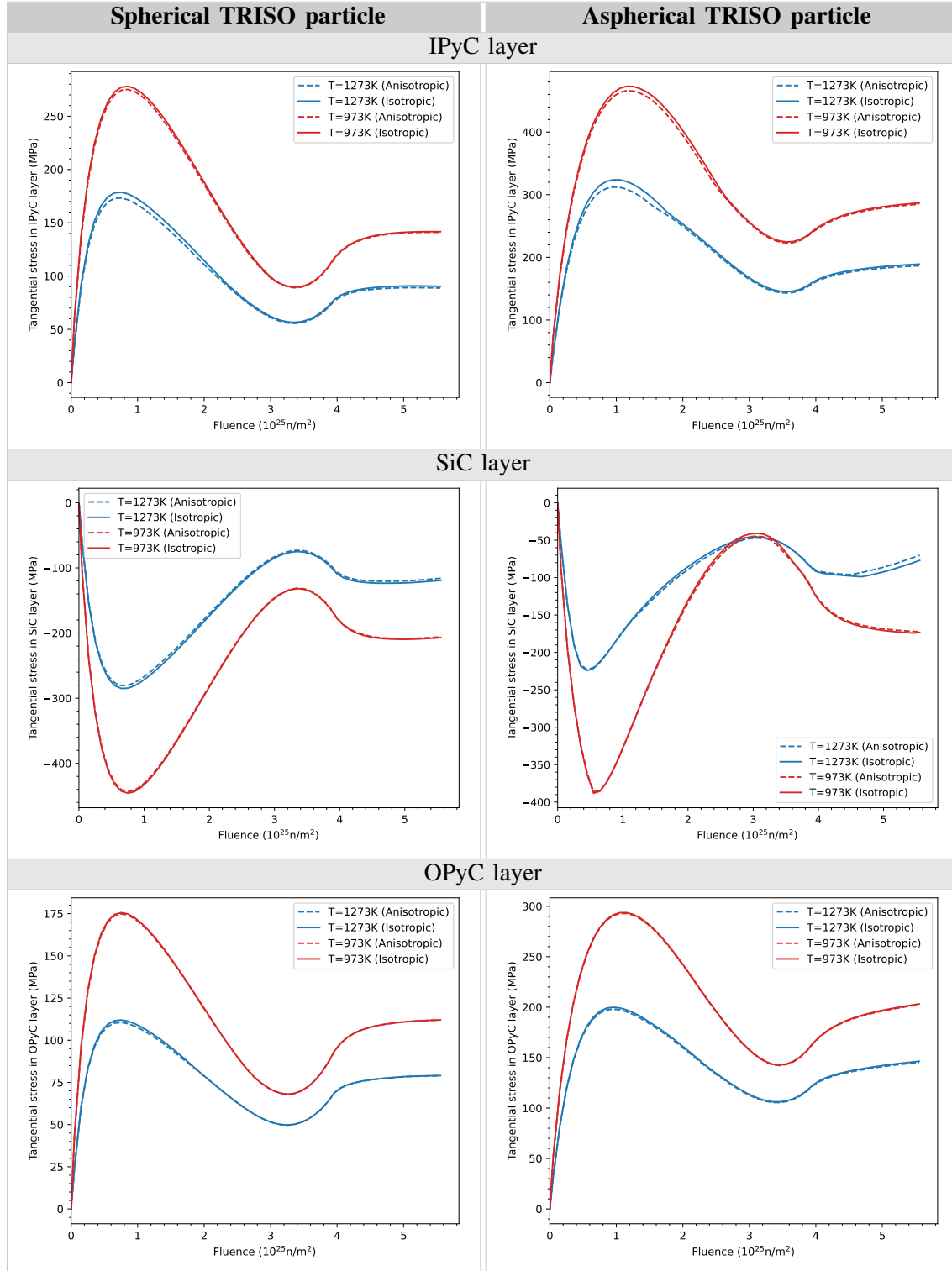


Fig. 6. Variation in maximum tangential stress with fluence in the IPyC, SiC, and OPyC layers of a spherical TRISO particle (left column) and an aspherical TRISO particle (right column).

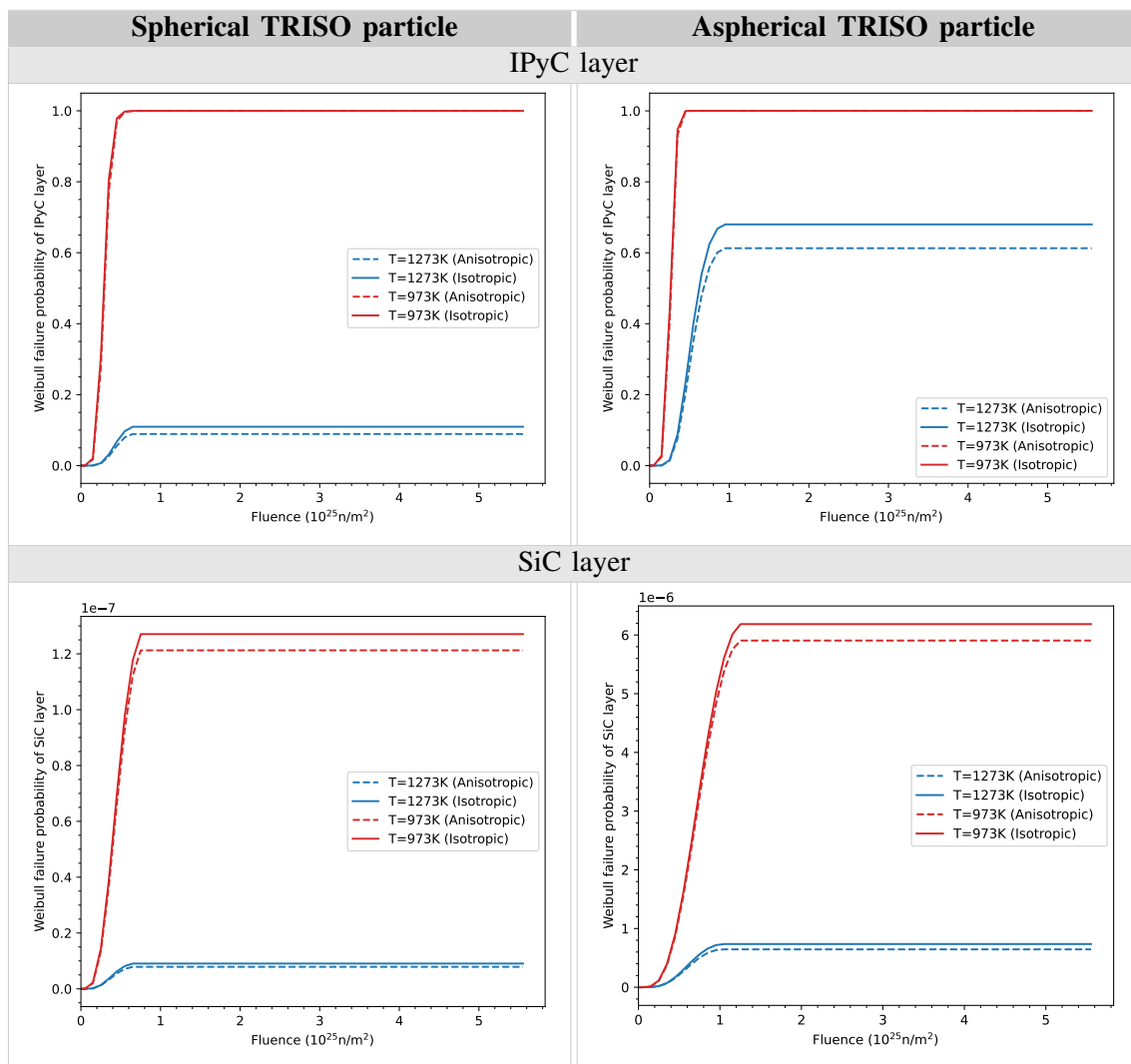


Fig. 7. Variation in Weibull failure probability with fluence in the IPyC and SiC layers of a spherical TRISO particle (left column) and an aspherical TRISO particle (right column).

B. Anisotropic Diffusion

As discussed earlier, the CVD process, which is used in manufacturing TRISO particles, can generate material layers featuring a crystallographic texture that may induce anisotropy in thermophysical properties. Thus, the capability to model anisotropic arrhenious diffusion was developed. As part of this effort, modeling of the anisotropic diffusion kernel via `AnisotropicArrheniusDiffusion` and anisotropic arrhenious diffusion material via `AnisotropicArrheniusDiffusionCoef` was implemented in BISON.

The material model `AnisotropicArrheniusDiffusionCoef` computes a two-term Arrhenius diffusion coefficient. The diffusion coefficient D is represented as a rank-two tensor:

$$\begin{bmatrix} D_{11} & D_{12} & D_{13} \\ D_{21} & D_{22} & D_{23} \\ D_{31} & D_{32} & D_{33} \end{bmatrix}, \quad (2)$$

where

$$D_{ij} = \begin{cases} D1_{ij} \exp\left(\frac{-Q1_{ij}}{RT}\right) + D2_{ij} \exp\left(\frac{-Q2_{ij}}{RT}\right), & \text{for } i = j \\ 0, & \text{for } i \neq j \end{cases}, \quad (3)$$

D_{ij} are tensor components that correspond to the orthonormal basis vectors in the local coordinate system, which rotates according to layer orientation, as was shown earlier in Figure 1 in the context of anisotropic thermal conductivity. As with anisotropic thermal conductivity, the off-diagonal elements of this tensor are zero in the local coordinate system but can have non-zero values when the tensor is transformed to the global coordinate system for the solve. The model is capable of applying automatic differentiation if needed.

Here, this capability is demonstrated by means of an example analysis involving a TRISO particle whose exterior surface temperature is 1273 K. The silver atoms are generated in the fuel and diffuse into the inner PyC (IPyC) layer and to the outer SiC and outer PyC (OPyC) layers. The PyC layer is considered to have different diffusivity values in the radial and tangential directions. The impact of these diffusivities on silver transport was analyzed. We started with an isotropic case in which both the radial and tangential diffusivities were equal to D_o (a diffusion coefficient of 5.3×10^{-8} m²/s and an activation energy of 154 kJ/mol). The tangential and radial diffusivities were then systematically increased by factors of 10 and 100, and the silver concentrations in both cases were compared. The gap diffusivity values were defined such that the diffusion increased with decreased gap width. This definition of gap diffusivity was chosen only to illustrate the anisotropic diffusion modeling capability by means of this example, and is not based on experimental data. The results are shown in Figure 8 and Figure 9.

Figure 8 shows that, as the diffusivity in the tangential direction increases, so does the diffusion of the silver atoms into the IPyC layer. Note that SiC has significantly lower diffusivity, and thus the concentrations of the silver atoms in the SiC and OPyC layers are smaller than that in the IPyC layer. The atoms mostly diffuse through the gap region, where the buffer layer is almost in contact with the IPyC layer, then diffuse circumferentially into the IPyC layer. This diffusion through the IPyC layer increases with increased tangential diffusivity.

Figure 9 shows the impact of increasing radial diffusivity of the PyC layer on the silver atoms. Increasing the diffusivity by a factor of 10 produces a clear increase in the concentration of atoms

diffusing radially. However, no further increase occurs in the diffusion of the atoms when the diffusivity is increased by a factor of 100. This happens because the gap acts as bottleneck, having lower diffusivity than the radial diffusivity of the IPyC layer. Thus, further increasing the diffusivity of the PyC layer does not affect the radial diffusion of the silver atoms.

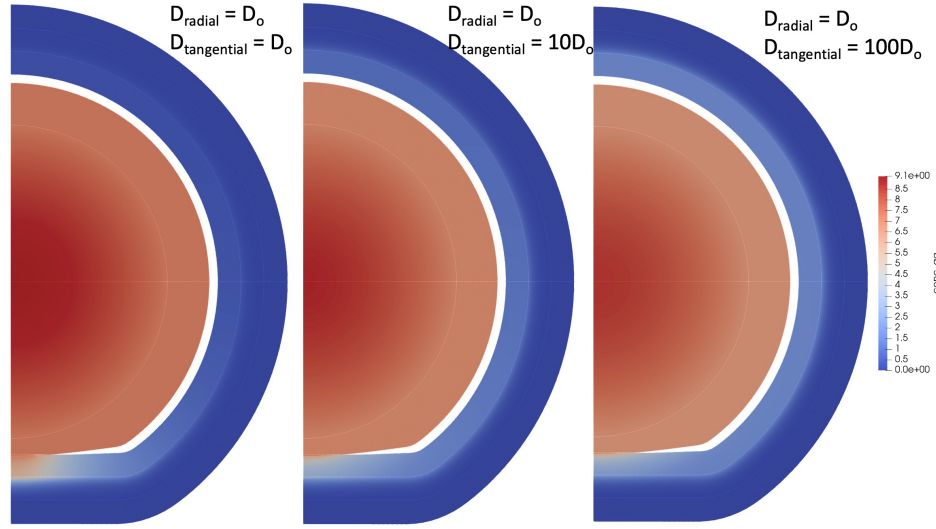


Fig. 8. Comparison of the concentration of silver for its three different diffusivity values for the PyC layers in the tangential direction (units: 10^{14} atoms/m³).

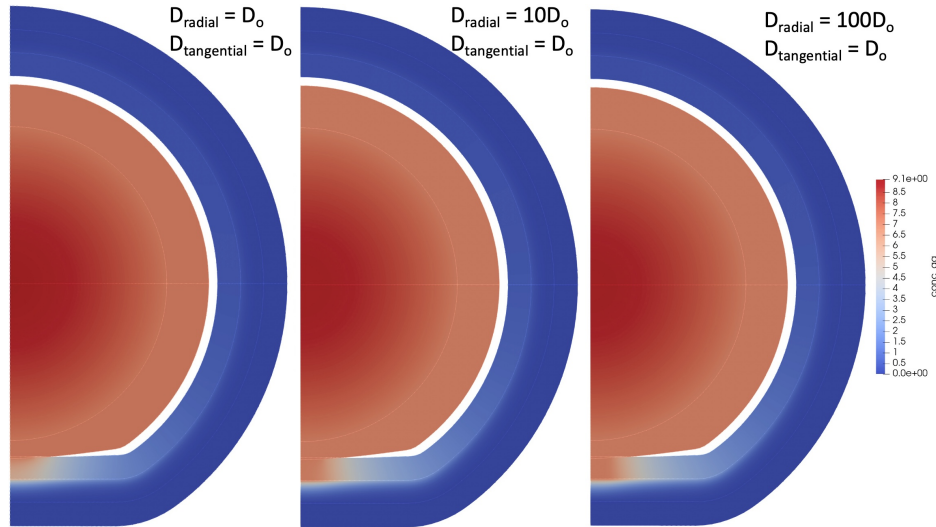


Fig. 9. Comparison of the concentration of silver for its three different diffusivity values for the PyC layers in the radial direction (units: 10^{14} atoms/m³).

C. Summary

The CVD process, used to manufacture TRISO particles, is known to produce crystallographic textured layers that can have anisotropic thermophysical properties. These anisotropic properties may affect the thermomechanical and fission product diffusion behavior of TRISO particles. In the present work, the ability to model anisotropic thermal behavior and diffusion was developed. Specifically, this capability enables users to define thermal conductivity as a second-order tensor whose components correspond to the thermal conductivity magnitudes in the radial and tangential directions. Similarly, the diffusivity coefficient of TRISO can be defined as a second-order tensor whose components correspond to the diffusion coefficient magnitudes in the radial and tangential directions. This newly implemented capability was demonstrated through example analyses conducted on both spherical and aspherical TRISO particles.

III. VERIFICATION OF THE MASS DIFFUSION SOLUTION

Many approaches have been developed to assess the credibility and predictive capabilities of modeling and simulation (M&S) tools (Oberkampf and Roy, 2010; Oberkampf et al., 2007; Hills et al., 2013; Roache, 1998; National Research Council, 2012). An important aspect of these approaches is verification, which ensures that the behavior of the numerical algorithm is consistent with the underlying mathematical model. In this work, we are specifically concerned with verification of BISON, which solves the coupled mechanical, thermal, and species diffusion equations for nuclear fuel systems via the finite-element method (FEM) (Williamson et al., 2021). BISON's governing equations are as follows:

- i. Conservation of momentum (or static equilibrium) is prescribed using Cauchy's equation:

$$\nabla \cdot \boldsymbol{\sigma} = 0, \quad (4)$$

where $\boldsymbol{\sigma}$ is the Cauchy stress tensor (a function of displacement).

- ii. The heat equation is:

$$\rho c_P \frac{\partial T}{\partial t} + \nabla \cdot \mathbf{q} - E_f \dot{F} = 0, \quad (5)$$

where T is the temperature, c_P is the specific heat capacity, \mathbf{q} is the heat flux, E_f is the energy released per fission, and \dot{F} is the volumetric fission rate.

- iii. Fission product species conservation (i.e., mass diffusion or Fick's second law) is given by:

$$\frac{\partial C}{\partial t} + \nabla \cdot \mathbf{J} + \lambda C - p = 0, \quad (6)$$

where C is the concentration, λ is the decay constant ($\lambda = \frac{\ln(2)}{T_{1/2}}$ in terms of the half-life $T_{1/2}$), p is the source rate of a given species, and \mathbf{J} is the mass flux. With neglected radioactive decay, Equation 5 and Equation 6 become similar PDEs.

Recent work has focused on verification of the PDE governing the conservation of fission product species (i.e., Equation 6), particularly its predictions under spatiotemporal reactor conditions for a TRISO particle. The fission product diffusion calculations were previously validated against the AGR-1 (Hales et al., 2021, 2020) and AGR-2 (Hales et al., 2022) experimental data, and benchmarked against the other fuel performance codes found within the Coordinated Research Program (CRP-6) benchmark (Hales et al., 2021, 2020). In addition to these validation cases, the reliability of BISON predictions under both steady-state and transient conditions had previously been verified (Hales et al., 2014; Toptan et al., 2020b,a; Hales et al., 2021; Toptan et al., 2022b; Hales et al., 2022). This paper covers a set of numerical experiments examining BISON's predictive capability concerning the conservation of fission product species (or the mass diffusion solution) under various in-pile and out-of-pile conditions. The verification exercises were chosen for their relevance to spherical TRISO particles for both short- and long-lived (i.e., stable) fission product species. The material presented here is a subset of the information found in Toptan et al. (2023).

A. Background

The conservation of fission product species is given by Equation 6. The PDE is composed of terms for transient effects, diffusion, decay, and the volumetric source rate. We use the same convention throughout this study, with the additional following symbols and dimensionless numbers: a is the radius of the sphere, $\rho = r/a$ is the dimensionless normalized radius ($0 \leq \rho \leq 1$), $\tau = D't$ is the dimensionless diffusion

time (-), $D' = D/a^2$ is the reduced diffusion coefficient (s^{-1}), and $\mu = \lambda/D'$ is the ratio of the decay rate to its diffusion rate (-). For short-lived isotopes, $\mu \gg 1$; for long-lived isotopes, $\mu \ll 1$; and for a stable isotope, $\mu = 0$.

In all cases, the sphere of radius a is subject to similar boundary and initial conditions. Radial symmetry is considered at the origin ($r = 0$) for all $t \geq 0$. The concentration is set to zero at the outer surface ($r = a$), and at $r = a$ for all $t \geq 0$, a Dirichlet boundary condition is applied as $C = \hat{C}$ on Γ_C , where \hat{C} is a prescribed value for concentration ($\hat{C} = 0$ to remain concentration-free, or for the ideal sink in this study) and Γ_C is the boundary on which it is applied. A constant (or flat) profile is applied as the initial concentration profile: $C(\mathbf{x}, t) = \hat{C}_0$ at $t = 0$ for $0 \leq r \leq a$, where \hat{C}_0 is the prescribed initial concentration.

In this study, the following three main verification exercises concerning the reactor conditions for spherical TRISO particles were selected:

- 1) In-pile production, transport, and decay of short-lived isotopes ($\lambda \neq 0$), where the spherical particle is initially concentration-free ($\hat{C}_0 = 0$) and a non-zero source term is applied ($p \neq 0$). See Section III-B.
- 2) In-pile production, transport, and decay of long-lived (or stable) isotopes ($\lambda \equiv 0$), where the spherical particle is initially free of concentration-free ($\hat{C}_0 = 0$) and a non-zero source term is applied ($p \neq 0$; see Section III-C.)
- 3) Out-of-pile conditions for transport and decay of pre-existing isotopes ($\lambda \neq 0$), where the spherical particle is initially at a non-zero concentration ($C_0 \neq 0$), and no production ($p = 0$) occurs within the particle, see Section III-D.

The analytical solutions to this PDE under these conditions were taken from Nabielek et al. (1974). In an attempt to better understand the physics by applying a reduced number of variables, these expressions are nondimensionalized in this study. The BISON-computed results were compared against the expected results obtained from the analytical expressions in terms of the following QoIs:

- 1) The *concentration*, $C(r, t)$, was obtained from Equation 6, based on the problem settings (e.g., initial/boundary conditions and geometry). For constant D and p , Equation 6 in spherical coordinates reduces to:

$$\frac{\partial C}{\partial t} = \frac{1}{r} \frac{\partial^2}{\partial r^2}(rC) - \lambda C + p. \quad (7)$$

- 2) The *release rate*, $R(t)$, is given as the product of the flux to the outside and the surface area of the sphere ($4\pi a^2$):

$$R(t) = -4\pi a^2 D \left. \frac{\partial C}{\partial r} \right|_{r=a}. \quad (8)$$

The ratio of the release rate to the production rate over the whole volume of the sphere ($\frac{4}{3}\pi a^3$) is referred to as the *release-rate over birth-rate* (R/B) (-), and is expressed as:

$$(R/B) = \frac{R(t)}{\frac{4}{3}\pi a^3 p(t)}. \quad (9)$$

The R/B ratio can also be thought of as the fractional release rate. This ratio is the non-dimensional correspondence of the release rate and is only meaningful for in-pile conditions.

- 3) The *fractional release* (i.e., *release fraction*), $F(t)$ (-) is defined as the ratio of the number of undecayed atoms outside the sphere to the number of undecayed atoms in the whole system. For a

constant production rate (i.e., $p(t) = p$), the above relation reduces to:

$$F(t) = \frac{\int_0^t R(t') e^{\lambda t} dt'}{\frac{4}{3}\pi a^3 \{C_0 + \frac{p}{\lambda} [e^{\lambda t} - 1]\}}. \quad (10)$$

B. Exercise 1: In-pile production, transport, and decay of short-lived isotopes ($C_0 = 0$, $p \neq 0$, and $\lambda \neq 0$)

The in-pile conditions for a decaying fission product ($\lambda \neq 0$) are considered in terms of the following settings: an initial concentration of zero in the sphere ($C_0 = 0$ for $0 \leq r \leq a$), and a non-zero source ($p \neq 0$). In this study, we assume constant source generation, $p(t) = p$. Equation 6 is solved in the spherical coordinates. For the in-pile production, transport, and decay of short-lived isotopes, the resulting analytical expressions for the concentration, R/B, and fractional release are as follows:

1) The concentration profile, $C(\rho, \tau)$, is expressed as:

$$\frac{C(\rho, \tau)}{p/\lambda} = \frac{2\mu}{\pi\rho} \sum_{n=1}^{\infty} (-1)^{n+1} \frac{1 - e^{-(n^2\pi^2 + \mu)\tau}}{n(n^2\pi^2 + \mu)} \sin(n\pi\rho), \quad (11a)$$

and as $\tau \rightarrow \infty$, Equation 11a reduces to:

$$\frac{C_{\infty}}{p/\lambda} = 1 - \frac{\sinh(\rho\sqrt{\mu})}{\rho \sinh(\sqrt{\mu})}. \quad (11b)$$

2) The R/B ratio is expressed as:

$$(R/B) = \frac{3}{\sqrt{\mu}} \left(\coth(\sqrt{\mu}) - \frac{1}{\sqrt{\mu}} \right) - 6 \sum_{n=1}^{\infty} \frac{e^{-(n^2\pi^2 + \mu)\tau}}{n^2\pi^2 + \mu}. \quad (12)$$

Equation 12 reduces to the first term on the right-hand side (RHS) of this relation as $\tau \rightarrow \infty$.

3) The fractional release, $F(\tau)$, is expressed as:

$$F(\tau) = \frac{3}{\sqrt{\mu}} \left(\coth(\sqrt{\mu}) - \frac{1}{\sqrt{\mu}} \right) - \frac{6\mu}{e^{\mu\tau} - 1} \sum_{n=1}^{\infty} \frac{1 - e^{-n^2\pi^2\tau}}{n^2\pi^2 (n^2\pi^2 + \mu)}. \quad (13)$$

Figure 10 compares the analytical and the computed concentration, $C/(p/\lambda)$, at four different radial locations ($\rho = 0.25, 0.50, 0.75$, and 0.95); R/B; and $F(\tau)$ as a function of dimensionless diffusion time, τ (with arbitrarily chosen $\mu = 0.1$). In this exercise, the first 100,000 terms in the infinite summation are considered sufficient to prevent any artificial oscillations in the analytical solution. The BISON predictions agree well with the analytical results for the concentration profiles, R/B ratio, and fractional release from a solid sphere under in-pile conditions for a decaying fission product.

C. Exercise 2: In-pile production and transport of a stable fission product ($C_0 = 0$, $p \neq 0$, and $\lambda = 0$)

The in-pile conditions for a stable fission product ($\lambda = 0$) are considered in terms of the following settings: an initial concentration of zero in the sphere ($C_0 = 0$ for $0 \leq r \leq a$), and a non-zero source ($p \neq 0$). In this study, we assume constant source generation, $p(t) = p$. Equation 6 is solved in the spherical coordinates. For the in-pile production and transport of a stable fission product, the resulting analytical expressions for the concentration, R/B, and fractional release are as follows:

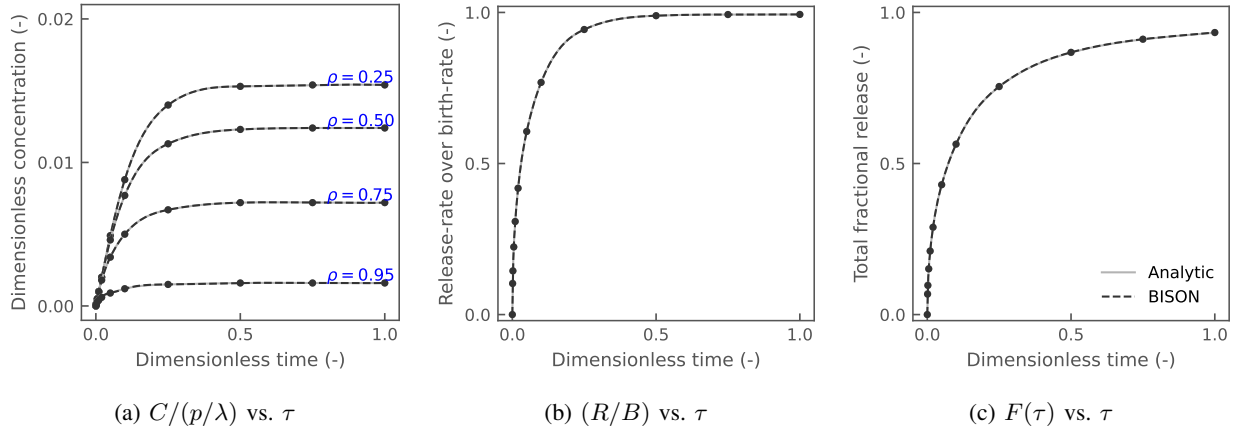


Fig. 10. Comparison of the analytical and the computed (a) concentration, $C/(p/\lambda)$, at four different radial locations ($\rho = 0.25, 0.50, 0.75$, and 0.95); (b) the release rate over the birth rate, (R/B) ; and the (c) fractional release, $F(\tau)$, as a function of dimensionless diffusion time, τ (with arbitrarily chosen $\mu = 0.1$), for in-pile production, transport, and decay of short-lived isotopes ($C_0 = 0$, $p \neq 0$, and $\lambda \neq 0$).

1) The concentration profile, $C(\rho, \tau)$ is expressed as:

$$\frac{C(\rho, \tau)}{p/6D'} = (1 - \rho^2) - \frac{12}{\rho} \sum_{n=1}^{\infty} (-1)^{n+1} \frac{e^{-n^2\pi^2\tau}}{n^3\pi^3} \sin(n\pi\rho). \quad (14)$$

The steady-state ($\tau \rightarrow \infty$) solution for the concentration reduces to the first term on the RHS of Equation 14.

2) The R/B ratio is expressed as:

$$(R/B) = 1 - 6 \sum_{n=1}^{\infty} \frac{e^{-n^2\pi^2\tau}}{n^2\pi^2}. \quad (15)$$

3) The fractional release, $F(t)$, is expressed as:

$$F(\tau) = 1 - \frac{6}{\tau} \sum_{n=1}^{\infty} \frac{1 - e^{-n^2\pi^2\tau}}{n^4\pi^4}. \quad (16)$$

Figure 11 compares the analytical and the computed concentration, $C(\rho, \tau)/[p/(6D')]$, at four different radial locations ($\rho = 0.25, 0.50, 0.75$, and 0.95); R/B; and $F(\tau)$ as a function of τ (with arbitrarily chosen $\mu = 0.1$; however, the concentration solution is independent of μ). In this exercise, the first 100,000 terms in the infinite summation are considered sufficient to prevent any artificial oscillations in the analytical solution. The BISON predictions agree well with the analytical results for the concentration profiles, R/B ratio, and fractional release from a solid sphere under in-pile conditions for a stable fission product.

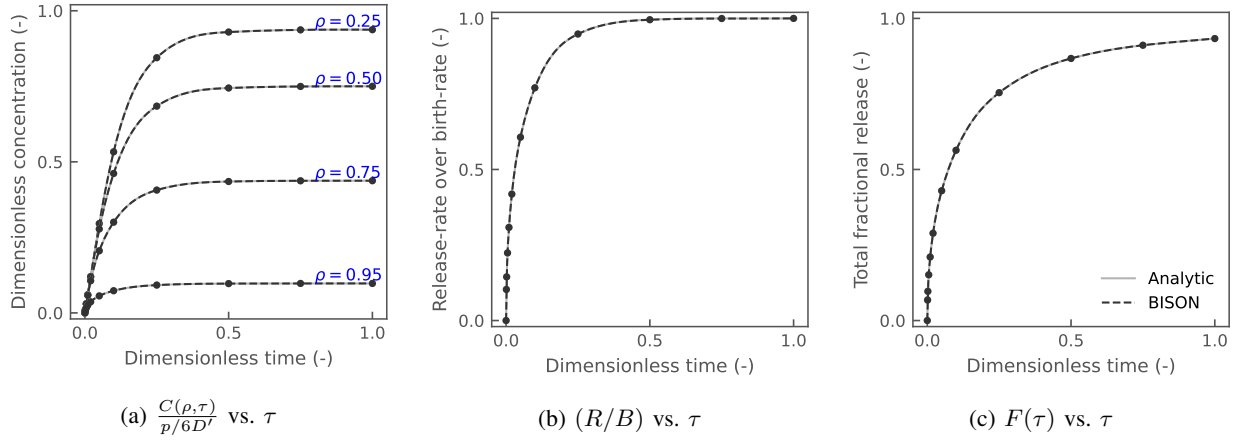


Fig. 11. Comparison of the analytical and the computed (a) concentration, $C(\rho, \tau)/[p/(6D')]$, at four different radial locations ($\rho = 0.25, 0.50, 0.75$, and 0.95); (b) release rate over birth rate, (R/B) ; and (c) fractional release, $F(\tau)$, as a function of dimensionless diffusion time, τ (with arbitrarily chosen $\mu = 0.1$; however, the concentration solution is independent of μ) for in-pile production and transport of a stable fission product ($C_0 = 0$, $p \neq 0$, and $\lambda = 0$).

D. Exercise 3: Out-of-pile conditions for the transport and decay of preexisting isotopes ($C_0 \neq 0$, $p = 0$, and $\lambda \neq 0$)

The out-of-pile conditions for a decaying fission product ($\lambda \neq 0$) are considered in terms of the following settings: an initial concentration of non-zero in the sphere ($C_0 \neq 0$ for $0 \leq r \leq a$), and a zero source ($p = 0$). Equation 6 is solved in the spherical coordinates. For out-of-pile conditions for the transport and decay of preexisting isotopes, the resulting analytical expressions for the concentration, release rate, and fractional release are as follows:

- 1) The concentration profile, $C(\rho, \tau)$, is expressed as:

$$\frac{C(\rho, \tau)}{C_0} = \frac{2}{\rho} \sum_{n=1}^{\infty} (-1)^{n+1} \frac{e^{-(n^2\pi^2 + \mu)\tau}}{n\pi} \sin(n\pi\rho). \quad (17)$$

- 2) The out-of-pile release rate, $R(\tau)$, is expressed as:

$$R(\tau) = 8\pi a^3 \frac{C_0 \lambda}{\mu} \sum_{n=1}^{\infty} e^{-(n^2\pi^2 + \mu)\tau}. \quad (18)$$

- 3) The fractional release, $F(\tau)$, is expressed as:

$$F(\tau) = 1 - 6 \sum_{n=1}^{\infty} \frac{e^{-n^2\pi^2\tau}}{n^2\pi^2}. \quad (19)$$

Figure 12 compares the analytical and the computed concentration, C/C_0 , at four different radial locations ($\rho = 0.25, 0.50, 0.75$, and 0.95); $R(\tau)$; and $F(\tau)$ as a function of τ (with arbitrarily chosen $\mu = 0.1$). Note that, as the R/B definition is not meaningful in regard to out-of-pile conditions, we use

the out-of-pile release rate $R(\tau)$. As $\tau \rightarrow \infty$, the dimensionless concentration approaches zero. In this exercise, the first 100,000 terms in the infinite summation are considered sufficient to prevent any artificial oscillations in the analytical solution. The BISON predictions agree well with the analytical results for concentration profiles, release rate, and fractional release from a solid sphere under out-of-pile conditions for the transport and decay of preexisting isotopes.

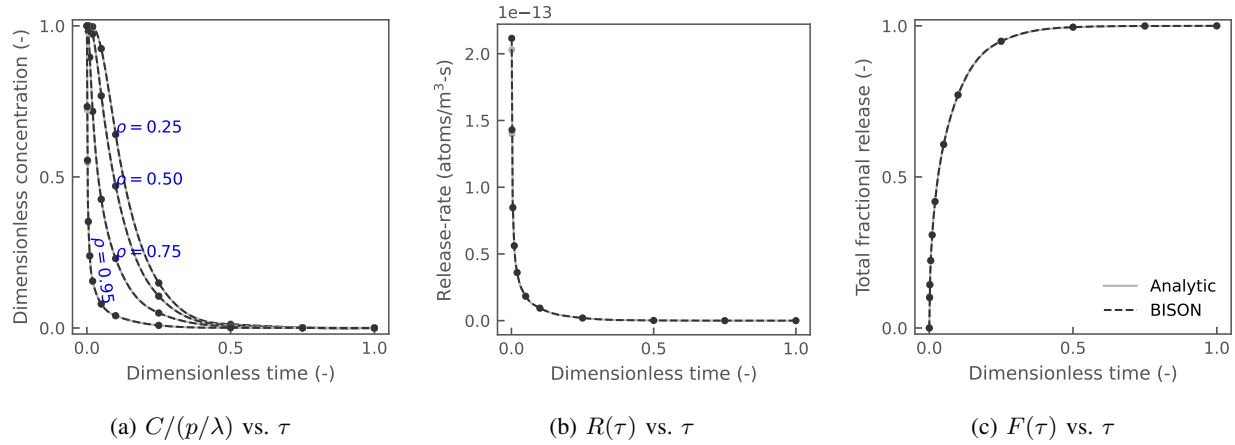


Fig. 12. Comparison of the analytical and the computed (a) concentration, C/C_0 , at four different radial locations ($\rho = 0.25, 0.50, 0.75$, and 0.95); (b) release rate, $R(\tau)$; and (c) fractional release, $F(\tau)$, as a function of dimensionless diffusion time, τ (with arbitrarily chosen $\mu = 0.1$) for out-of-pile conditions for the transport and decay of preexisting isotopes ($C_0 \neq 0$, $p = 0$, and $\lambda \neq 0$).

E. Summary

The BISON predictions agree well with the analytical results for concentration profiles, release rate and R/B, and fractional release from a solid sphere under in-pile conditions for both decaying and stable fission products, and under out-of-pile conditions for the preexisting isotopes. These verification problems were made available in the BISON verification test suite and can be found within the BISON verification documentation.

IV. DIFFUSION COEFFICIENT ESTIMATES BASED ON THE AGR-1 AND -2 INTEGRAL RELEASE EXPERIMENTS

The fission product diffusion (or mass diffusion) follows Equation 6. The mass flux, \mathbf{J} , is:

$$\mathbf{J} = -D\nabla C, \quad (20)$$

where the diffusion coefficient, D (m²/s), is defined in an Arrhenius-type temperature-dependent form:

$$D = D(T, \Gamma, c, \dots) = \sum_{i=1,2} D_i \exp\left(-\frac{Q_i}{RT}\right), \quad (21)$$

where D_i is the frequency factor (m²/s), Q_i is the activation energy (J/mol), R is the universal gas constant (8.3145 J/mol/K), and T is the temperature (K). Typical values of D_i and Q_i are tabulated in Table I for long-lived fission product species such as silver (Ag), cesium (Cs), strontium (Sr), and krypton (Kr).

TABLE I. Mass diffusion coefficients from Hales et al. (2022).

FP	Zone	D_1 (m ² /s)	Q_1 (kJ/mol)	D_2 (m ² /s)	Q_2 (kJ/mol)
Ag	Kernel	6.7×10^{-9}	165		
	PyC	5.3×10^{-9}	154		
	SiC	3.6×10^{-9}	215		
Cs ^a	Kernel	5.6×10^{-8}	209	5.2×10^{-4}	362
	PyC	6.3×10^{-8}	222		
	SiC	$5.5 \times 10^{-14} e^{(\Gamma \times 1.1/5)}$	125	1.6×10^{-2}	514
Sr	Kernel	2.2×10^{-3}	488		
	PyC	2.3×10^{-6}	197		
	SiC	1.2×10^{-9}	205	1.8×10^6	791
Kr	Kernel	1.3×10^{-12} ($T < 1353^\circ\text{C}$)	126 ($T < 700^\circ\text{C}$)	6×10^{-1} ($T \geq 700^\circ\text{C}$)	480 ($T \geq 700^\circ\text{C}$)
		8.8×10^{-15} ($T \geq 700^\circ\text{C}$)	54 ($T \geq 700^\circ\text{C}$)		
	PyC	2.9×10^{-8}	291	2×10^5	923
	SiC	8.6×10^{-10} ($T < 1353^\circ\text{C}$)	326 ($T < 1353^\circ\text{C}$)		
		3.7×10^1 ($T \geq 1353^\circ\text{C}$)	657 ($T \geq 1353^\circ\text{C}$)		

^a Γ is the fast neutron fluence ($\times 10^{25}$ n/m², $E > 0.18$ MeV)

This study aims to investigate the availability and reliability of diffusion coefficients for key radioactive species in the particle as listed in Table I. Section IV-A presents the methods used in the calibration to estimate the diffusion coefficients based on AGR integral release experiments. Section IV-B briefly describes the AGR-1 and -2 experiments during both the base irradiation and safety heating tests. Section IV-C details how the calibration techniques were applied to BISON. Section IV-D provides and discusses the diffusion coefficient estimates and the surveyed empirical coefficients of the key radioactive species in the kernel, PyC, and SiC layers. Lastly, Section IV-E concludes this section with a discussion and outline of future work.

A. Calibration Technique

Calibration is the process of using observations—either synthetic data or experimental data—to estimate the parameters of a computational model of interest. Several parameter estimation methods are available in the literature (e.g., the frequentist and Bayesian estimation methods). This study employs the frequentist method, in which the frequentist view of probability is the frequency of occurrence as $P(A) = n/N$ for n times that event A occurs in N . The Bayesian view of probability is a measure of the plausibility of an event, given incomplete knowledge, with Bayes' rule simply expressing the likelihood of an event A occurring that event B as $P(A|B) = P(B|A)P(A)/P(B)$ for events A and B with $P(B) \neq 0$. Frequentist inference does not require a prior and is less computationally intensive than Bayesian inference. The Bayesian inference can be computationally intensive due to the integration over many dimensions (Toptan, 2019).

The main principle in the frequentist approach is to estimate model parameters $\theta = \{\theta_i\}_{i=1}^n$ by minimizing the differences between the observations $\mathbf{v} = \{v_i\}_{i=1}^n$ and the predictions $\mathbf{y} = \{y_i\}_{i=1}^n$, with predictions being made according to the model function $f(\theta)$:

$$\hat{\theta} = \underset{\theta}{\operatorname{argmin}} \sum_{i=1}^n [v_i - y_i]^2, \quad (22)$$

where the variance estimate is expressed by:

$$\hat{\sigma}^2 = \frac{1}{(n-p)} \mathbf{R}^T \mathbf{R}, \quad (23)$$

where \mathbf{R} is the residual matrix between the observations and the predictions. The ordinary least square method is a common (or traditional) example of the frequentist method. The sensitivity matrix χ of the model function is calculated numerically and used to estimate the covariance of parameter matrix θ . The covariance matrix \mathbf{V} can be estimated via

$$\hat{\mathbf{V}}(\hat{\theta}) = \hat{\sigma}^2 (\hat{\chi}^T \hat{\chi})^{-1}, \quad (24)$$

with the sensitivity matrix χ approximated numerically at each state point from the experimental data, as per:

$$\hat{\chi}_{ij} = \frac{\partial f(x_i, \hat{\theta})}{\partial \theta_j} \approx \frac{f(x_i, \hat{\theta} + \epsilon_j) - f(x_i, \hat{\theta})}{\epsilon}, \quad (25)$$

with a small perturbation to the j -th parameter value, ϵ_j .

1) Bootstrapping Method

For highly nonlinear problems or problems involving small sample sizes, the bootstrapping method (see Algorithm 1) is an alternative way to construct sampling distributions by using frequentist estimators. The same estimators are resampled to calculate a MC approximation of the parameter distributions. Since actual sampling of additional data is not practical, the existing data are resampled (Porter, 2018).

2) Nelder-Mead Method

This study employs the Nelder-Mead method as the minimization technique for Equation 22, which uses the simplex algorithm (Nelder and Mead, 1965; Wright, 1996) and is considered robust in many applications. The Nelder-Mead method iteratively generates a sequence of simplices to approximate an optimal point of $\min f(x)$, where $f : \mathbb{R}^n \rightarrow \mathbb{R}$ is the objective function and n is the dimension. A

Algorithm 1 Bootstrapping parameter estimation, which is the process of resampling estimators from the same set of data to acquire a distribution of those estimators (Porter, 2018).

- 1: **Input:** Experimental data \mathbf{y} , model f , and number of bootstrap samples M .
 - 2: **Output:** Frequentist estimates of optimized parameters $\boldsymbol{\theta}_{\text{OLS}}$, experimental error $\hat{\sigma}^2$, and covariance matrix \hat{V} .
 - 3: Determine $\boldsymbol{\theta}_{\text{OLS}} = \underset{\boldsymbol{\theta}}{\operatorname{argmin}} \sum_{i=1}^N [y_i - f(x_i, \boldsymbol{\theta})]^2$
 - 4: Construct standardized residuals $r_i = \sqrt{\frac{N}{N-p}} [y_i - f(x_i, \boldsymbol{\theta})]$
 - 5: **for** $m = 1$ **to** M **do**
 - 6: Sample from r with replacement to generate a bootstrap sample of N standardized residuals, \bar{r}^m
 - 7: Generate synthetic data $y^m = f(x, \boldsymbol{\theta}_{\text{OLS}}) + \bar{r}^m$
 - 8: Calculate the OLS estimate to obtain $\boldsymbol{\theta}^m$
 - 9: **end for**
 - 10: Now $\boldsymbol{\theta}^m$ is a chain that can be used to construct $\boldsymbol{\theta}_{\text{OLS}}$, $\hat{\sigma}^2$, and \hat{V} .
-

simplex is a geometric figure in n dimensions that is the convex hull of $n + 1$ vertices. We denote a simplex with vertices $\mathbf{x}_1, \mathbf{x}_2, \dots, \mathbf{x}_{n+1}$ as Δ . At each iteration, the vertices $\{\mathbf{x}_j\}_{j=1}^{n+1}$ of the simplex are ordered according to the objective function values:

$$f(\mathbf{x}_1) \leq f(\mathbf{x}_2) \leq \dots \leq f(\mathbf{x}_{n+1}). \quad (26)$$

Here, \mathbf{x}_1 is referred to as the best vertex and \mathbf{x}_{n+1} as the worst. If several vertices have the same objective values, consistent tie-breaking rules are required for the method to be well defined. The algorithm uses four possible operations: reflection, expansion, contraction, and shrink, each being associated with a scalar parameter: α , β , γ , and δ , respectively, whose values must satisfy $\alpha > 0$, $\beta > 1$, $0 < \gamma < 1$, and $0 < \delta < 1$. In the standard implementation of the Nelder-Mead method, the parameters are chosen to be

$$\{\alpha, \beta, \gamma, \delta\} = \left\{1, 2, \frac{1}{2}, \frac{1}{2}\right\}. \quad (27)$$

Here, the parameters were chosen adaptively, based on the problem dimension n (for $n \geq 2$) as

$$\{\alpha, \beta, \gamma, \delta\} = \left\{1, 1 + \frac{2}{n}, 0.75 - \frac{1}{2n}, 1 - \frac{1}{n}\right\}. \quad (28)$$

according to Gao and Han (2012). In this study, we exercised the latter approach. The Nelder-Mead method is one of the bound-constrained minimization techniques that allows to define physical parameter ranges. In our application, we physically constrained the parameter ranges within $(0, \infty)$ to not have positively defined physical values for the mass diffusion coefficients, and our objective function is the code simulation at a given set of mass diffusion parameters.

B. AGR-1 and -2 Experiments

The four irradiation experiments sponsored by the U.S. Department of Energy (DOE)'s AGR program are as follows (EPRI, 2019): (1) early fuel experiment (AGR-1), (2) performance test fuel experiment

(AGR-2), (3) fission product transport experiments (AGR-3/4), and (4) fuel qualification and fuel performance margin testing experiments (AGR-5/6/7). In this study, we evaluate the diffusion coefficients of Ag, Cs, Kr, and Sr, based on the AGR-1 and -2 experiments. Refer to EPRI (2019); Collin (2015, 2018) for more details on the four campaigns of the AGR program.

The *AGR-1 irradiation* provided data on irradiated fuel performance for both baseline and variant fuels. The early data on the performance of fuel variants supported the selection of a reference fuel for the AGR-2 irradiation experiment, as well as the development of an improved fundamental understanding of the relationship among the fuel fabrication process, as-fabricated fuel properties, and performance under both normal operation and potential accident scenarios. The AGR-1 features six uranium oxycarbide (UCO) capsules with a total of 72 compacts containing TRISO particles fabricated in a small laboratory-scale coater. Selected irradiated AGR-1 compacts were evaluated at temperatures of 1600–1800°C during the *AGR-1 safety test*, which aimed to explore the characteristics of fission product release during a depressurized conduction cool-down event experienced by UCO fuel.

The *AGR-2 irradiation* provided irradiated fuel performance data for coated particles at the engineering scale, as well as irradiated fuel specimens for PIE and safety heating testing. As with the AGR-1, the AGR-2 has six capsules, four of which contained U.S.-manufactured fuel, three UCO capsules, and one uranium dioxide (UO₂) capsule. The remaining two capsules (i.e., Capsules 1 and 4) contained fuel manufactured by Westinghouse/Pebble-Bed Modular Reactor SOC Ltd. and Commissariat à l'Énergie Atomique et Aux Énergies Alternatives, and are not discussed or included in our analyses for this study (EPRI, 2019). Similarly, for select compacts, a post-irradiation heating test (i.e., the *AGR-2 safety test*) was conducted at 1600–1800°C to test both the integrity and fission product retention of the TRISO particles.

Figure 13 shows the experimental conditions of both the AGR-1 and -2 fuel compacts at the end of irradiation as a function of burnup, fast neutron fluence, and time-average volume-average (TAVA) temperature. AGR-1 has six UCO capsules, for a total of 72 compacts. AGR-2 has three UCO capsules (i.e., Capsules 2, 5, and 6) and an UO₂ capsule (i.e., Capsule 3), for a total of 48 compacts. The compacts for which PIE data are available are outlined in black. Thus, 17 compacts for AGR-1 and 48 compacts for AGR-2 are considered in this study. The AGR-1 fuel compacts were irradiated up to a burnup of 19.6% fissions per initial metal atom (FIMA), with a fast neutron fluence of $4.3 \times 10^{25} \text{ n/m}^2$ ($E > 0.18 \text{ MeV}$) (Collin, 2015). The AGR-2 fuel compacts were irradiated up to a burnup of 7–10% FIMA, with a fast neutron fluence of up to $5.0 \times 10^{25} \text{ n/m}^2$ ($E > 0.18 \text{ MeV}$) (Collin, 2018).

In Hales et al. (2021, 2022), the BISON predictions were validated against the AGR-1 and -2 experiments and PARFUME predictions. Here, we selected the same compacts used in our previous studies (Hales et al., 2021, 2022), and each compact in this study is referred to based on its capsule, compact number, and stack location. For example, AGR-1 6-4-3 refers to the fourth compact in the sixth capsule, which is stacked in the third axial location for the AGR-1 experiment. A brief summary of the measurements conducted during both the base irradiation and safety tests is provided in the following sections.

The scope of this study mainly focuses on the release fraction data from the AGR-1 and -2 experimental datasets for the key fission products of interest. We use measurements with intact particles in the optimization study, whereas measurements with the failed particles are concerned for cross-validation purposes.

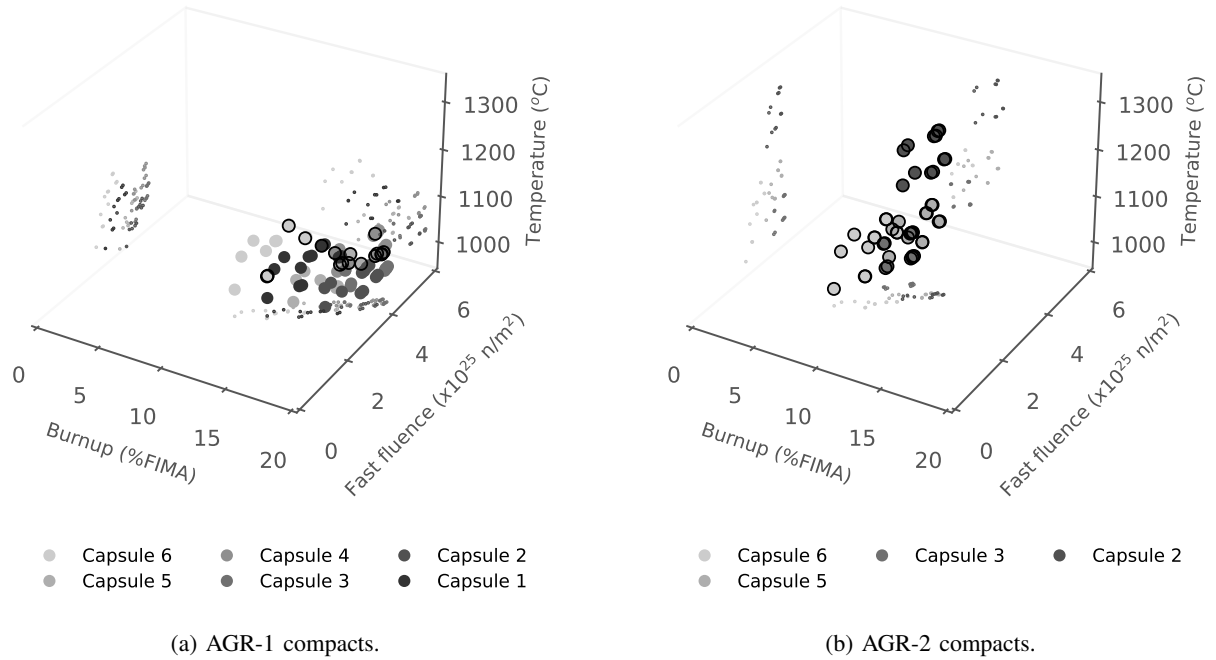


Fig. 13. AGR-1 and -2 compacts at the end of irradiation as a function of burnup, fast neutron fluence, and TAVA. AGR-1 has six UCO capsules, for a total of 72 compacts. AGR-2 has three UCO capsules (2, 5, and 6) and an UO_2 capsule (3), for a total of 48 compacts. The compacts for which PIE data are available are outlined in black; therefore, 17 compacts for AGR-1 and 48 compacts for AGR-2 are considered in the validation. The AGR-1 compacts were irradiated to higher burnups, lower irradiation temperature ranges, and relatively higher fast neutron fluences than the AGR-2 compacts.

1) Base irradiation

The base irradiation results for the AGR-1 compacts are plotted for both intact particles (Figure 14) and failed particles (Figure 15). The material presented here is a subset of the information found in Hales et al. (2021).

Similarly, the base irradiation results for the AGR-2 compacts are plotted for both the intact particles (Figure 16) and the failed particles (Figure 17). The material presented here is a subset of the information found in Hales et al. (2022).

During the base irradiation, the compacts were operated over a moderate temperature range, with a TAVA temperature of 1000–1150°C. Discrepancies between the BISON and PARFUME predictions with respect to the PIE data do not exhibit a clear trend, but indicate that current diffusivity models carry deficiencies that possibly arise from missing physics or incorrect model parameters.

2) Safety heating tests

In addition to the base irradiation, select compacts from the AGR-1 and -2 experiments were evaluated at high temperature (i.e., 1600–1800°C) during the post-irradiation safety tests. BISON modeling of the AGR-2 safety test was done first, as was presented in Hales et al. (2022). This study presents the BISON

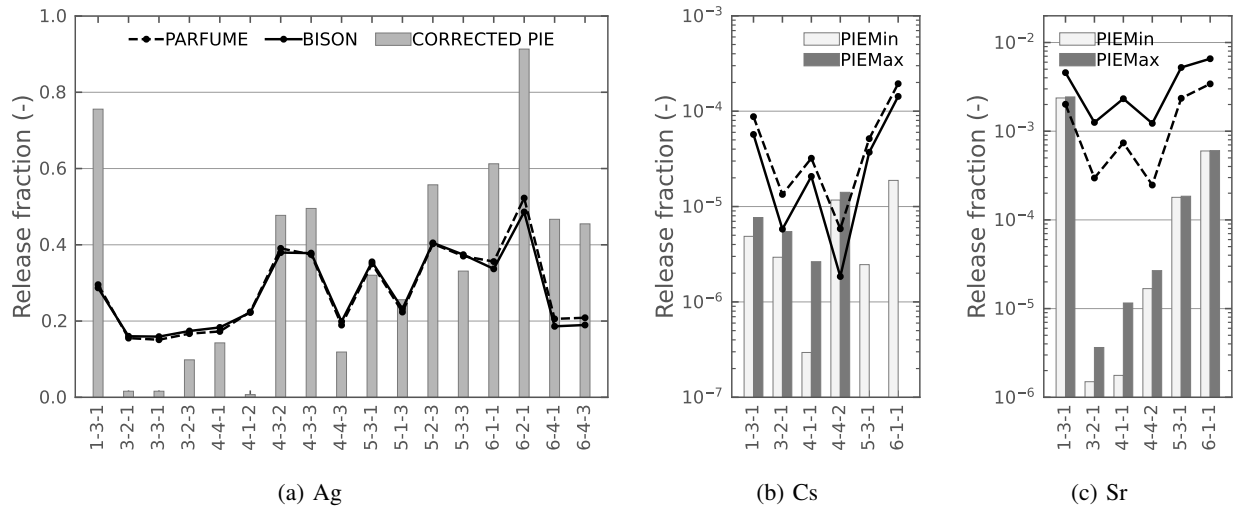


Fig. 14. BISON-predicted release fractions using the International Atomic Energy Agency (IAEA)-reported diffusion coefficients (see Table I) for (a) Ag, (b) Cs, and (c) Sr, as compared to the measured release fractions for the AGR-1 base irradiation with the intact particles.

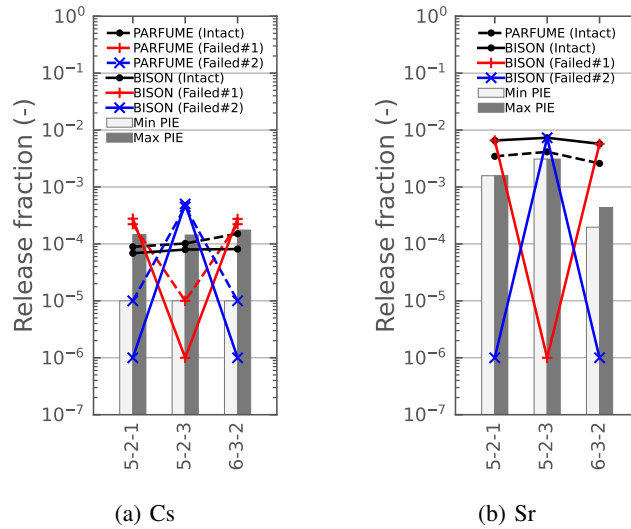


Fig. 15. BISON-predicted release fractions using the IAEA-reported diffusion coefficients (see Table I) for (a) Cs and (b) Sr, as compared to the measured release fractions for the AGR-1 base irradiation with the failed particles. Here, the dashed lines represent the PARFUME predictions, and the solid lines represent the BISON predictions.

modeling of the AGR-1 safety test, which is newly performed and merged into the BISON repository during this fiscal year.

A total of 14 irradiated AGR-1 compacts underwent the safety test; detailed information on them is given in Table II. In the safety test, the compacts were heated for at least 300 hours to the target

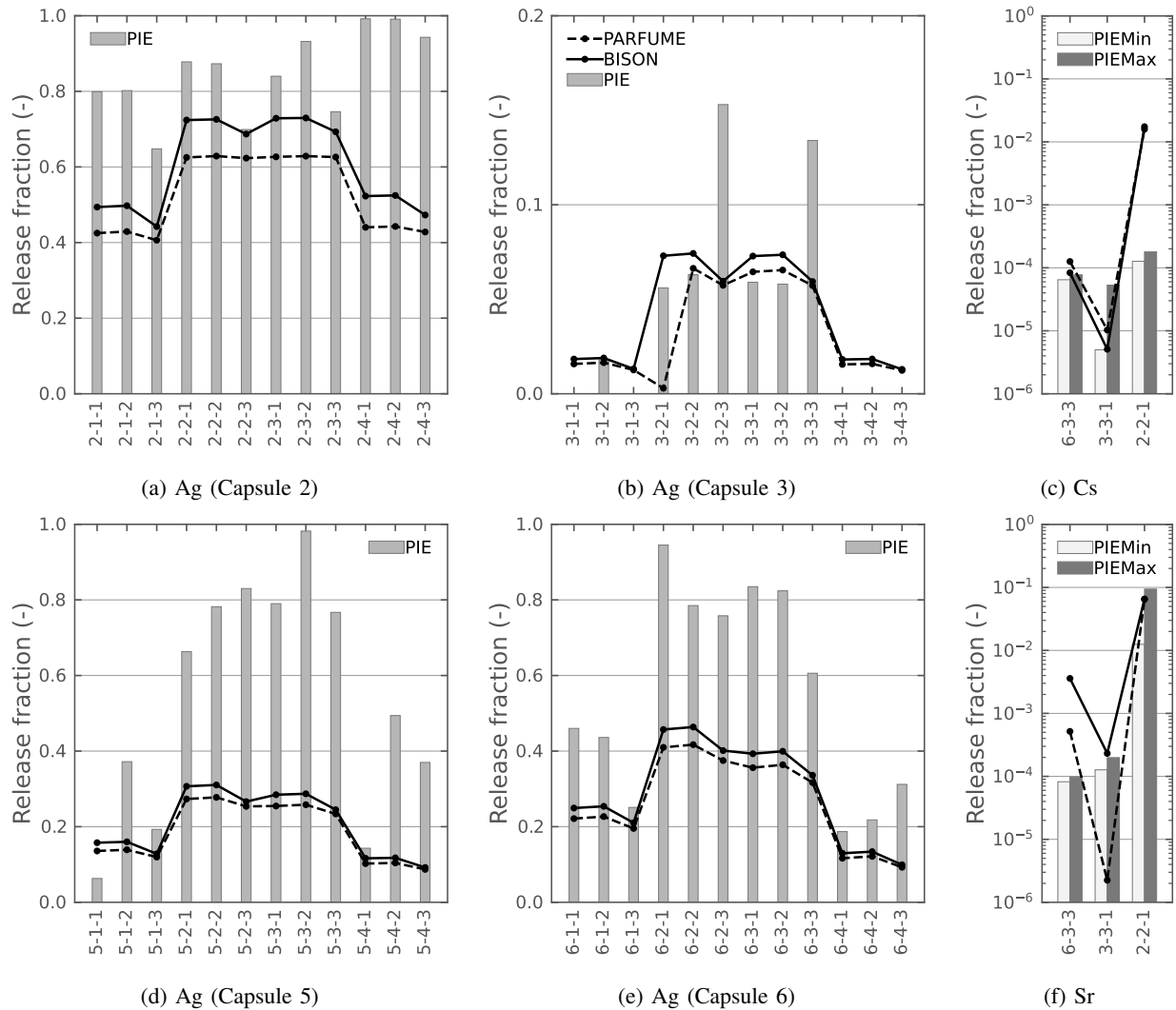


Fig. 16. BISON-predicted release fractions using the IAEA-reported diffusion coefficients (see Table I) for (a,b,d,e) Ag, (c) Cs, and (f) Sr, as compared to the measured release fractions for the AGR-2 base irradiation with the intact particles. Here, Capsules 2, 5, and 6 (a,d,e) are comprised of UCO fuel kernels, while Capsule 3 (b) is comprised of UO_2 fuel kernels.

temperature, as shown in Figure 18. Selection of the target temperatures was based on the fact that 1600°C is the expected maximum fuel temperature during a depressurization conduction cool-down event, and 1800°C is the temperature at which the SiC layer starts to degrade (Collin et al., 2016). Time-dependent release of the fission products Ag, Cs, Sr, europium (Eu), and Kr was monitored by the Core Conduction Cooldown Test Facility (Baldwin et al., 2014) at INL and the Fuel Accident Condition Simulator furnace system (Demkowicz et al., 2012) at Oak Ridge National Laboratory. More detailed PIE analyses of each fission gas species can be found in Morris et al. (2016).

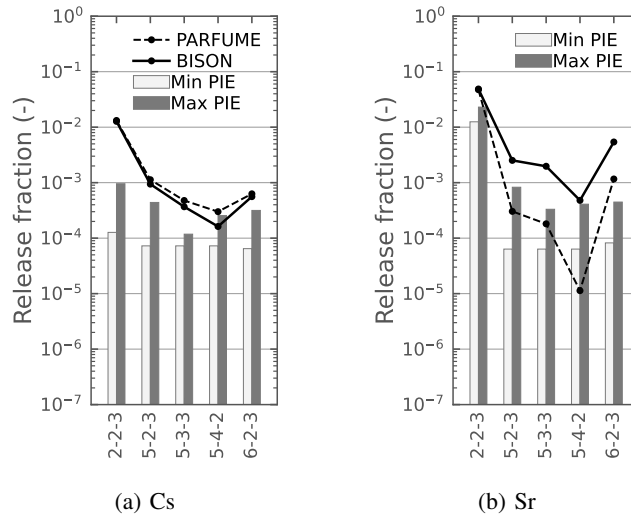


Fig. 17. BISON-predicted release fractions using the IAEA-reported diffusion coefficients (see Table I) for (a) Cs and (b) Sr, as compared to the measured release fractions for the AGR-2 base irradiation with the failed particles.

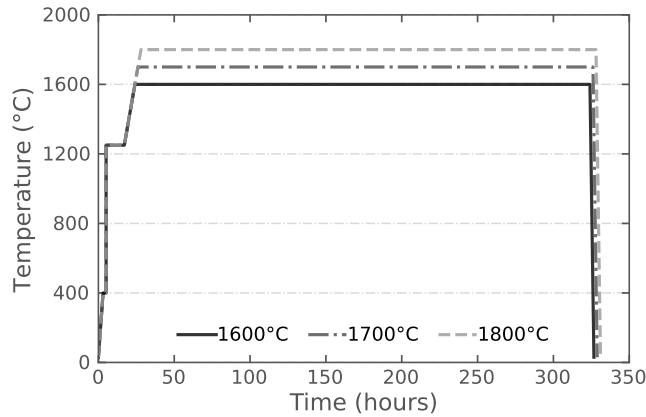


Fig. 18. Heating plan for the AGR-1 safety test (Collin et al., 2016).

For the purpose of code verification, PARFUME predictions for the AGR-1 safety test were introduced as a benchmark (Collin et al., 2016). BISON and PARFUME release fraction predictions were compared to the PIE data from the AGR-1 safety tests conducted on both the intact particles (Figure 19) and the failed particles (Figure 20). For the intact particles, the BISON and PARFUME predictions agree well with each other in regard to Ag and Sr fractional release, while BISON underestimates the release of Cs (as compared to PARFUME) by 1–2 orders of magnitude. Both BISON and PARFUME overestimate the fission product release when compared to the PIE measurement, indicating the adoption of overestimated diffusivity for Ag, Cs, and Sr. For the particles that experienced SiC failure, the fractional releases were

TABLE II. AGR-1 safety tests (Morris et al., 2016).

Test temperature	1600°C							
Compact	6-2-1	6-4-1	6-4-3	3-2-2	3-3-2	4-1-2	4-3-3	5-3-3
Number of particles with failed IPyC	0	1	0	0	1	1	0	0
Burnup (%FIMA)	14.2	13.4	13.4	17.0	17.0	17.4	18.6	17.0
TAVA (°C)	1135	1041	1041	1019	1020	1042	1094	1042

Test temperature	1700°C			1800°C			
Compact	3-3-1	4-4-3	5-1-1	3-2-3	4-3-2	4-4-1	5-1-3
Number of particles with failed IPyC	4	0	3	11	5	2	7
Burnup (%FIMA)	19.1	19.0	18.2	19.1	16.4	19.0	18.2
TAVA (°C)	1051	1059	1041	1053	1057	1057	1042

compared for Ag, Cs, Kr, and Sr, using both BISON and PARFUME. The BISON and PARFUME predictions for all fission products generally match. Again, the fractional releases predicted by BISON and PARFUME are orders of magnitude higher than what is seen in the PIE data, except in the case of Cs, for which the predictions made by BISON and PARFUME closely align with the PIE measurement.

In summary, BISON modeling of the AGR-1 safety test indicates diffusivity overestimation for fission products under high temperatures:

- 1) The diffusivity of Ag in SiC may have been overestimated by a factor of 10^2 – 10^3 at 1600°C and 1700°C, and 10 – 10^2 at 1800°C.
- 2) The diffusivity of Cs in UCO may have been overestimated by a factor of 10^2 – 10^3 at 1600°C, 10^5 at 1700°C, and 10^3 at 1800°C.
- 3) The diffusivity of Sr in SiC may have been overestimated by a factor of 10 – 10^2 at 1600°C and 1700°C, and 10^2 – 10^3 at 1800°C.

Similar conclusions have been drawn based on the PARFUME modeling work (Collin et al., 2016).

Similarly, the BISON and PARFUME release fraction predictions were compared to the measured PIE data collected from the AGR-2 safety tests with intact particles (Figure 21) and failed particles (Figure 22). Additional details on the BISON modeling of the AGR-2 safety test were published in Hales et al. (2022). Again, it is shown that the diffusivities for Ag, Cs, and Sr are overestimated in the high-temperature range.

C. Calibration Settings

The optimization strategy for diffusion coefficient estimates at the engineering scale is designed to be repeatable—as well as expandable to include more data points, if needed. The code inputs are split into multiple inputs for each fission product (FP), accelerating the optimization process by turning off computations for FPs other than the selected one. Another important aspect is the data organization in BISON, which utilizes a consistent data structure, allows the fuel kernel type specification (either UCO or UO_2) to be chosen in the calibration process, and stores data in CSV files for both calibration and visualization purposes.

A brief summary of the data points from the AGR-1 and -2 experiments is tabulated in Table III. The intact particles were considered in the calibration, while failed particles were only used for cross-validation purposes. In the calibration, the diffusion parameters were obtained from a combination of various datasets

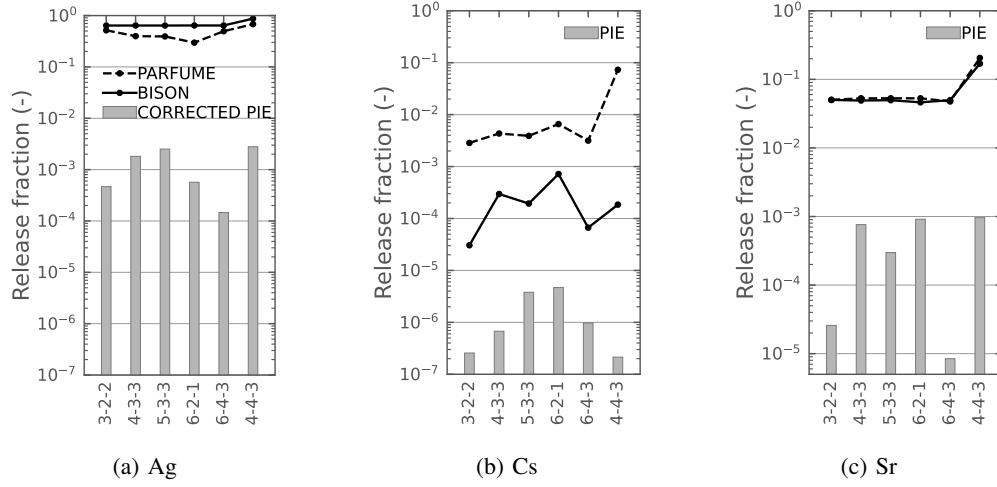


Fig. 19. BISON-predicted release fractions using the IAEA-reported diffusion coefficients (see Table I) for (a) Ag, (b) Cs, and (c) Sr, as compared to the measured release fractions during the AGR-1 safety heating tests with the intact particles.

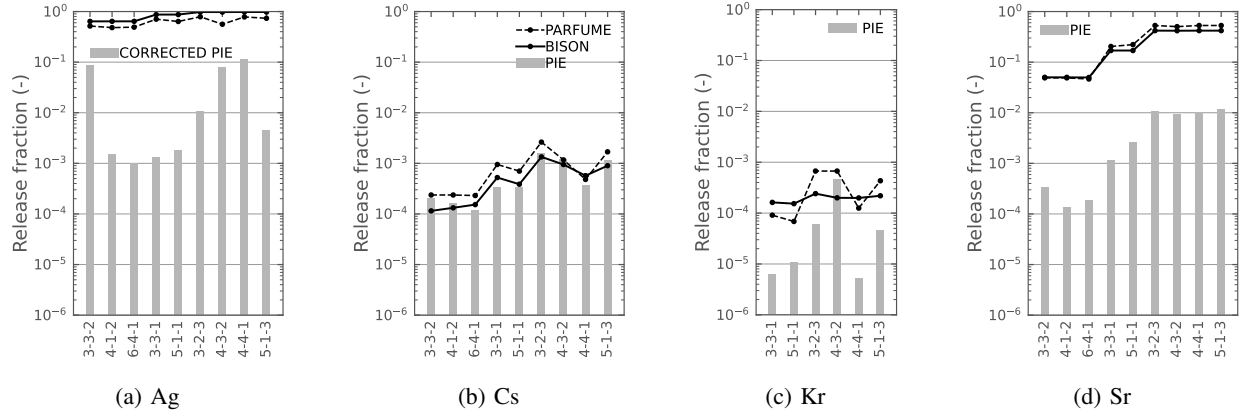


Fig. 20. BISON-predicted release fractions using the IAEA-reported diffusion coefficients (see Table I) for (a) Ag, (b) Cs, (c) Kr, and (d) Sr, as compared to the measured release fractions during the AGR-1 safety heating tests with the failed particles.

(e.g., the AGR-1 dataset only, the AGR-2 dataset only, and the AGR-1 and -2 datasets combined). The initial diffusion parameters were set to IAEA-reported values. A minimum of six diffusion parameters were explored in calibrating each FP (e.g., the D_1 and Q_1 values were considered for the fuel kernel, PyC, and SiC layers in the particle). One could consider increasing the number of parameters to calibrate; however, an important limitation is the number of experimental data points available. The number of required observations must exceed the number of parameters to calibrate (i.e., $n > p$ in Equation 23). Thus, in our exercises, we opted not to calibrate D_2 and Q_2 for the FP of interest.

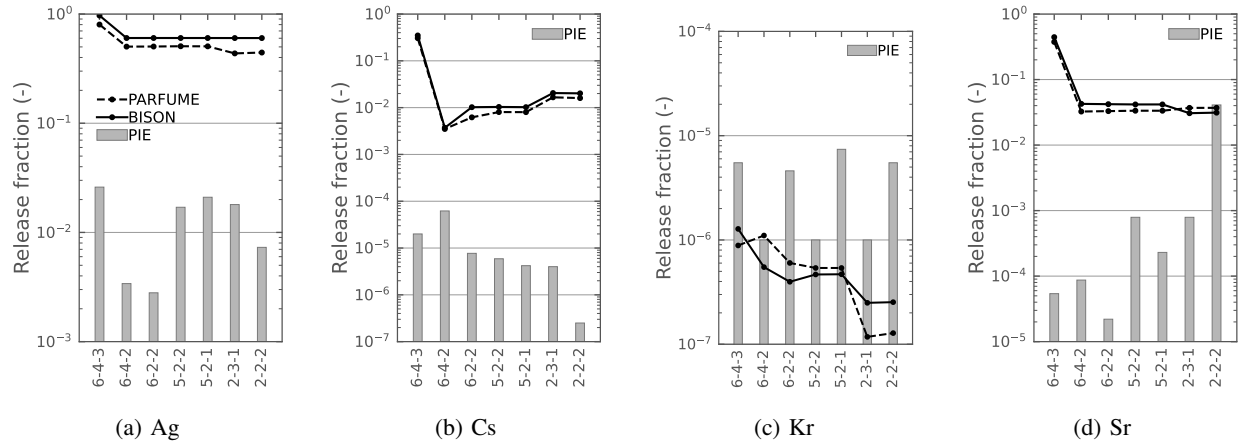


Fig. 21. BISON-predicted release fractions using the IAEA-reported diffusion coefficients (see Table I) for (a) Ag, (b) Cs, (c) Kr, and (d) Sr, as compared to the measured release fractions during the AGR-2 safety heating tests conducted on the intact particles.

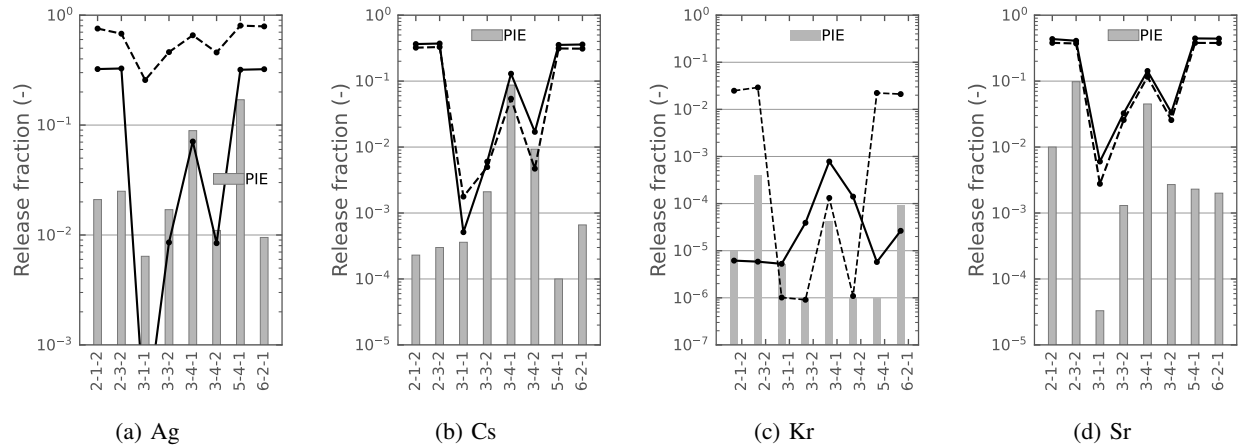


Fig. 22. BISON-predicted release fractions using the IAEA-reported diffusion coefficients (see Table I) for (a) Ag, (b) Cs, (c) Kr, and (d) Sr, as compared to the measured release fractions during the AGR-2 safety heating tests conducted on the failed particles.

TABLE III. Summary of the data points from the AGR-1 and -2 experiments.

			UCO fuel kernel				UO ₂ fuel kernel			
			No.	Intact	Failed	Figure	No.	Intact	Failed	Figure
Ag	AGR-1	Base irradiation	17	✓		14a				
		Safety tests	6	✓		19a				
			9		✓	20a				
	AGR-2	Base irradiation	36	✓		16a,c,d	12	✓		16b
		Safety tests	6	✓		21a				
			4		✓	22a	4		✓	22a
Cs	AGR-1	Base irradiation	6	✓		14b				
			3		✓	15a				
		Safety tests	6	✓		19b				
			9		✓	20b				
	AGR-2	Base irradiation	2	✓		16c				
			5		✓	17a				
		Safety tests	7	✓		21b				
			4		✓	22b	4		✓	22b
Kr	AGR-1	Safety tests	6		✓	20c				
	AGR-2	Safety tests	7	✓		21c	4	✓		21c
							4		✓	22c
Sr	AGR-1	Base irradiation	6	✓		14c				
			3		✓	15b				
		Safety tests	6	✓		19c				
			9		✓	20d				
	AGR-2	Base irradiation	2	✓		16f	1	✓		16f
			5		✓	17b				
		Safety tests	7	✓		21d				
			4		✓	22d	4		✓	22d

D. Results & Discussion

The diffusion coefficient estimates are provided for Ag in Section IV-D1, for Cs in Section IV-D2, for Sr in Section IV-D3, and for Kr in Section IV-D4, along with the literature-reported diffusion coefficients from Collin (2016).

1) Ag results

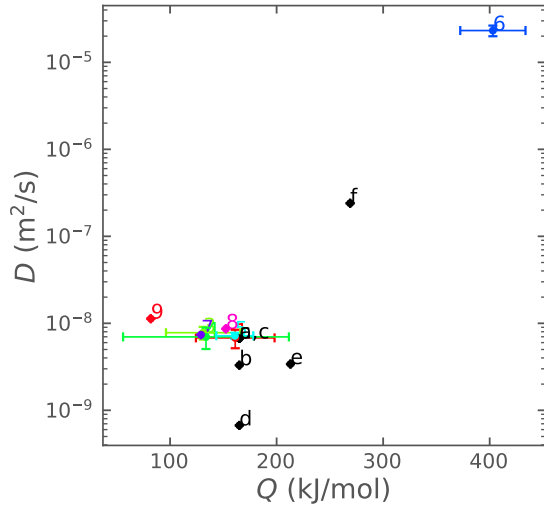
The calibration results generated from this study include diffusion coefficient estimates for Ag in the kernel (Figure 23), PyC (Figure 24), and SiC (Figure 25) layers, based on AGR-1, AGR-2, and combined AGR-1 & -2 PIE data. The literature-reported Ag diffusion coefficients from Collin (2016) are also provided in these plots, and are denoted by alphabetical letters.

Figures 26 and 27 show, respectively, the AGR-1 and -2 base irradiation test results based on intact (or no failed) particles and using the diffusion coefficient estimates from Figures 23–25. Here, we also included the lower-length scale (LLS)-informed diffusion coefficients by Simon et al. (2022) and the best-estimate diffusion coefficients by Seo et al. (2022) for Ag. Note that the microstructure-dependent diffusion coefficients of Ag in SiC were derived by Simon et al. (2022) for the AGR-1 base irradiation. Here, the results on the plots are shown for Simon et al. (2022), using the microstructure-dependent diffusion coefficients in SiC while fixing the Ag diffusion coefficients in both the kernel and PyC as tabulated in Table I. Similarly, Seo et al. (2022) only reports the best estimate diffusion coefficients for Ag in the SiC and PyC layers. The results shown in Seo et al. (2022) were obtained by using these best estimate values while fixing the Ag diffusion coefficients in the kernel as tabulated in Table I.

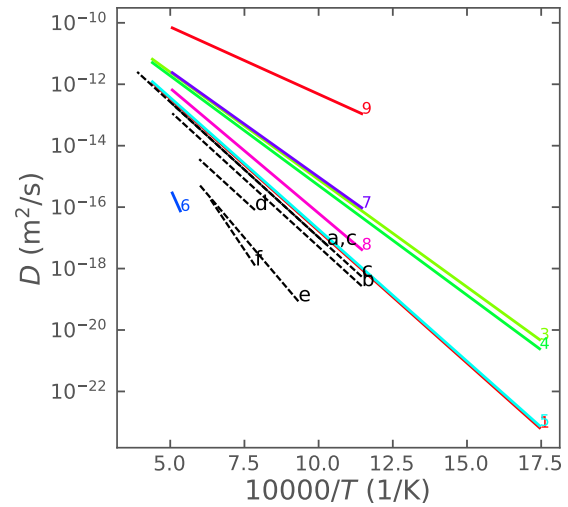
Additionally, the residuals between the measured and the computed release fractions are displayed using box plots, a standardized way of displaying a data distribution by utilizing a five-number summary format (from left to right): minimum, first-quartile, median (orange line), third-quartile, and maximum. The outliers are represented by markers. The box plots are good measures for understanding the central tendency of the distributions/datasets, here the residuals. For a successful calibration study, the residuals between the measured and predicted data should be symmetrical around the zero and tightly grouped. Here, the residuals are computed as $(1 - q_{\text{predicted}}/q_{\text{measured}})$ in fraction, with q being the quantity of interest (QoI).

Figures 26 and 27 show Ag release fractions from both the AGR-1 and -2 base irradiation tests, respectively, for the *intact* particles.

- For the AGR-1 base irradiation tests shown in Figure 26, the code predictions using the Ag diffusion coefficients from all cases (except case 8) show relatively similar agreement with the measured data. Case 8 yields larger release fractions, mainly the diffusion coefficients in case 8 were estimated based on combined AGR-1&-2 UCO compacts. Note that the measured AGR-2 release fractions are relatively larger than those of AGR-1, thus the diffusion coefficient estimates were dominated by the AGR-2 data in the calibration process. This is why using the diffusion coefficients in case 8 for the AGR-1 base irradiation yields overestimation of the release fractions. Similarly, one would expect to observe underestimation of the release fractions when the diffusion coefficients given in case 1 are used for the AGR-2 base irradiation.
- For the AGR-2 base irradiation tests shown in Figure 27, the code predictions with the diffusion coefficients listed in Table I underpredict the measured data in all three assessment cases, namely: (1) when only 36 UCO compacts are used (2) when only 12 UO₂ compacts are used (3) when all 48 UCO and UO₂ compacts are used.



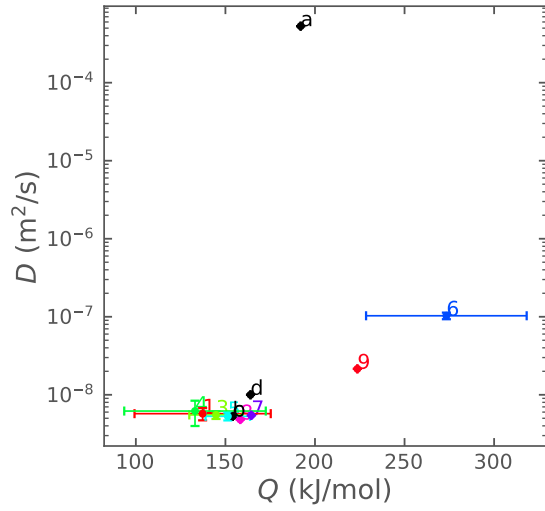
(a) D (m²/s) vs. Q (kJ/mol)



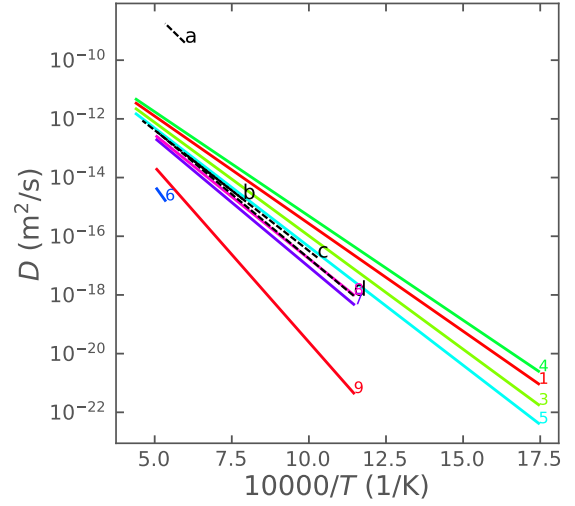
(b) D (m²/s) vs. $10000/T$ (1/K)

Fig. 23. Ag diffusion coefficients in the kernel.

	Reference	Notes	D_1 (m ² /s)	Q_1 (kJ/mol)	D_2 (m ² /s)	Q_2 (kJ/mol)
<i>Literature-reported diffusion coefficients (Collin, 2016)</i>						
a	Moormann and Verfondern (1987)	UO ₂ , 700–2400°C, 500μm	6.7×10^{-9}	165	–	–
b	Myers (1987)	UO ₂ , 350μm	3.3×10^{-9}	165	–	–
c	Myers (1987)	UO ₂ , 500μm	6.7×10^{-9}	165	–	–
d	Amian et al. (1982)	UO ₂ , 1000–1500°C	6.7×10^{-10}	165	–	–
e	Nabielek et al. (1977)	UO ₂ , 800–1500°C, 500μm	3.4×10^{-9}	213	–	–
f	Brown and Faircloth (1976)	UO ₂ , 1000–1400°C, 500μm	2.4×10^{-7}	269	–	–
<i>Diffusion coefficient estimates based on the AGR-1 experiment</i>						
1	Base irradiation	UCO	6.80×10^{-9} (24.0%)	161.17 (22.9%)	–	–
2	Safety tests	UCO	n/a	n/a	–	–
<i>Diffusion coefficient estimates based on the AGR-2 experiment</i>						
3	Base irradiation	UCO/UO ₂	7.80×10^{-9} (16.6%)	131.021 (26.6%)	–	–
4	Base irradiation	UO ₂	6.98×10^{-9} (27.5%)	133.720 (58.2%)	–	–
5	Base irradiation	UCO	7.19×10^{-9} (8.2%)	160.763 (10.8%)	–	–
6	Safety tests	UCO	2.32×10^{-5} (14.0%)	403.007 (7.6%)	–	–
<i>Diffusion coefficient estimates based on the AGR-1 and -2 experiments</i>						
7	Base irradiation	UCO & UO ₂ (65pts)	7.40×10^{-9}	129.036	–	–
8	Base irradiation	UCO (53pts)	8.64×10^{-9}	152.380	–	–
9	Safety tests	Combined datasets (13pts)	1.13×10^{-8}	81.935	–	–



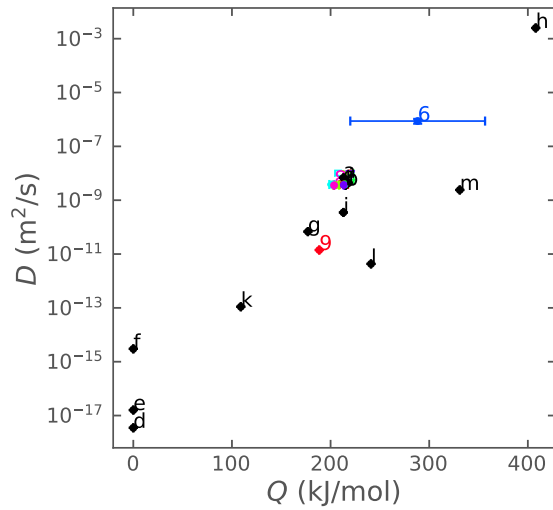
(a) D (m^2/s) vs. Q (kJ/mol)



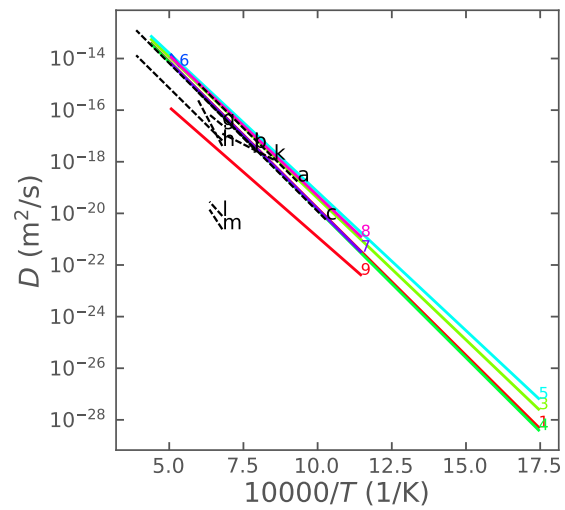
(b) D (m^2/s) vs. $10000/T$ ($1/\text{K}$)

Fig. 24. Ag diffusion coefficients in PyC.

	Reference	Notes	D_1 (m^2/s)	Q_1 (kJ/mol)	D_2 (m^2/s)	Q_2 (kJ/mol)
<i>Literature-reported diffusion coefficients (Collin, 2016)</i>						
a	Chernikov et al. (1985)	1400–1700°C, 1.84 g/cm ³	5.3×10^{-4}	192	–	–
b	Amian et al. (1982)	1000–1500°C	5.3×10^{-9}	154	–	–
c	Moormann and Verfondern (1987)	700–2000°C	5.3×10^{-9}	154	–	–
d	Offermann (1977)		1.0×10^{-8}	164	–	–
<i>Diffusion coefficient estimates based on the AGR-1 experiment</i>						
1	Base irradiation	UCO	5.73×10^{-9} (17.9%)	137.28 (27.7%)	–	–
2	Safety tests	UCO	n/a	n/a	–	–
<i>Diffusion coefficient estimates based on the AGR-2 experiment</i>						
3	Base irradiation	UCO/VO ₂	5.52×10^{-9} (11.2%)	144.751 (10.3%)	–	–
4	Base irradiation	VO ₂	6.19×10^{-9} (35.7%)	133.026 (29.7%)	–	–
5	Base irradiation	UCO	5.30×10^{-9} (11.4%)	151.345 (8.2%)	–	–
6	Safety tests	UCO	1.03×10^{-7} (9.7%)	273.350 (16.4%)	–	–
<i>Diffusion coefficient estimates based on the AGR-1 and -2 experiments</i>						
7	Base irradiation	UCO & VO ₂ (65pts)	5.46×10^{-9}	164.456	–	–
8	Base irradiation	UCO (53pts)	4.82×10^{-9}	158.275	–	–
9	Safety tests	Combined datasets (13pts)	2.15×10^{-8}	223.662	–	–



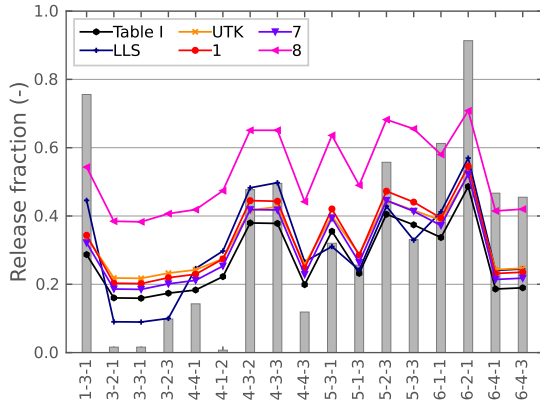
(a) D (m²/s) vs. Q (kJ/mol)



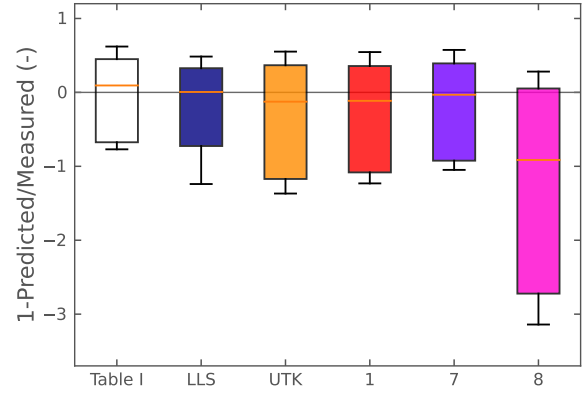
(b) D (m²/s) vs. $10000/T$ (1/K)

Fig. 25. Ag diffusion coefficients in SiC.

	Reference	Notes	D_1 (m²/s)	Q_1 (kJ/mol)	D_2 (m²/s)	Q_2 (kJ/mol)
<i>Literature-reported diffusion coefficients (Collin, 2016)</i>						
a	Nabielek et al. (1977)	800–1500°C, upper limit	6.8×10^{-9}	213	–	–
b	Amian et al. (1982)	1000–1500°C	3.6×10^{-9}	215	–	–
c	Moormann and Verfondern (1987)	700–2400°C	3.6×10^{-9}	215	–	–
d	López-Honorato et al. (2010)	950°C	3.5×10^{-18}	–	–	–
e	López-Honorato et al. (2010)	1150°C	1.6×10^{-17}	–	–	–
f	López-Honorato et al. (2010)	1500°C	3.0×10^{-15}	–	–	–
g	Fukuda et al. (1989)	1200–1400°C	6.8×10^{-11}	177	–	–
h	Bullock (1984)	1200–1500°C	2.5×10^{-3}	408	–	–
i	Chernikov et al. (1985)	1200–2400°C	3.5×10^{-10}	213	–	–
j	Amian and Stöver (1983)	1000–1500°C	4.5×10^{-9}	218	–	–
k	van der Merwe (2009)	900–1300°C	1.1×10^{-13}	109	–	–
l	Friedland et al. (2009)	1200–1400°C	4.3×10^{-12}	241	–	–
m	Friedland et al. (2011)	1200–1400°C	2.4×10^{-9}	331	–	–
<i>Diffusion coefficient estimates based on the AGR-1 experiment</i>						
1	Base irradiation	UCO	3.86×10^{-9} (12.1%)	213.35 (2.0%)	–	–
2	Safety tests		n/a	n/a	–	–
<i>Diffusion coefficient estimates based on the AGR-2 experiment</i>						
3	Base irradiation	UCO & UO ₂	3.63×10^{-9} (10.8%)	205.538 (1.5%)	–	–
4	Base irradiation	UO ₂	3.90×10^{-9} (13.2%)	214.572 (0.7%)	–	–
5	Base irradiation	UCO	3.83×10^{-9} (4.5%)	201.344 (1.3%)	–	–
6	Safety tests	UCO	8.71×10^{-7} (19.8%)	288.299 (23.7%)	–	–
<i>Diffusion coefficient estimates based on the AGR-1 and -2 experiments</i>						
7	Base irradiation	UCO & UO ₂ (65pts)	3.68×10^{-9}	213.445	–	–
8	Base irradiation	UCO (53pts)	3.58×10^{-9}	203.544	–	–
9	Safety tests	Combined datasets (13pts)	1.41×10^{-11}	188.519	–	–

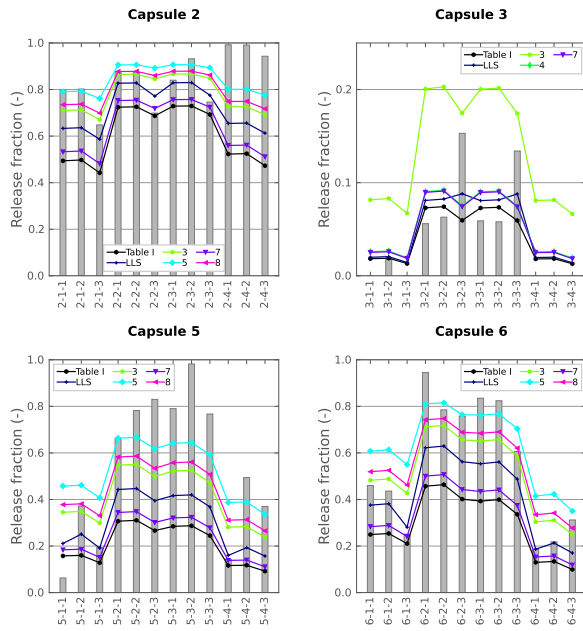


(a) Release fraction results

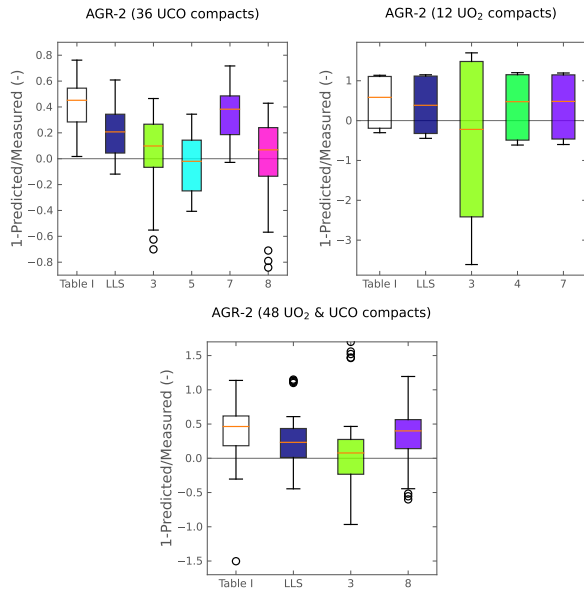


(b) Residuals

Fig. 26. Comparison of the measured and the computed Ag release fractions during the AGR-1 base irradiation with intact particles.



(a) Release fraction results



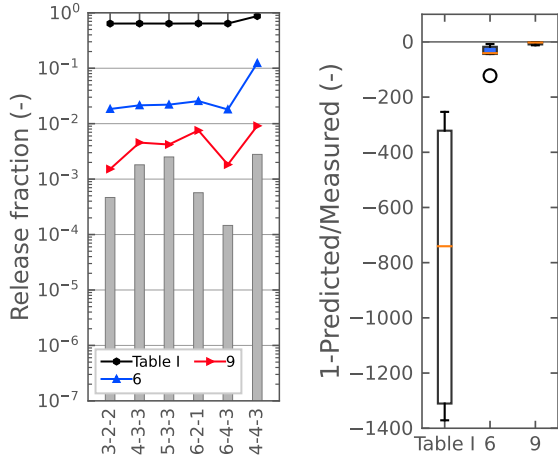
(b) Residuals

Fig. 27. Comparison of the measured and the computed Ag release fractions during the AGR-2 base irradiation of intact particles.

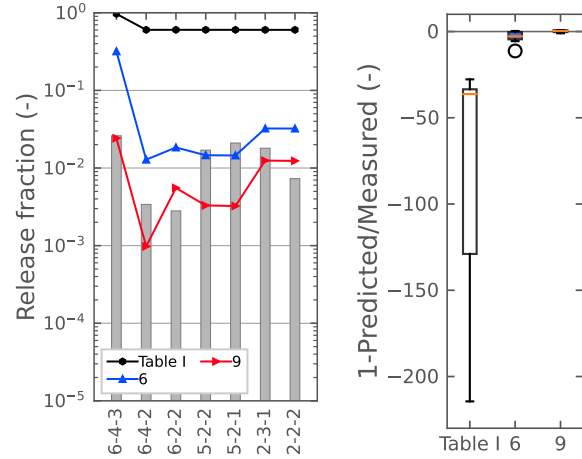
- 1) In the first assessment type, only 36 UCO compacts were considered. The best agreement with the measured data was obtained with case 5, in which the diffusion coefficients were estimated based solely on the AGR-2 UCO compacts. Case 5 was followed by case 8, in which the diffusion coefficients were estimated based on combined AGR-1&-2 UCO compacts. Code predictions based on LLS-informed diffusion coefficients (Simon et al., 2022) slightly improved the release fractions, as compared against the predictions made by using the diffusion coefficients listed in Table I. However, the release fractions are still underpredicted in comparison to the measured data.
- 2) In the second assessment type, only 12 UO₂ compacts were considered. All code predictions (except for case 3) behaved relatively similar to what was seen in the measured data. In case 3, the diffusion coefficients were estimated based on all 48 AGR-2 UCO and UO₂ compacts. Note that the measured AGR-2 release fractions for UCO compacts are relatively larger than those measured for UO₂ compacts; thus, the diffusion coefficient estimates for case 3 were dominated by the AGR-2 UCO compacts in the calibration process.
- 3) In the third assessment type, the assessment was performed for all 48 AGR-2 UCO and UO₂ compacts. Code predictions based on the case 3 diffusion coefficients yielded the best agreement with the measured data. Code predictions using LLS-informed diffusion coefficients (Simon et al., 2022) slightly improved the release fractions in comparison to predictions based on the diffusion coefficients listed in Table I. However, the release fractions remain underpredicted when compared to the measured data.

Figure 28 shows Ag release fractions from the AGR-1&-2 safety heating tests for the *intact* particles. As stated earlier, due to the scarcity of the AGR-1 safety data, the Ag diffusion coefficients were estimated based on the AGR-2 data only and the combined AGR-1&-2 data. In cases 6 and 9, the new diffusion coefficient estimates enhance the release fraction predictions by several orders of magnitude in comparison with the results obtained using the diffusion coefficients listed in Table I. Case 9 in particular yielded the best agreement with the measured data.

Figure 29 shows Ag release fractions from the AGR-1&-2 safety heating tests for the *failed* particles. In this assessment, BISON predictions using the new diffusion coefficient estimates were compared to independent measured datasets (i.e., the datasets not used in the calibration) for cross-validation purposes. Similarly, in cases 6 and 9, the new diffusion coefficient estimates enhance the release fraction predictions by several orders of magnitude in comparison with the results obtained using the diffusion coefficients listed in Table I. Case 9 in particular yields the best agreement with the measured data. This cross-validation exercise establishes more confidence in the estimated diffusion coefficients for Ag to assess how the release fraction results using these diffusion coefficients will generalize to an independent dataset.

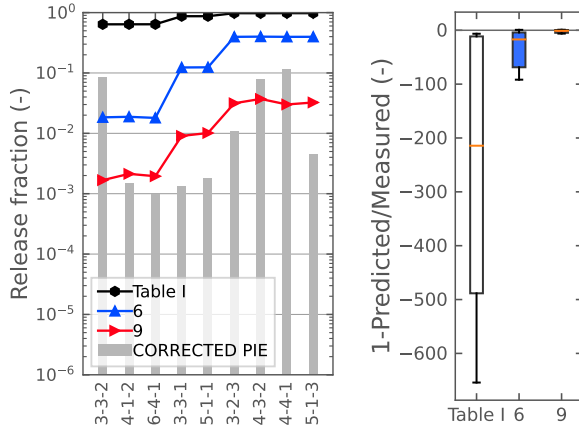


(a) AGR-1 safety heating tests

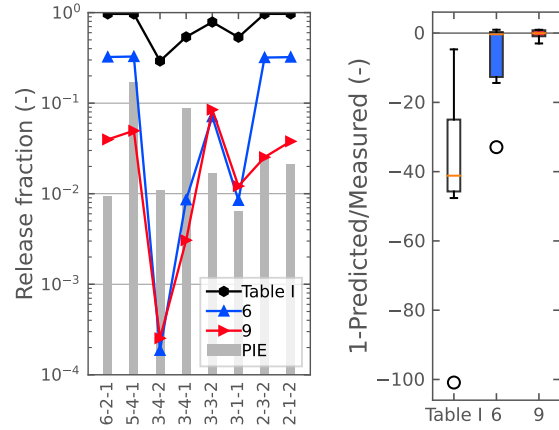


(b) AGR-2 safety heating tests

Fig. 28. Comparison of measured and computed Ag release fractions during the safety heating tests with intact particles.



(a) AGR-1 safety heating tests



(b) AGR-2 safety heating tests

Fig. 29. Comparison of measured and computed Ag release fractions during the safety heating tests conducted on the failed particles.

2) Cs results

The calibration results from this study include diffusion coefficient estimates for Cs in the kernel (Figure 30), PyC (Figure 31), and SiC (Figure 32) layers, based on AGR-1, AGR-2, and combined AGR-1&-2 PIE data. The literature-reported Cs diffusion coefficients from Collin (2016) are also provided in these plots, and are denoted by alphabetical letters.

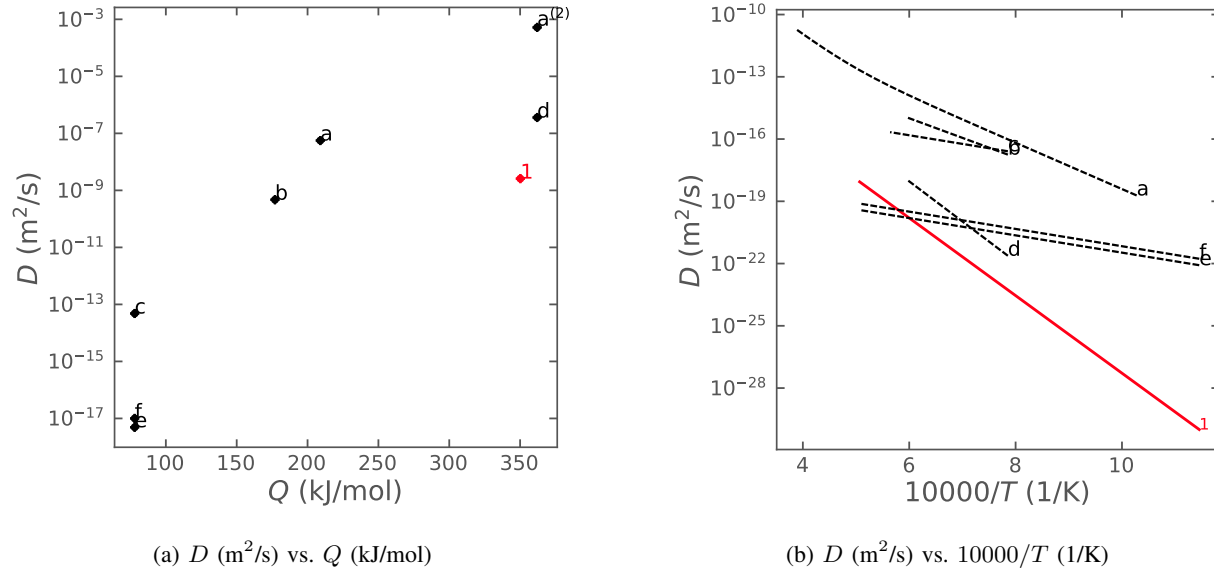
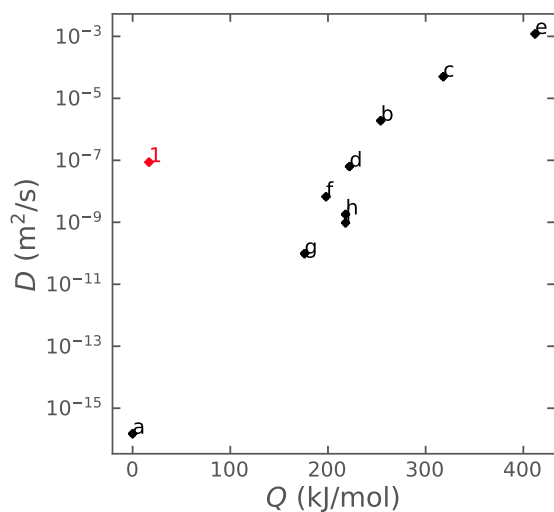
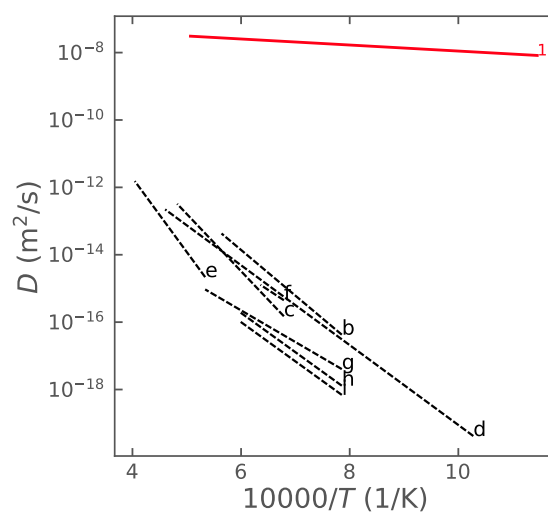


Fig. 30. Cs diffusion coefficients in the kernel.

	Reference	Notes	D_1 (m^2/s)	Q_1 (kJ/mol)	D_2 (m^2/s)	Q_2 (kJ/mol)
<i>Literature-reported diffusion coefficients (Collin, 2016)</i>						
a	Moormann and Verfondern (1987)	UO ₂ , 700–2400°C, 500 μm diameter	5.6×10^{-8}	209	5.2×10^{-4}	362
b	Fukuda et al. (1989)	UO ₂ , 1000–1450°C, 500 μm diameter	4.7×10^{-10}	177	–	–
c	Amian et al. (1982)	UO ₂ , 1000–1600°C	4.8×10^{-14}	78	–	–
d	Brown and Faircloth (1976)	UO ₂ , 1000–1500°C, grain 10–50 μm	3.6×10^{-7}	362	–	–
e	Myers (1987)	UO ₂ , 350 μm diameter	4.9×10^{-18}	78	–	–
f	Myers (1987)	UO ₂ , 500 μm diameter	1.0×10^{-17}	78	–	–
<i>This study</i>						
1	AGR-1&-2 combined intact	UCO, base+safety, 21 pts	2.585×10^{-9}	350.166	–	–



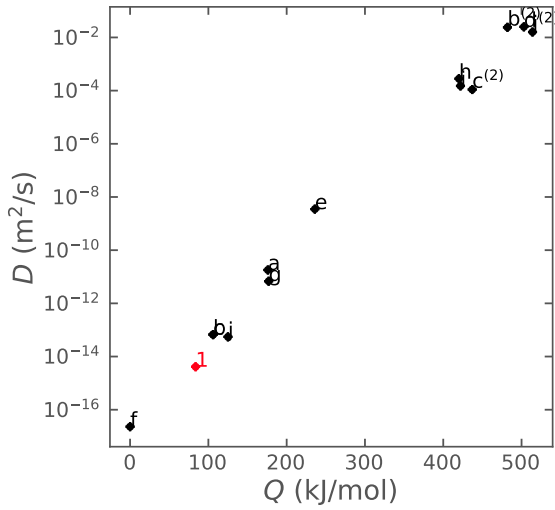
(a) D (m^2/s) vs. Q (kJ/mol)



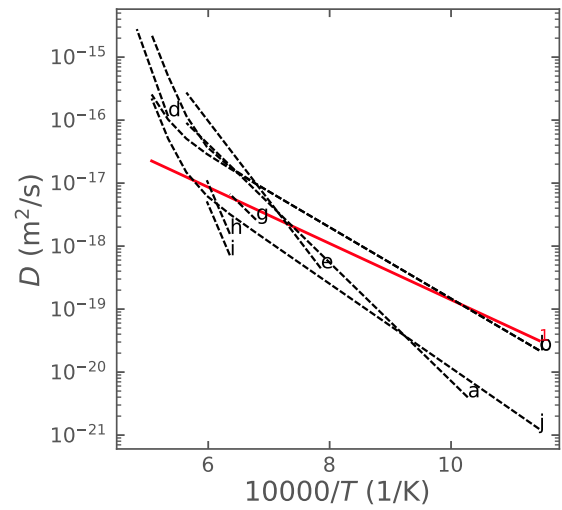
(b) D (m^2/s) vs. $10000/T$ ($1/\text{K}$)

Fig. 31. Cs diffusion coefficients in PyC.

	Reference	Notes	D_1 (m^2/s)	Q_1 (kJ/mol)	D_2 (m^2/s)	Q_2 (kJ/mol)
<i>Literature-reported diffusion coefficients (Collin, 2016)</i>						
a	Gudkov et al. (1989)	1000°C	1.5×10^{-16}	—	—	—
b	Amian et al. (1982)	1000–1600°C	1.9×10^{-6}	254	—	—
c	Myers and Bell (1979)	1200–1850°C	5.0×10^{-5}	318	—	—
d	Moormann and Verfondern (1987)	700–2000°C	6.3×10^{-8}	222	—	—
e	Hayashi and Fukuda (1990)	1600–2300°C	1.2×10^{-3}	412	—	—
f	Fukuda et al. (1989)	1200–1400°C	6.7×10^{-9}	198	—	—
g	Gethard and Zumwalt (1967)	1000–1650°C	9.7×10^{-11}	176	—	—
h	Brown and Faircloth (1976)	1000–1500°C, 1.8 g/cm^3	1.8×10^{-9}	218	—	—
i	Brown and Faircloth (1976)	1000–1500°C, 1.9 g/cm^3	9.6×10^{-10}	218	—	—
<i>This study</i>						
1	AGR-1&-2 combined intact	UCO, base+safety, 21pts	8.73×10^{-8}	16.722	—	—



(a) D (m²/s) vs. Q (kJ/mol)



(b) D (m²/s) vs. $10000/T$ (1/K)

Fig. 32. Cs diffusion coefficients in SiC.

	Reference	Notes	D_1 (m ² /s)	Q_1 (kJ/mol)	D_2 (m ² /s)	Q_2 (kJ/mol)
<i>Literature-reported diffusion coefficients (Collin, 2016)</i>						
a	Moormann and Verfondern (1987)	700–1500°C	1.8×10^{-11}	176	–	–
b	Myers (1984)	upper limit	6.7×10^{-14}	106	2.4×10^{-2}	482
c	Myers (1984)	lower limit	6.7×10^{-14}	106	1.1×10^{-4}	437
d	Minato et al. (1993)	1600–1900°C	2.5×10^{-2}	503	–	–
e	Amian et al. (1982); Amian and Stöver (1983)	1000–1600°C	3.5×10^{-9}	236	–	–
f	Gudkov et al. (1989)	1000°C	2.3×10^{-17}	–	–	–
g	Fukuda et al. (1989)	1200–1400°C, upper limit	6.8×10^{-12}	177	–	–
h	Ogawa et al. (1985)	1300–1500°C, upper limit	2.8×10^{-4}	420	–	–
i	Ogawa et al. (1985)	1300–1500°C, lower limit	1.5×10^{-4}	422	–	–
j	Christ (1985)	Γ fluence, $E > 0.1$ MeV	$5.5e^{\Gamma/5} \times 10^{-14}$	125	1.6×10^{-2}	514
<i>This study</i>						
l	AGR-1&-2 combined intact	UCO, base+safety, 21pts	4.13×10^{-15}	83.688	–	–

Figures 33 and 34 show, respectively, the Cs release fractions from the base irradiation and safety heating tests for the *intact* particles. In this calibration study, the measured release fractions during both the AGR-1&2 base irradiation and safety heating tests are of similar orders of magnitude. For this reason, the diffusion coefficients were estimated based on combining all the AGR-1&2 intact particles at base irradiation and safety heating tests, resulting in 21 data points in total. In the calibration process, the measured PIE data were considered as the mean of the reported minimum and maximum PIE values. Overall, with the new diffusion coefficient estimates, the release fraction predictions are improved (i.e., case 1) several orders of magnitude in comparison with the results obtained using the diffusion coefficients listed in Table I, and also showed better agreement with the measured data.

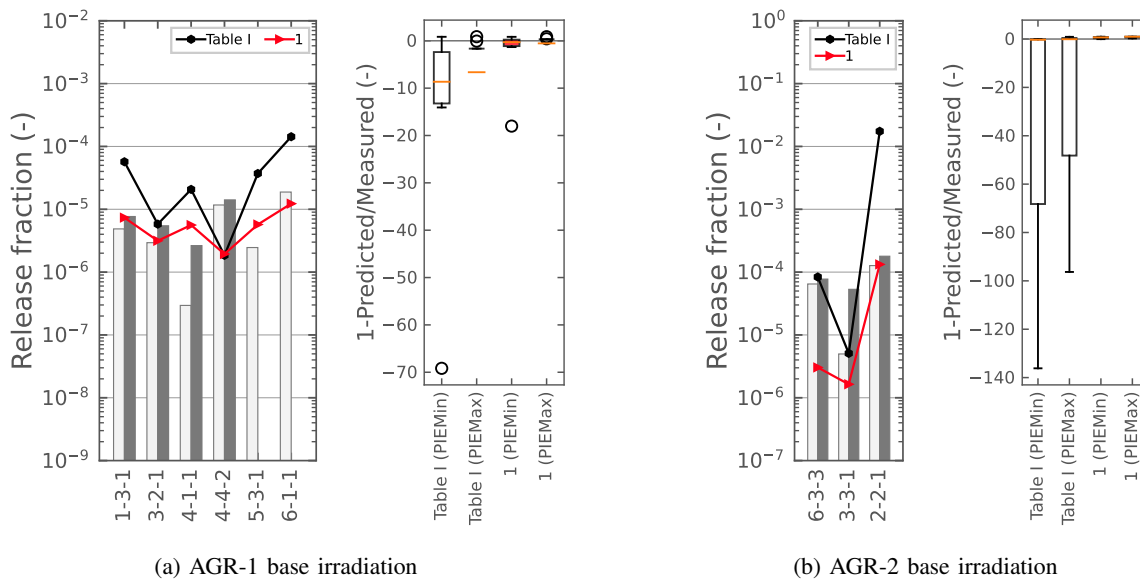
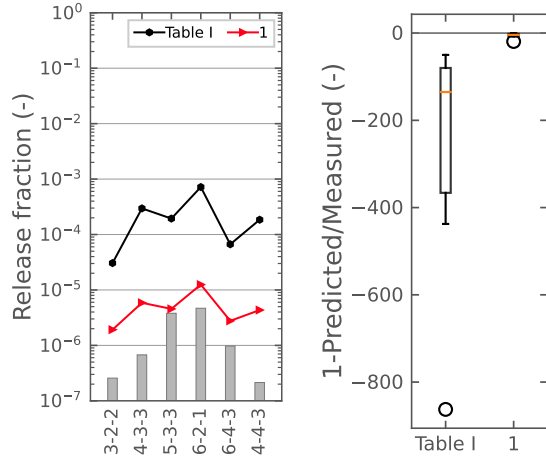
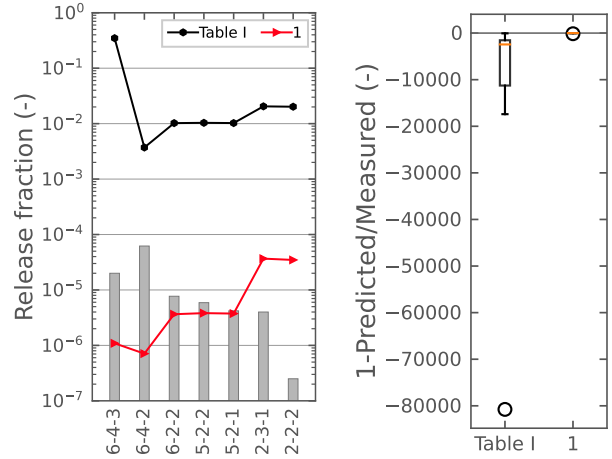


Fig. 33. Comparison of the measured and the computed Cs release fractions during the base irradiation with intact particles.

Figures 35 and 36 respectively show the Cs release fractions from the base irradiation and safety heating tests with the *failed* particles. In this assessment, BISON predictions using the new diffusion coefficient estimates were compared against independent measured datasets (i.e., the datasets not used in the calibration) for cross-validation purposes.

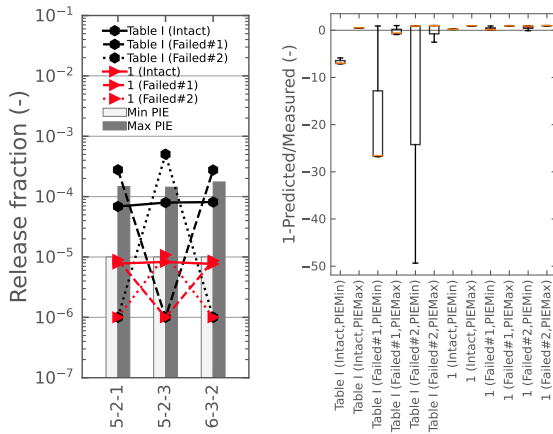


(a) AGR-1 safety heating tests

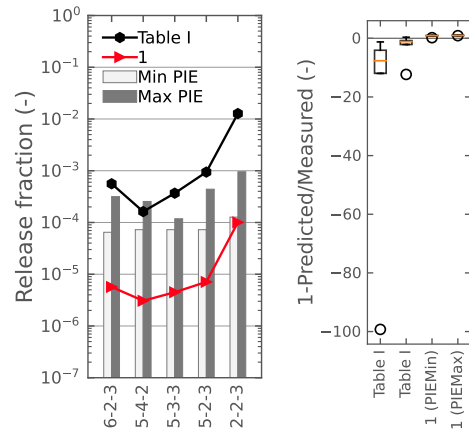


(b) AGR-2 safety heating tests

Fig. 34. Comparison of the measured and the computed Cs release fractions during the safety heating tests with intact particles.

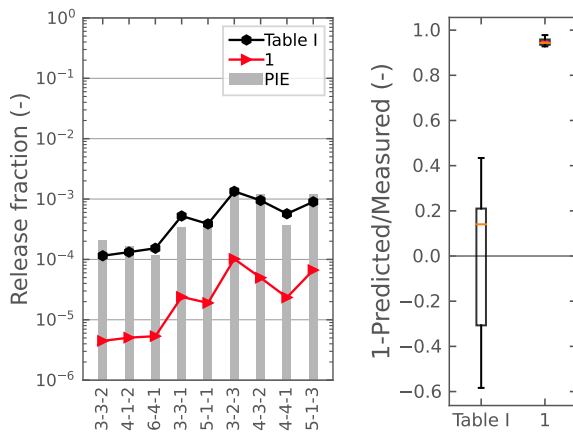


(a) AGR-1 base irradiation

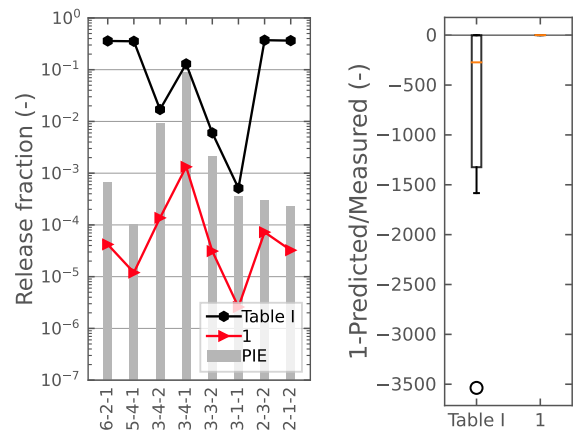


(b) AGR-2 base irradiation

Fig. 35. Comparison of measured and computed Cs release fractions during the base irradiation with failed particles.



(a) AGR-1 safety heating tests



(b) AGR-2 safety heating tests

Fig. 36. Comparison of measured and computed Cs release fractions during the safety heating tests with failed particles.

3) Sr results

The calibration results from this study include diffusion coefficient estimates for Sr in the kernel (Figure 37), PyC (Figure 38), and SiC (Figure 39) layers, based on AGR-1, AGR-2, and combined AGR-1&2 PIE data. The literature-reported Cs diffusion coefficients from Collin (2016) are also provided in these plots, and are denoted by alphabetical letters.

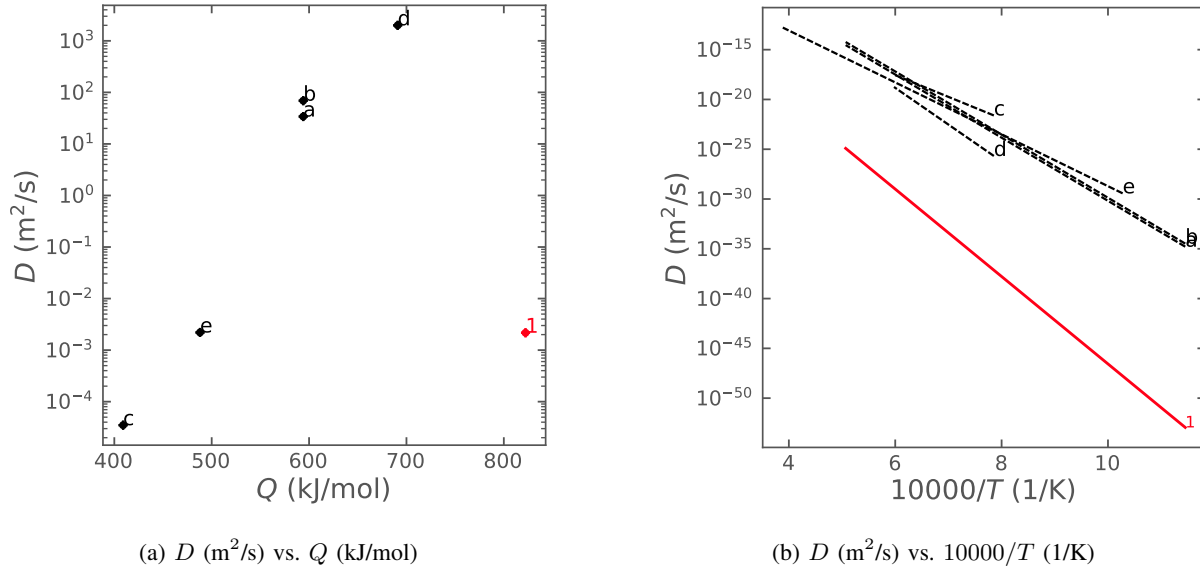
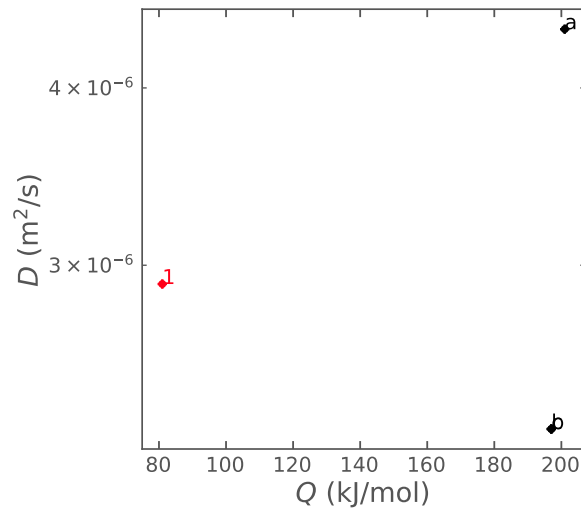
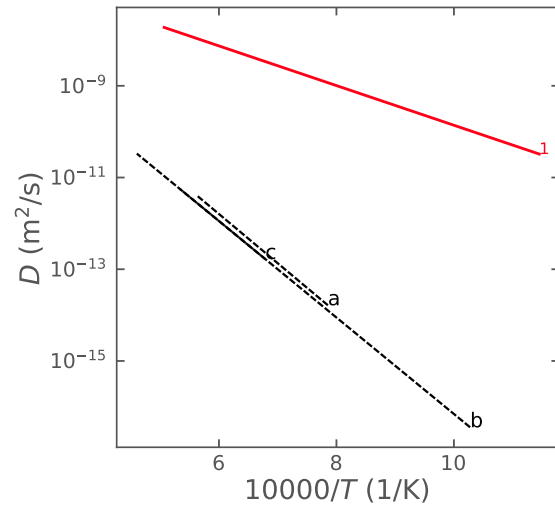


Fig. 37. Sr diffusion coefficients in the kernel.

	Reference	Notes	D_1 (m ² /s)	Q_1 (kJ/mol)	D_2 (m ² /s)	Q_2 (kJ/mol)
<i>Literature-reported diffusion coefficients (Collin, 2016)</i>						
a	Myers (1987)	UO ₂ , 350 μ m diameter	$3.4 \times 10^{+1}$	594	—	—
b	Myers (1987)	UO ₂ , 500 μ m diameter	$6.9 \times 10^{+1}$	594	—	—
c	Amian et al. (1982)	UO ₂ , 1000–1500°C	3.5×10^{-5}	409	—	—
d	Brown and Faircloth (1976)	UO ₂ , 1500–1650°C, 500 μ m diameter	$2.0 \times 10^{+3}$	691	—	—
e	Moormann and Verfondern (1987)	UO ₂ , 700–2400°C, 500 μ m diameter	2.2×10^{-3}	488	—	—
<i>This study</i>						
1	AGR-1&2 combined intact	UCO, base+safety (21pts)	2.17×10^{-3}	822.274	—	—



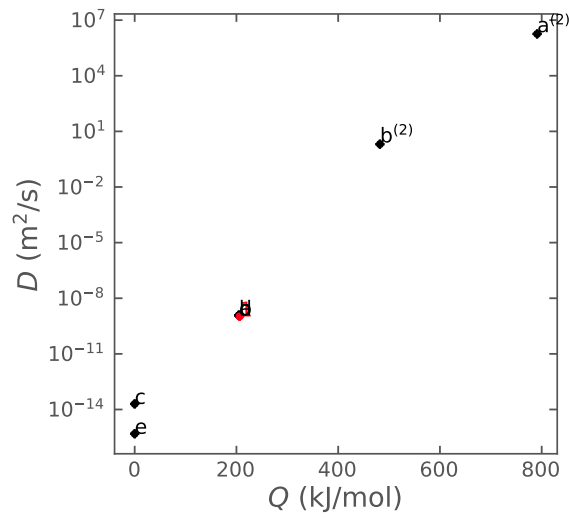
(a) D (m^2/s) vs. Q (kJ/mol)



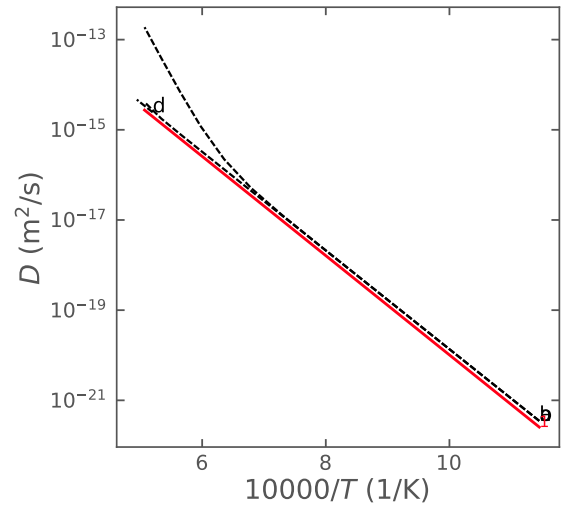
(b) D (m^2/s) vs. $10000/T$ ($1/\text{K}$)

Fig. 38. Sr diffusion coefficients in PyC.

	Reference	Notes	D_1 (m^2/s)	Q_1 (kJ/mol)	D_2 (m^2/s)	Q_2 (kJ/mol)
<i>Literature-reported diffusion coefficients (Collin, 2016)</i>						
a	Gethard and Zumwalt (1967)	1000–1600°C	4.4×10^{-6}	201	–	–
b	Moormann and Verfondern (1987)	700–2000°C	2.3×10^{-6}	197	–	–
c	Myers and Bell (1974)	1200–1650°C	2.3×10^{-6}	197	–	–
<i>This study</i>						
1	AGR-1&-2 - combined intact	UCO, base+safety (21pts)	2.91×10^{-6}	80.987	–	–



(a) D (m²/s) vs. Q (kJ/mol)



(b) D (m²/s) vs. $10000/T$ (1/K)

Fig. 39. Sr diffusion coefficients in SiC.

	Reference	Notes	D_1 (m²/s)	Q_1 (kJ/mol)	D_2 (m²/s)	Q_2 (kJ/mol)
<i>Literature-reported diffusion coefficients (Collin, 2016)</i>						
a	Verfondere and Müller (1991)		1.2×10^{-9}	205	$1.8 \times 10^{+6}$	791
b	Moormann and Verfondere (1987)		1.2×10^{-9}	205	204×10^{-2}	482
c	Fukuda and Iwamoto (1975)	1750°C	2.0×10^{-14}	–	–	–
d	Fukuda and Iwamoto (1978)	1650–1850°C	1.2×10^{-9}	205	–	–
e	Förthmann and Gyarmati (1975)	1400°C	4.9×10^{-16}	–	–	–
<i>This study</i>						
1	AGR-1&-2 combined intact	UCO, base+safety (21pts)	1.04×10^{-9}	206.222	–	–

Figures 40 and 41 respectively show Sr release fractions from the base irradiation and safety heating tests with the *intact* particles. In this calibration study, the measured release fractions for both AGR-1&-2 intact particles at base irradiation and safety heating tests are on similar orders of magnitude. As a result, the diffusion coefficients were estimated based on all the combined AGR-1&-2 intact particles at base irradiation and safety heating tests, resulting in 21 data points in total. In the calibration process, measured PIE data are considered as the mean of the reported minimum and maximum PIE values. With the new diffusion coefficient estimates, the release fraction predictions are improved (i.e., case 1) by several orders of magnitude compared to the results obtained by using the diffusion coefficients listed in Table I, and show better agreement with the measured data.

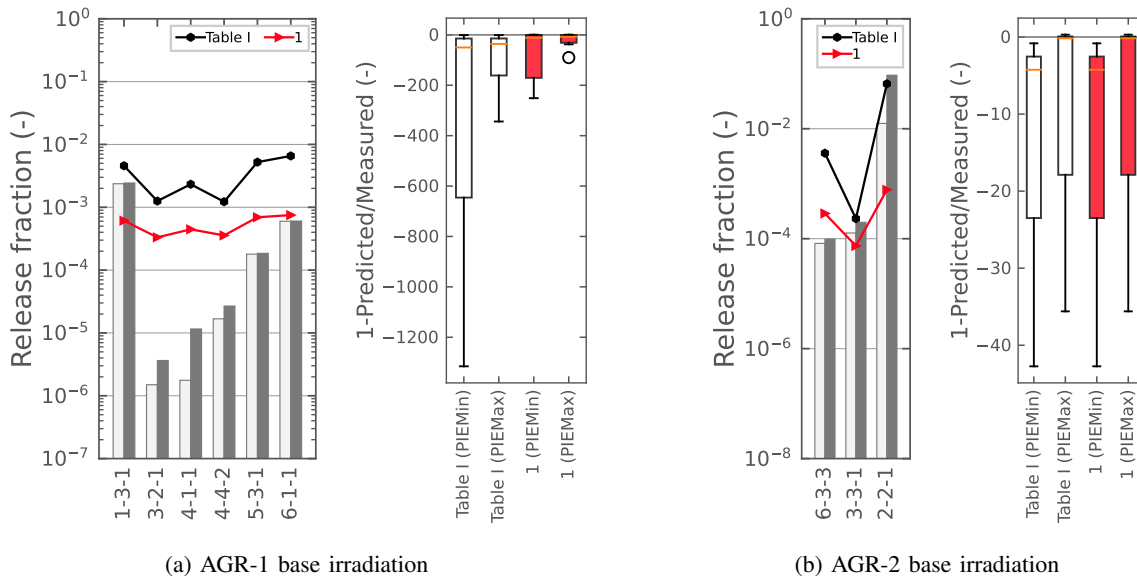
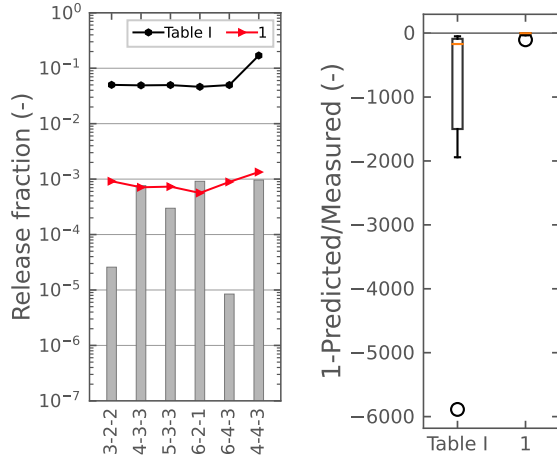
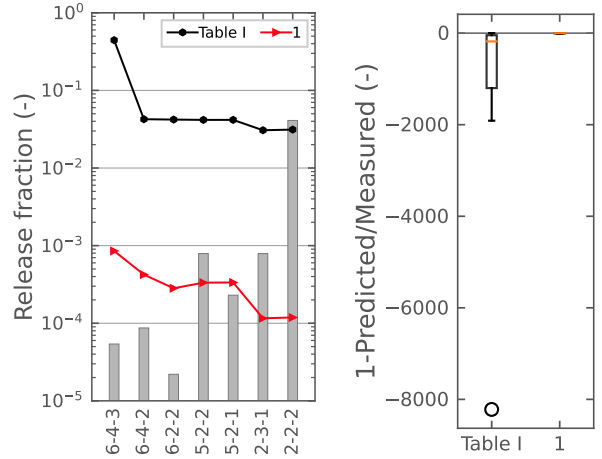


Fig. 40. Comparison of the measured and the computed Sr release fractions during the base irradiation with intact particles

Figures 42 and 43 show, respectively, Sr release fractions from the base irradiation and safety heating tests with the *failed* particles. In this assessment, BISON predictions using the new diffusion coefficient estimates were compared to independent measured datasets (i.e., the datasets not used in the calibration) for cross-validation purposes.

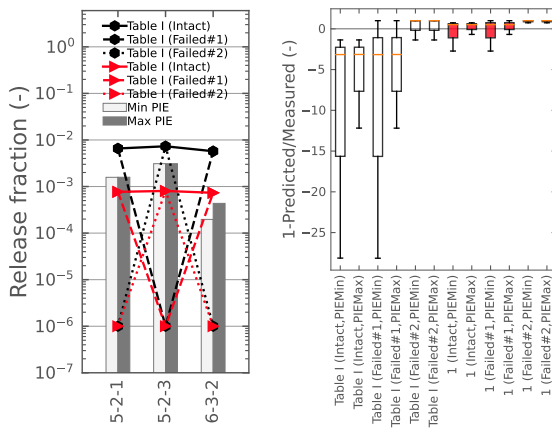


(a) AGR-1 safety heating tests

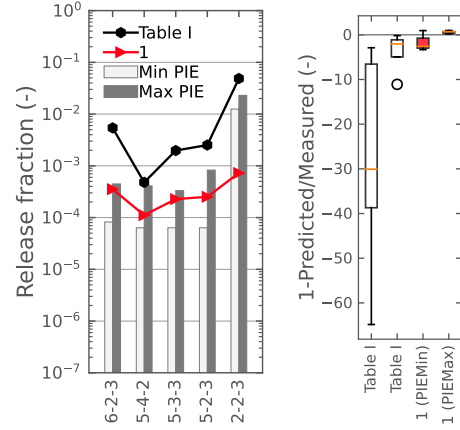


(b) AGR-2 safety heating tests

Fig. 41. Comparison of the measured and the computed Sr release fractions during the safety heating tests with intact particles.

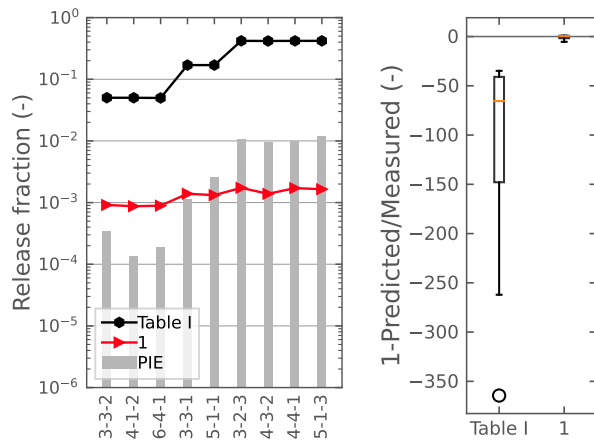


(a) AGR-1 base irradiation

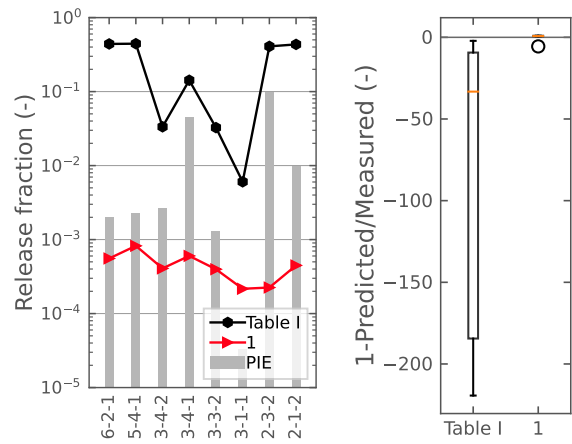


(b) AGR-2 base irradiation

Fig. 42. Comparison of the measured and the computed Sr release fractions during the base irradiation with failed particles.



(a) AGR-1 safety heating tests



(b) AGR-2 safety heating tests

Fig. 43. Comparison of the measured and the computed Sr release fractions during the safety heating tests with failed particles.

4) Kr results

Due to the scarcity of data in the available AGR experiments, physical calibration results were not obtained for Kr diffusion coefficients. The calibration based on the AGR-1 dataset was made infeasible by $n \leq p$, since there are only six data points available in the safety heating tests with the intact particles. For the AGR-2 and combined dataset conditions, no physical diffusion coefficients were estimated from the calibration activities. Instead, the literature-reported diffusion coefficients from Collin (2016) are provided for Kr in the kernel (Figure 44), PyC (Figure 45), and SiC (Figure 46) layers, which are denoted by alphabetical letters.

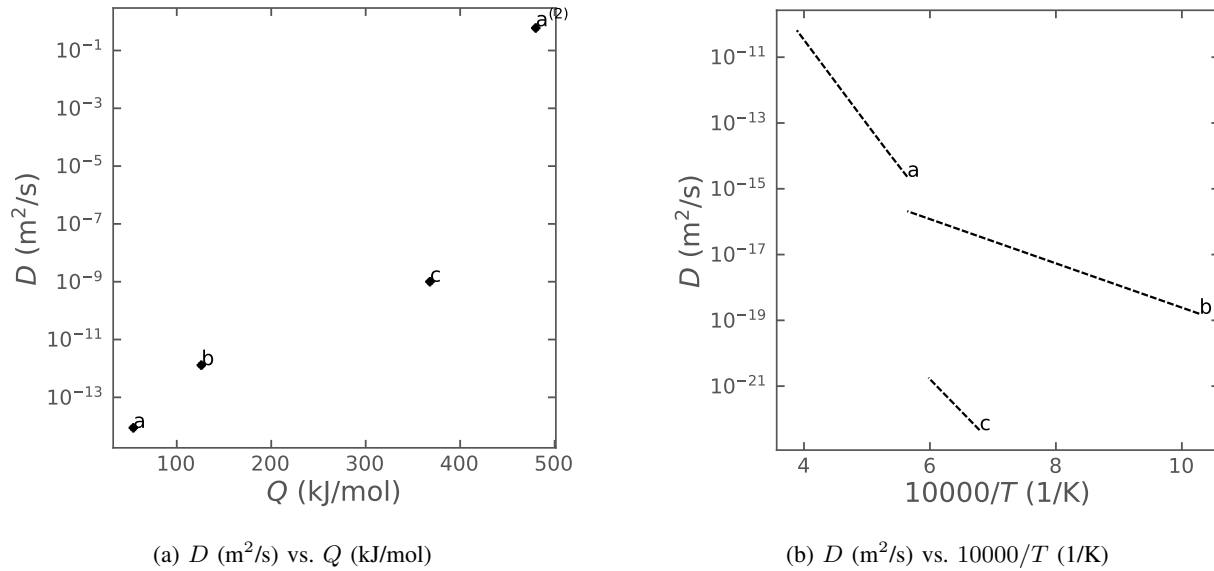
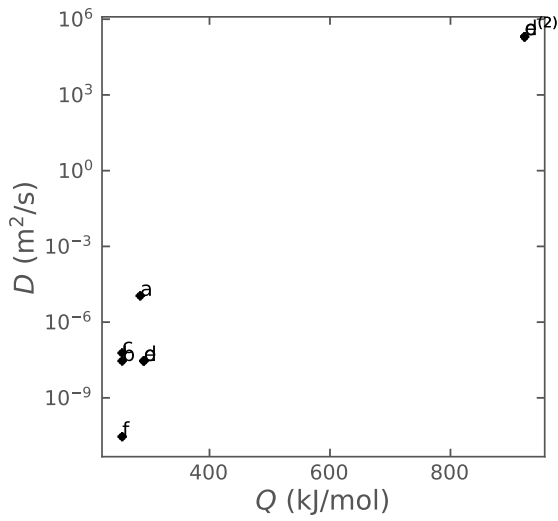
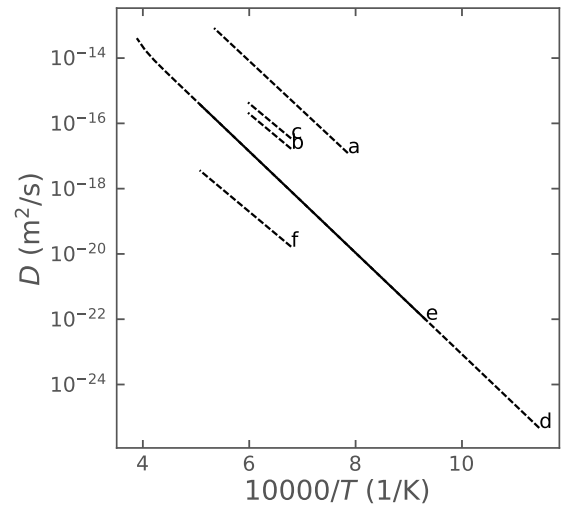


Fig. 44. Kr diffusion coefficients in the kernel.

	Reference	Notes	D_1 (m^2/s)	Q_1 (kJ/mol)	D_2 (m^2/s)	Q_2 (kJ/mol)
<i>Literature-reported diffusion coefficients (Collin, 2016)</i>						
a	Moormann and Verfonderen (1987)	UO ₂ , 1500–2400°C, 500 μm	8.8×10^{-15}	54	6.0×10^{-1}	480
b	Müller (1976); Moormann and Verfonderen (1987)	UO ₂ , 700–1500°C, 500 μm	1.3×10^{-12}	126	–	–
c	Chernikov et al. (1985)	UO ₂ , 1200–1450°C, 500 μm	1.0×10^{-9}	368	–	–



(a) D (m^2/s) vs. Q (kJ/mol)



(b) D (m^2/s) vs. $10000/T$ ($1/\text{K}$)

Fig. 45. Kr diffusion coefficients in PyC.

	Reference	Notes	D_1 (m^2/s)	Q_1 (kJ/mol)	D_2 (m^2/s)	Q_2 (kJ/mol)
<i>Literature-reported diffusion coefficients (Collin, 2016)</i>						
a	Chernikov et al. (1985)	1000–1650°C	1.1×10^{-5}	285	–	–
b	Fukuda et al. (1989)	1200–1500°C, upper limit	2.9×10^{-8}	255	–	–
c	Fukuda et al. (1989)	1200–1500°C, lower limit	6.0×10^{-8}	255	–	–
d	Goodin and Nabielek (1985)		2.9×10^{-8}	291	$2.0 \times 10^{+5}$	923
e	Moormann and Verfondern (1987)	800–2400°C	2.9×10^{-8}	291	$2.0 \times 10^{+5}$	923
f	Fukuda and Iwamoto (1975)	1200–1750°C, Xe values	2.9×10^{-11}	255	–	–

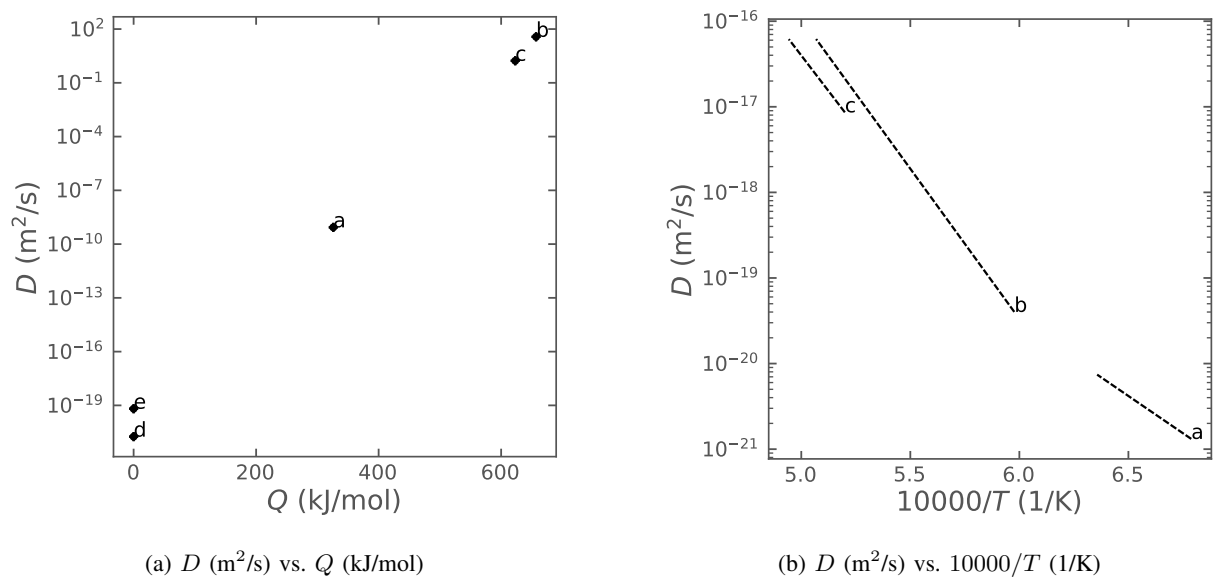


Fig. 46. Kr diffusion coefficients in SiC.

	Reference	Notes	D_1 (m²/s)	Q_1 (kJ/mol)	D_2 (m²/s)	Q_2 (kJ/mol)
<i>Literature-reported diffusion coefficients (Collin, 2016)</i>						
a	Fukuda and Iwamoto (1976)	1200–1400°C, Xe values	8.6×10^{-10}	326	–	–
b	Fukuda and Iwamoto (1976)	1400–1750°C, Xe values	3.7×10^{-11}	657	–	–
c	Fukuda and Iwamoto (1978)	1650–1850°C, Xe values	1.7×10^{-10}	623	–	–
d	Friedland et al. (2011)	1100°C, I values	1.8×10^{-21}	–	–	–
e	Friedland et al. (2011)	1200°C, I values	6.5×10^{-20}	–	–	–

E. Summary

The availability and reliability of diffusion coefficients were investigated for key radioactive species in the particle. The diffusion coefficients were estimated for Ag, Cs, and Sr in the kernel, PyC, and SiC layers, based on the AGR-1 and -2 integral release experiments and only considering intact particles in the calibration. Due to the scarcity of data from the available AGR experiments for Kr, no physical calibration results were obtained for Kr diffusion coefficients. The diffusion coefficient estimates and the surveyed empirical coefficients of the key radioactive species in the kernel, PyC, and SiC layers were also provided. Later, the newly estimated diffusion coefficients were assessed against the measured AGR-1&-2 data during base irradiation and safety heating tests with both intact and failed particles. As mentioned earlier, the assessments of the failed particles were not considered in the calibration process; thus, the cases involving failed particles became useful in the cross-validation that was conducted to establish greater confidence in the diffusion coefficient estimates and to assess how the release fraction results obtained by using these diffusion coefficients would generalize to an independent dataset. Overall, the release fraction predictions were improved using the newly estimated diffusion coefficients in terms of aligning with the measured data.

The calibration methodology was constructed to be repeatable—as well as expandable to include more data points, if needed. The availability of the AGR-3/4 experiments will allow for more data points in the calibration process, enabling better statistics for use in the estimation of diffusion coefficients.

V. EFFECTIVE DIFFUSIVITY COEFFICIENT

The material presented here is a subset of the information found in Toptan et al. (2022a). The governing steady-state equations of the elasticity, thermal conduction, and electrical conduction problems take similar mathematical forms (Table IV). Most approaches developed for solving conductive problems can also be extended to corresponding elastic problems, as well as to the simplified Fickian diffusion widely used for calculations in engineering applications. By considering heat conduction (see Equation 5) to be analogous with simplified Fickian diffusion (or fission product species conservation, see Equation 6), we can apply the same analytical homogenization methods to obtain the effective thermal conductivity (ETC) as used to obtain the EDC.

Based on our previous ETC-related work in Toptan et al. (2021), the effective medium theory (EMT) showed the best agreement for $\alpha > 1$ while differential effective medium theory (D-EMT) for $\alpha < 1$, where α is defined as the ratio of thermal conductivities of particles to continuous medium for the ETC calculations. In this study, we selected only the two recommended ETC models (see Table V) to determine whether our hypothesis was valid for EDC calculations.

The heat conduction is given by Equation 5. Fission product species conservation is given by Equation 6, where the mass flux is expressed as $\mathbf{J} = -D\nabla C$, using the diffusion coefficient, D (m^2/s), which is defined in a temperature-dependent Arrhenius form as:

$$D = \sum_i D_{0,i} \exp\left(-\frac{Q_i}{RT}\right), \quad (29)$$

where Q is the activation energy, R is the universal gas constant, and T is the temperature.

TABLE IV. Correspondence between elastic and conductive problems, taken from Deng and Zheng (2009).

Problem	Elasticity	Thermal Conductance	Electric Conductance
Corresponding quantities	Stress $\boldsymbol{\tau}$	Heat flux \mathbf{q}	Current \mathbf{J}
	Displacement \mathbf{u}	Temperature T	Electrical potential ϕ
	Strain $\boldsymbol{\epsilon} = \frac{1}{2}(\nabla \mathbf{u} + (\nabla \mathbf{u})^\top)$	Thermal gradient $\mathbf{g} = -\nabla T$	Electric field intensity $\mathbf{E} = -\nabla \phi$
	Elasticity tensor \mathbb{C}	Thermal conductivity tensor \mathbf{K}	Electric conductivity tensor $\boldsymbol{\sigma}$
Equilibrium eq.	$\nabla \cdot \boldsymbol{\tau} = 0$	$\nabla \cdot \mathbf{q} = 0$	$\nabla \cdot \mathbf{J} = 0$
Physical eq.	$\boldsymbol{\tau} = \mathbb{C} : \boldsymbol{\epsilon}$	$\mathbf{q} = \mathbf{K} \cdot \mathbf{g}$	$\mathbf{J} = \boldsymbol{\sigma} \cdot \mathbf{E}$

We performed several numerical experiments using the finite-element-based code BISON (Williamson et al., 2021), and assessed the recommended analytical models for EDC. These numerical experiments were conducted for a domain with randomly dispersed, mono-sized spherical particles featuring varying material properties.

A. Methods

Here, we describe the methodology for obtaining, in three main steps, the EDC from the FEAs, along with the problem settings in each, based on the converged concentration profile for the EDC.

Step 1. We create a three-dimensional (3-D) cubic computational domain for a representative volume element of material with randomly dispersed, mono-sized spheres (see Figure 47). The spheres are described in a diffuse manner by a field variable. This field variable equals one within the spheres, and varies continuously—but steeply—to zero within the secondary phase. The diffusive interface width

TABLE V. Recommended analytical methods for the ETC based on our previous work in Toptan et al. (2021). The nomenclature: k_e is the ETC; k_1 and v_1 are the thermal conductivity and volume fraction, respectively, of the continuous phase; k_2 and v_2 are the thermal conductivity and volume fraction, respectively, of the dispersed phase; and $\alpha = k_2/k_1$ is the ratio of the thermal conductivities of the dispersed phase to those of the continuous phase.

Model	Formulation	Notes
$\alpha < 1$ D-EMT	$\left(\frac{k_e - k_2}{k_1 - k_2}\right)^3 \frac{k_1}{k_e} = (1 - v_2)^3$	Roots of the third-order polynomial are computed accordingly, and the largest real root of the cubic equation is assigned to the ETC (Toptan et al., 2019).
$\alpha > 1$ EMT	$\sum_i v_i \left(\frac{k_i - k_e}{k_i + 2k_e}\right) = 0$	The <i>Bruggeman</i> (Bruggeman, 1935) obtained the following relation for a binary system: $\frac{k_e}{k_1} = \alpha A + \sqrt{\alpha^2 A^2 + \frac{\alpha}{2}}$ with $A = \frac{1}{4} \left(3v_2 - 1 + \frac{1}{\alpha} [2 - 3v_2]\right)$

is a user-controlled parameter, here set to 10% of the sphere diameter. Adaptive meshing is utilized to resolve the phase interface by using two levels of refinement in the periphery regions of each sphere. The distance between the centers of two adjacent spheres, d , is required to be at least one sphere diameter, D , in order to avoid overlap between the spheres (i.e., $d \geq d_{\min} = 1.05D$).

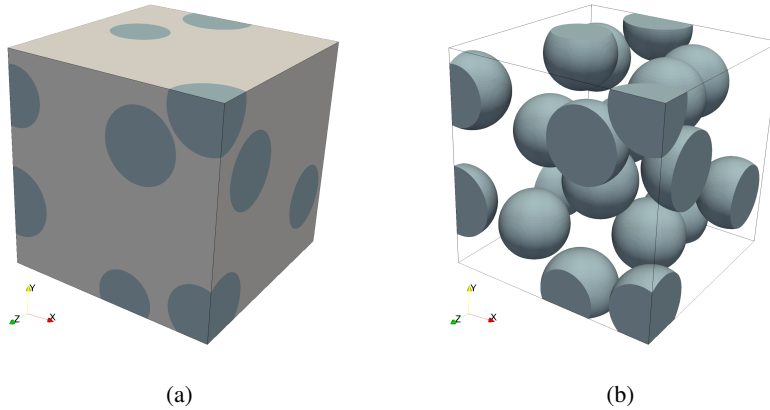


Fig. 47. 3-D constructed computational domain: (a) matrix with embedded spheres; (b) random distribution of mono-sized spheres (the matrix is hidden for ease of visibility). The characteristic domain length-to-particle radius, L/R , is 6. The volume fraction of the continuous matrix, v_1 , is 0.726. The minimum distance between the centers of two adjacent spheres is set to one sphere diameter, D (i.e., $d_{\min} = D$).

Step 2. Finite-element analysis (FEA) simulations are performed for different volume fractions in each numerical experiment. Different volume fractions are obtained by varying the number of spheres in the computational domain. The present study includes evaluation of EDC; therefore, only Equation 6 is solved. The diffusivity coefficients of both the host matrix and the spherical inclusions are chosen based on the analyses of interest. The diffusivity coefficient is weighted based on the volume fraction of each phase for a cell including both phases. The numerical simulations are performed under a packing fraction of up to approximately 40%.

Step 3. The EDC is calculated from the converged concentration field, using the relation from Mu et al. (2007):

$$D_{e,x} = \frac{\int_A \int D_b \left(\frac{\partial C}{\partial x} \right)_{x=L} dydz}{\frac{(C_2 - C_1)}{L} A}, \quad (30)$$

where D_b is the bulk diffusivity coefficient (or matrix diffusivity coefficient), C_1 and C_2 are the concentration values applied to each opposing surface in the unidirectional diffusion process, and A is the surface area. To obtain a single value for EDC from the set of simulations, an arithmetic mean of the diffusivity coefficients in the principal directions is employed:

$$D_e = \frac{1}{n} \left(\sum_{i=1}^n D_{e,i} \right), \quad (31)$$

where $D_{e,i}$ represents the diffusivity coefficient in each principal direction (via Equation 30), and n is the number of principal directions (i.e., $n = 3$ for 3-D).

B. Results & Discussion

The FEAs were performed for the computational domain at various volume fractions. The EDC was evaluated for randomly dispersed mono-sized spherical inclusions embedded in a continuous matrix, considering two cases: (1) the diffusivity coefficient of the particles is less than the continuous matrix ($\alpha = D_2/D_1 < 1$), and (2) the diffusivity coefficient of the particles exceeds the continuous matrix ($\alpha > 1$). The detailed results are provided and discussed. Note that $\alpha = 1$ corresponds to the homogeneous material; thus, it is not evaluated here.

The simulation results and model predictions are provided in terms of the diffusivity coefficients ratio of the effective to host matrix, D_e/D_1 , to understand the impact of spherical inclusions (with varying diffusivity coefficients) as a function of the volume fraction of the matrix, v_1 . For the computational considerations, the characteristic domain length-to-particle ratio, L/R , was set to 6 in these analyses—a value found sufficient in the parametric study performed in Toptan et al. (2021). Only the uncertainty around the mean FEA results varies with the chosen L/R ratio, which is indicated by the error bars around the FEA predictions.

1) Case I. The diffusivity coefficient of the particles is less than the continuous matrix ($\alpha < 1$).

Figure 48 shows the concentration profiles for the case featuring $\alpha < 1$ in each unidirectional diffusion process in the principal direction at a fixed volume fraction (i.e., 0.726) of the continuous matrix, v_1 , for the arbitrarily chosen $\alpha = 1 \times 10^{-4}$, 0.1, and 0.5. See Figure 47 for the actual particle locations with $v_1 = 0.726$. The FEA-predicted D_e was estimated based on the average values of realizations performed in all three principal directions (plotted in Figure 50a), as well as on the model predictions from both EMT and D-EMT. In this case, the diffusion gradient across the domain is relatively smooth at $\alpha = 0.5$ (see Figure 48c). The presence of the particles within the domain becomes more pronounced on the diffusion process as α approaches zero (see Figures 48a and 48b).

Figure 50a shows the model and FEA predictions for D_e/D_1 as a function of v_1 for the arbitrarily chosen $\alpha = 1 \times 10^{-4}$, 0.1, and 0.5. Unsurprisingly, introducing fewer diffusive particles into the system degrades its overall diffusivity coefficient. As expected, the material behaves homogeneously at $v_1 = 1$. The models behave similarly in regard to $\alpha = 0.5$, but significantly differ from each other as α becomes

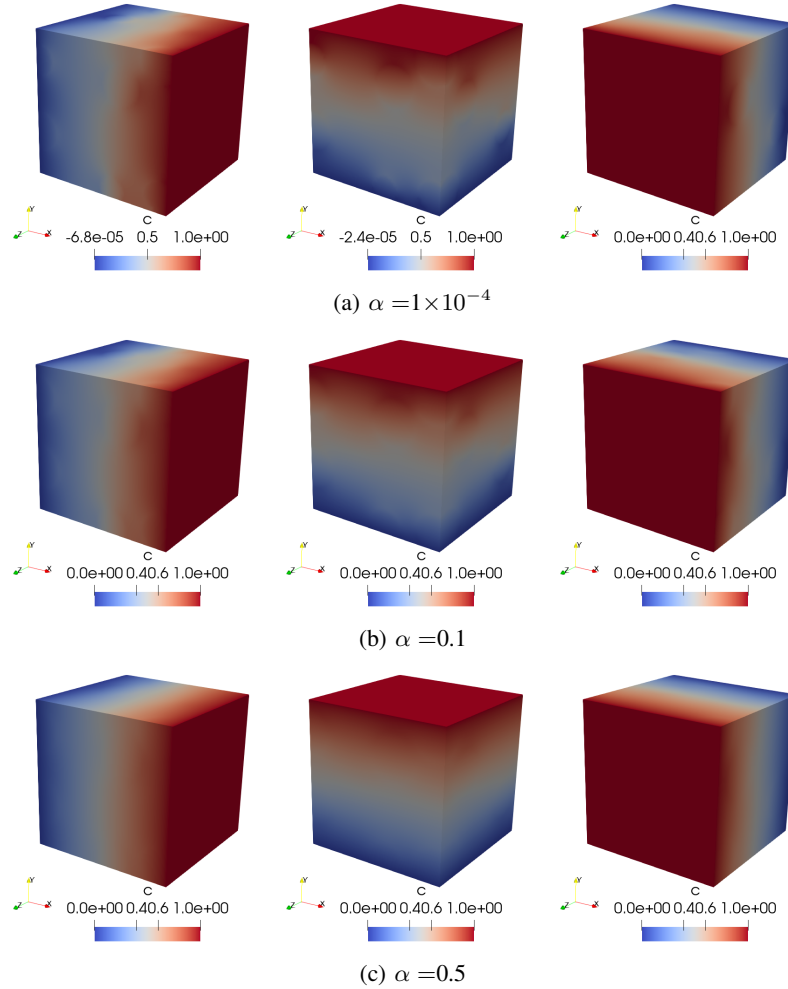


Fig. 48. Concentration profile contours, obtained via the unidirectional diffusion process, in the x-, y-, and z-directions at a fixed v_1 of 0.726 (see Figure 47 for the actual particle locations) for (a) $\alpha = 1 \times 10^{-4}$, (b) $\alpha = 0.1$, and (c) $\alpha = 0.5$. The FEA-predicted D_e was estimated from the average of three realizations performed in each principal direction.

smaller. As suggested in Toptan et al. (2021), the D-EMT accurately represents the expected behavior for $\alpha < 1$ in estimating EDC. The numerical simulations were performed under a packing fraction of up to approximately 40%. The maximum packing fraction for different arrangements (e.g., face-centered cubic (FCC), hexagonal close (HC), random close/loose, and simple cubic (SC)) are indicated in Figure 50a (Nielsen, 1974).

2) *Case II. The diffusivity coefficient of the particles is greater than the continuous matrix ($\alpha > 1$).*

Figure 49 shows the concentration profiles for the case with $\alpha > 1$. Similarly, the unidirectional diffusion process is illustrated in each principal direction at a fixed v_1 of 0.726 for the arbitrarily chosen $\alpha = 2.0$, 10.0, and 100.0. See Figure 47 for the actual particle locations at $v_1 = 0.726$.

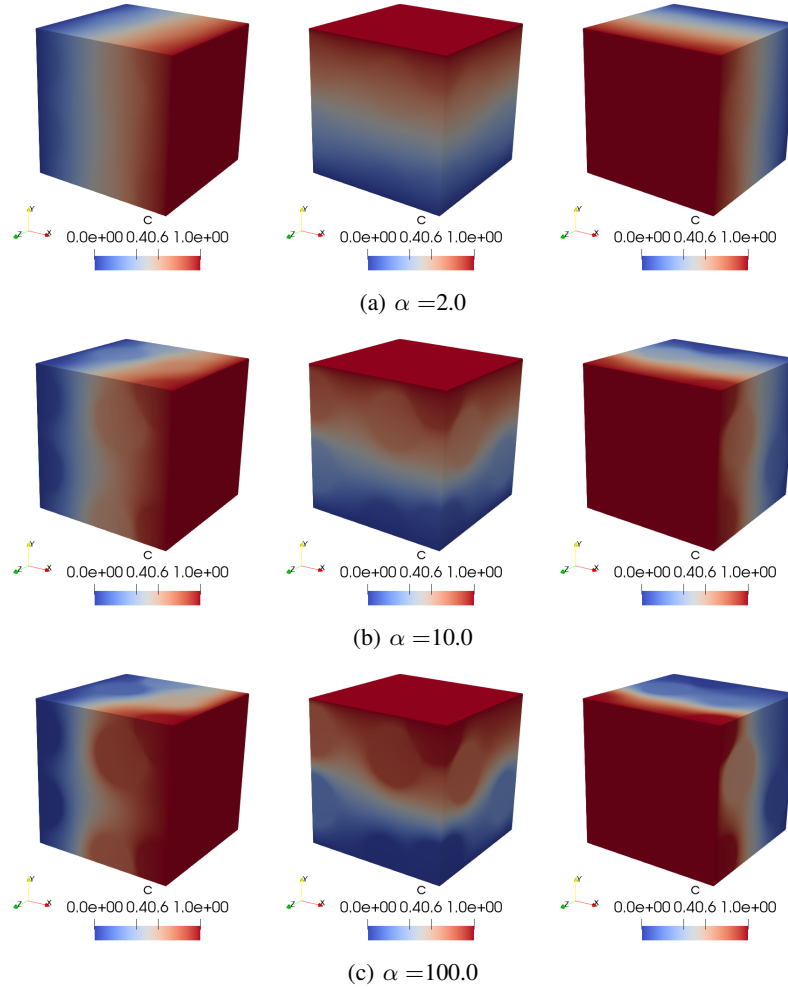


Fig. 49. Concentration profile contours, obtained via the unidirectional diffusion process, in the x-, y-, and z-direction at a fixed v_1 of 0.726 (see Figure 47 for the actual particle locations) for (a) $\alpha = 2.0$, (b) $\alpha = 10.0$, and (c) $\alpha = 100.0$. The FEA-predicted D_e was estimated from the average of three realizations performed in each principal direction.

The FEA and model predictions for D_e/D_1 are plotted in Figure 50b as a function of v_1 at the selected α values. The inclusion of more diffusive particles into the medium increases the system's overall diffusivity coefficient. The models only behave similarly at a packing fraction of up to 10% (i.e., $v_2 = 1 - v_1 = 0.10$), and significantly vary from each other when more particles are present in the system at higher α values. As suggested in Toptan et al. (2021) for the ETC, the EMT represents the expected behavior comparatively better for $\alpha > 1$ in estimating the EDC.

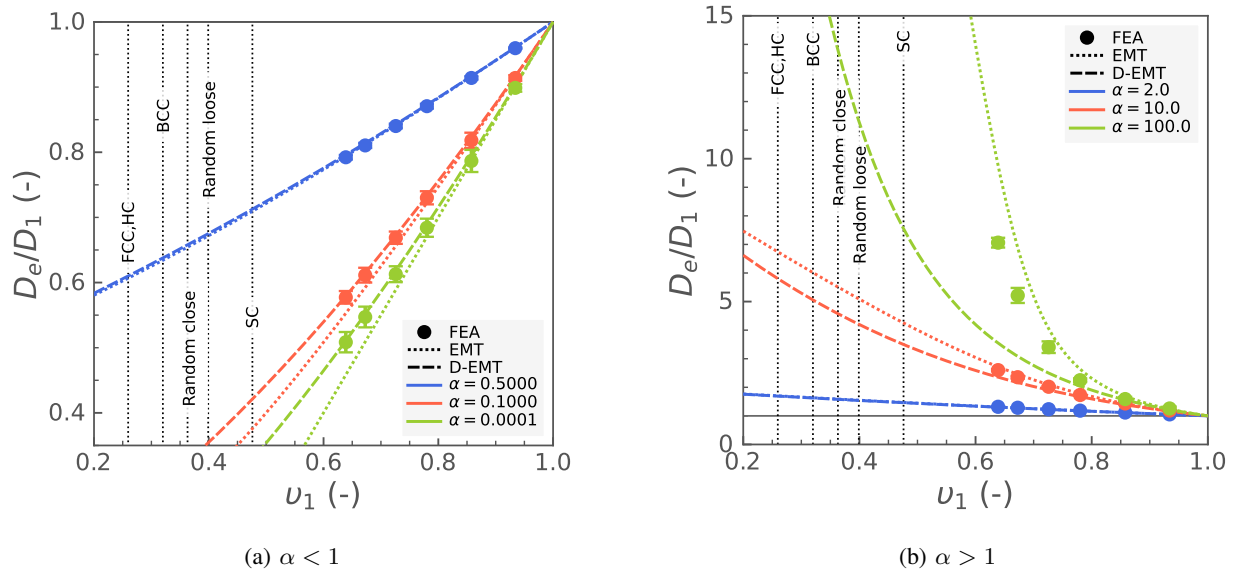


Fig. 50. D_e/D_1 predictions with respect to v_1 for (a) $\alpha < 1$ and (b) $\alpha > 1$. The model predictions and regions determined by the upper and lower bounds of the D_e/D_1 predictions are plotted against the expected FEA predictions. The packing fraction, v_2 , can be obtained from $1 - v_1$ in a binary system. The dashed vertical lines represent the maximum packing fractions for different arrangements (e.g., FCC, HC, random close/loose, and SC).

C. Summary

Analytical methods for application to the ETC of a medium with spherical inclusions were investigated in Toptan et al. (2021). Although the focus of that previous study was on the macroscopic description of thermal conductivity, the discussions and conclusions are similarly valid for diffusivity coefficients, due to their similar mathematical forms. In this study, we extended our research to examine the validity of models for the effective diffusivity calculations, obtained from the Fickian diffusion. Only the models we examined in our earlier study (Toptan et al., 2021) (i.e., D-EMT for $\alpha < 1$ and EMT for $\alpha < 1$) were considered in the present study. Each analytical model was evaluated with respect to the expected EDC obtained from the FEA simulations under a variety of conditions. In our analyses, the FEA simulations were performed under a packing fraction of up to approximately 40%. We observed similar behavior from each model in regard to estimating the EDC of a binary system: D-EMT for $\alpha < 1$ and EMT for $\alpha > 1$, where α is defined as the ratio of the diffusivity coefficient of spheres over that of the host matrix. These numerical results establish the regimes in which these analytical formulations can be used with a high degree of confidence for the applications of interest, particularly for Fickian-diffusion-based EDC estimation for TRISO modeling applications. Both the EMT and D-EMT approaches, among many others detailed in Toptan et al. (2021), are available in the BISON code.

VI. COMPACT DIFFUSION MODELING

A. Convergence Study on Point Source Calculation Using Dirac Kernels

In our approach to modeling the species diffusion of a TRISO compact/pebble, a homogenization technique is used to treat the compact/pebble as an equivalent continuous medium, and the species releases from TRISO particles are treated as point sources in the compact/pebble model. The point sources are modeled by setting the source term as the Dirac delta distribution $f(\mathbf{x}) = \delta(\mathbf{x})$. The Dirac delta distribution satisfies $\int \psi(\mathbf{x})\delta(\mathbf{x} - \hat{\mathbf{x}})d\mathbf{x} = \psi(\hat{\mathbf{x}})$ at $\hat{\mathbf{x}} \in \Omega$ for any continuous function $\psi(\mathbf{x})$. The accuracy of the numerical solution is verified by computing the convergence order of the FEM for elliptic test problems, as given below:

$$-\Delta u = f \quad \text{in } \Omega, \quad (32)$$

$$u = r \quad \text{on } \partial\Omega, \quad (33)$$

where $f(\mathbf{x})$ and $r(\mathbf{x})$ are given functions on the domain Ω and on its boundary $\partial\Omega$, respectively. Smooth and non-smooth test problems from Kalayeh et al. are considered. For the smooth problems, the RHS of the Poisson equation $f(\mathbf{x})$ in Equation 32 was chosen to be:

$$f(\mathbf{x}) = \begin{cases} \frac{\pi}{2} \left(\frac{1}{\rho} \sin \frac{\pi\rho}{2} + \frac{\pi}{2} \cos \frac{\pi\rho}{2} \right) & \text{for 2-D,} \\ \frac{\pi}{2} \left(\frac{2}{\rho} \sin \frac{\pi\rho}{2} + \frac{\pi}{2} \cos \frac{\pi\rho}{2} \right) & \text{for 3-D,} \end{cases} \quad (34)$$

where the norm $\rho = \sqrt{x^2 + y^2}$ in 2-D and $\rho = \sqrt{x^2 + y^2 + z^2}$ in 3-D. The analytical solutions are given as:

$$u(\mathbf{x}) = \begin{cases} \cos \frac{\pi\sqrt{x^2+y^2}}{2} & \text{for 2-D,} \\ \cos \frac{\pi\sqrt{x^2+y^2+z^2}}{2} & \text{for 3-D.} \end{cases} \quad (35)$$

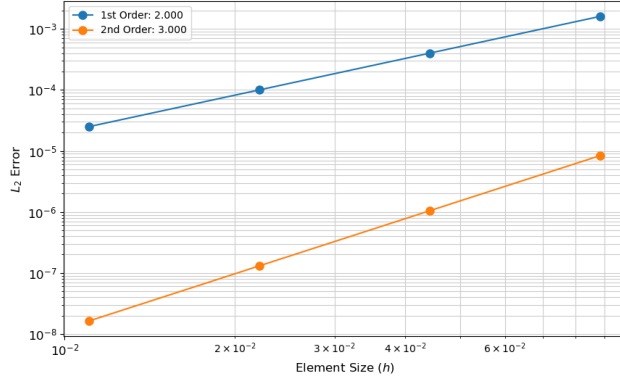
For a smooth problem, mathematical theory shows that the convergence rate of the L^2 norm can reach $p + 1$, where p is the polynomial degree. Our numerical solutions shown in Figure 51 agree with the mathematical derivation.

For the non-smooth test problems, the forcing term $f(\mathbf{x})$ is chosen to model a point source. In the Multiphysics Object-Oriented Simulation Environment (MOOSE), a point source is applied by `DiracKernel`. The analytical solutions are given as:

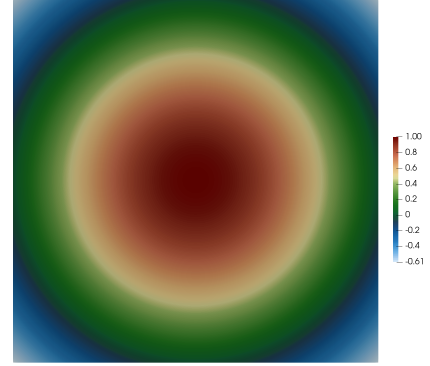
$$u(\mathbf{x}) = \begin{cases} \frac{-\ln \sqrt{x^2+y^2}}{2\pi} & \text{for 2-D,} \\ \frac{1}{4\pi\sqrt{x^2+y^2+z^2}} & \text{for 3-D.} \end{cases} \quad (36)$$

The solution of a non-smooth problem is not square-integrable, so the convergence rate is limited by the regularity order k given by $2 - d/2$, which depends on the dimensions d . Our numerical solutions shown in Figure 52 agree with the mathematical derivation by which degraded convergence rates are predicted.

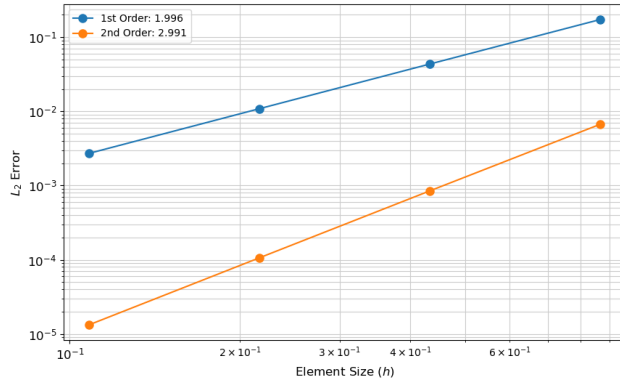
To mitigate degradation, one approach is to use a graded mesh that is locally refined around the point. Though this approach can almost recover the optimal convergence rate, as shown in Figure 53, it becomes infeasible for a multiple point sources problem because generating a graded mesh for multiple points can



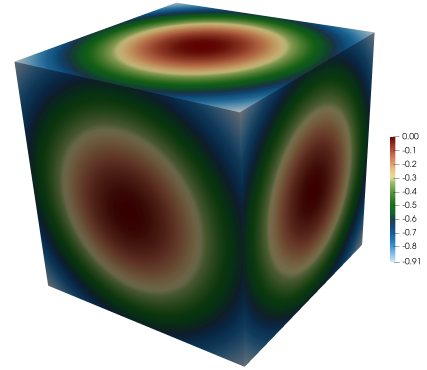
(a) Convergence rates for the 2-D smooth test problem with first- and second-order finite elements.



(b) Solution of the 2-D smooth test problem.



(c) Convergence rates for the 3-D smooth test problem with first- and second-order finite elements.



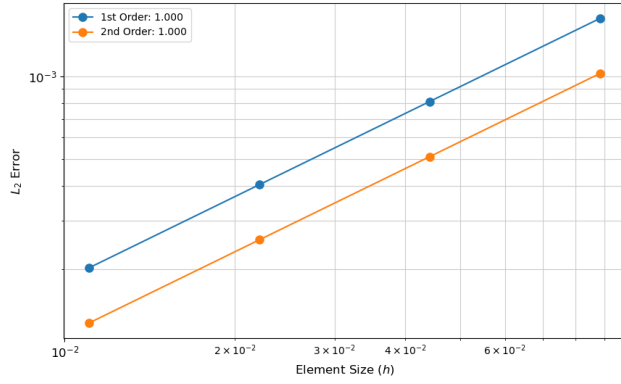
(d) Solution of the 3-D smooth test problem.

Fig. 51. Convergence studies for the smooth test problems.

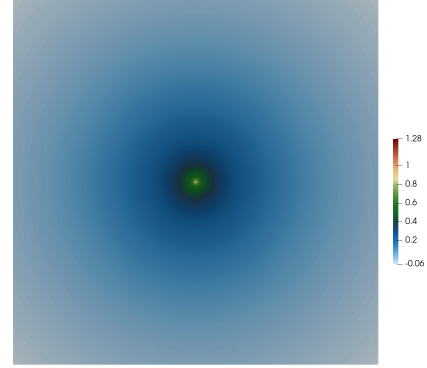
be practically difficult. Another way to recover optimality is to evaluate errors only in the domain away from the singular points. Figure 54 shows that the solution away from the point can reach an optimal convergence rate. This indicates that the use of point sources in TRISO compact/pebble modeling can provide good accuracy if the global species diffusion quantities are of interest.

B. Two-Way Coupling between TRISO Particles and the Matrix

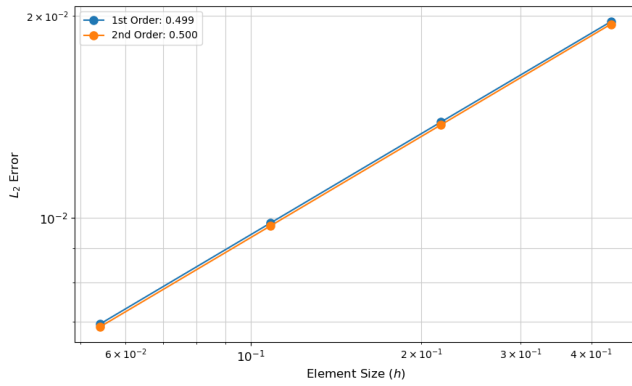
The coupling between TRISO particles and the matrix utilizes MOOSE's "MultiApps" system (Jiang et al. (2021c)). The species releases from TRISO particles are treated as point sources in the compact/pebble model. The point sources can be directly obtained from the MC simulation, and their values are transferred to the compact/pebble model at every time step. Previously, all TRISO particles were set at the same temperature boundary conditions regardless of their location inside the compact/pebble.



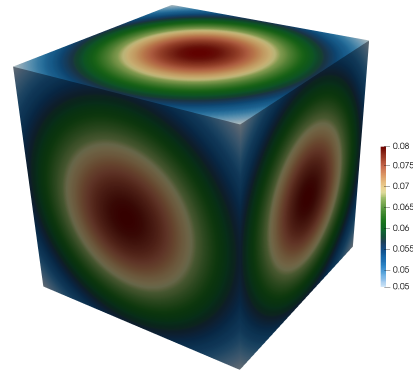
(a) Convergence rates for the 2-D non-smooth test problem with first- and second-order finite elements.



(b) Solution of the 2-D non-smooth test problem.



(c) Convergence rates for the 3-D non-smooth test problem with first- and second-order finite elements.

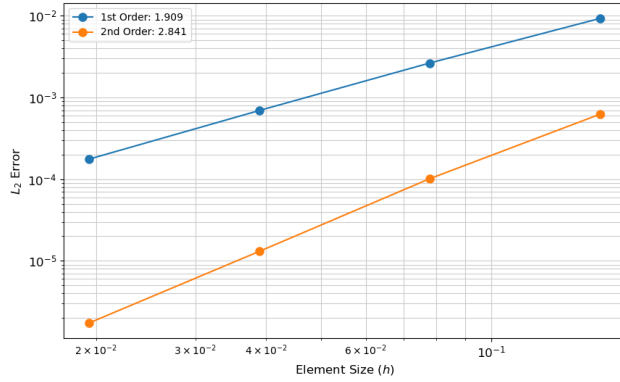


(d) Solution of the 3-D non-smooth test problem.

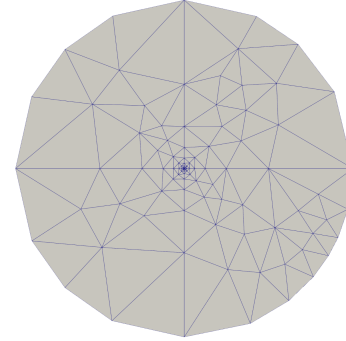
Fig. 52. Convergence studies for the non-smooth test problems.

To account for the effect of temperature variations across the compact/pebble, a new capability was developed to transfer temperature from the compact/pebble to TRISO particles, based on their locations. This overall capability is depicted in Figure 55. An example of the two-way coupling between TRISO particles and the compact is shown in Figure 56. The cross-section temperature contours show that the compact temperature field correctly transfers to all particles. The temperatures and SiC stress histories of all the particles are shown in Figure 57. The maximum differences in temperature and SiC stress for all particles in a compact are about 20 K and 250 MPa, respectively.

Our two-way coupling capability was further extended to model multiple compacts. Figure 58 shows an example of modeling three compacts with particle point sources. The particles in each compact can feature unique statistical variations in terms of layer thickness and material properties. Each compact can also have its own packing fraction and particle distribution. This can be useful in studying axial species



(a) Convergence rates for the 2-D non-smooth test problem using a graded mesh.



(b) Graded mesh.

Fig. 53. Convergence studies for the non-smooth test problems using a graded mesh.

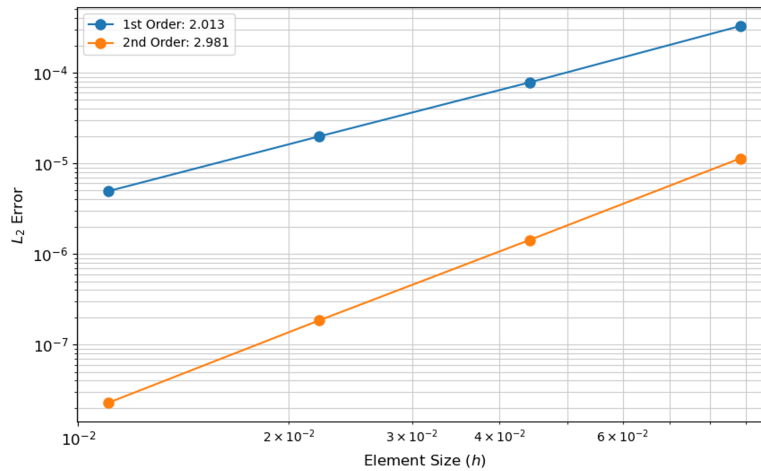


Fig. 54. Convergence rates for the 2-D non-smooth test problem for the domain away from the point.

diffusion in capsules used in AGR experiments.

Recent assessment of TRISO particle locations confirmed and further quantified a non-uniform distribution of TRISO particles, with the spatial distribution in the radial direction being roughly described as a dampened sinusoidal function (Kane et al., 2022). A new capability for reading particle locations from a text file was developed. The text file stores particle x, y, and z-coordinates taken from x-ray computed tomography measurements. Three representative AGR-1 compacts with packing fractions of 25, 40, and 48% are demonstrated in Figure 59. The center-line temperature rises as the packing fraction increases. A cross-section view of the particles reveals a ring pattern distribution in the radial direction. The effect

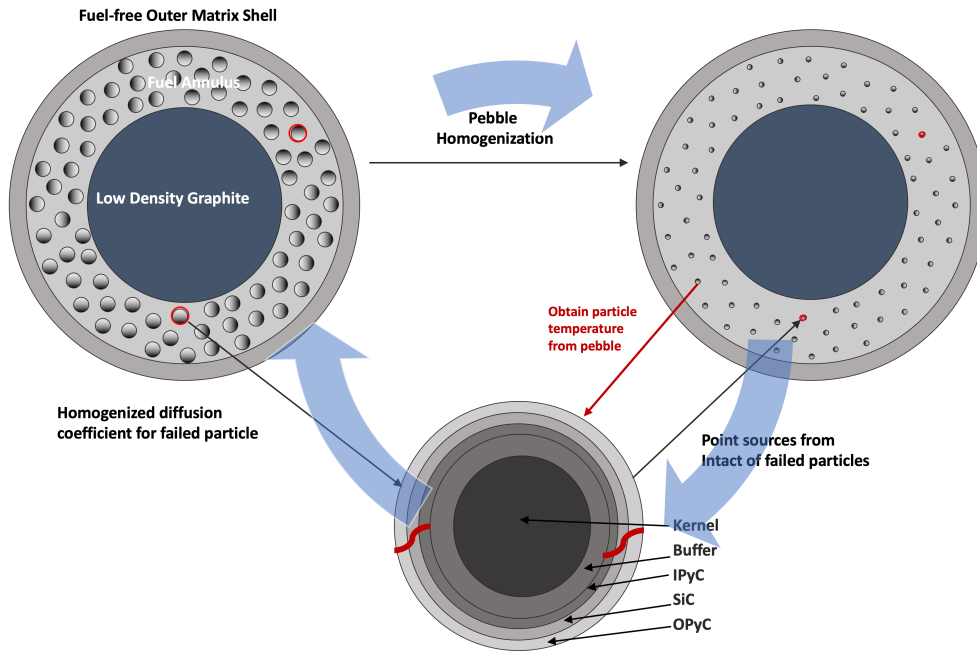


Fig. 55. BISON pebble modeling illustration.

of the particle distribution pattern on compact and particle behaviors will be the subject of future study.

To evaluate the accuracy of release fraction calculations made using our “multi-app” approach, a benchmark problem involving a single particle was considered. As shown in Figure 60, this benchmark problem was solved using both the multi-app and monolithic approaches. In the monolithic approach, the particle and matrix are simulated simultaneously within a single domain. In the multi-app approach, the release from the particle is transferred to the matrix as a point source. The amount of release from the matrix with different diffusivity was shown in Figure 61. As particle diffusivity increases, the difference between the multi-app and monolithic approaches shrinks.

C. TRISO Diffusion Modeling with Discontinuous Galerkin

Fission product diffusivity exhibits large contrasts across the various layers of a TRISO particle. This results in the Gibbs phenomenon (i.e., solution oscillation near the interface) when using the classical continuous Galerkin (CG) method. This solution oscillation can be mitigated by a locally refined mesh near the interface, but this can significantly increase the computational cost for 2-D and 3-D problems. The Gibbs phenomenon is attributed to the use of continuous functions to approximate an abrupt jump. Thus, the solution oscillation associated with the Gibbs phenomenon can be largely ameliorated by using a discontinuous Galerkin (DG) method.

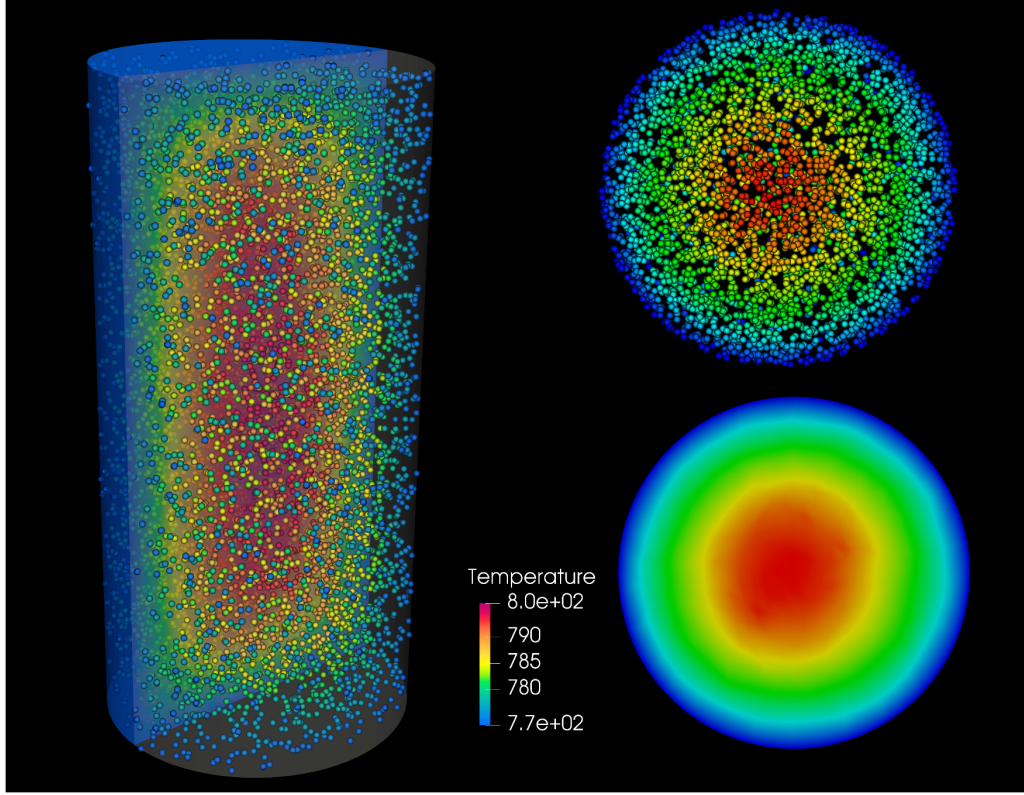


Fig. 56. BISON compact modeling with two-way coupling.

In DG, additional constraints to enforce local mass conservation are needed across the element edges. The residual of those constraints is implemented as `DGKernel` in MOOSE. For diffusion problems, the weak form of element edge terms is given as:

$$R = - \sum_e \int_e \{k \nabla u\} \llbracket \psi \rrbracket dS - \sum_e \int_e \{k \nabla \psi\} \llbracket u \rrbracket dS + \sum_e \int_e \frac{\beta}{h_e} k_e \llbracket \psi \rrbracket \llbracket u \rrbracket dS. \quad (37)$$

The weighted average operator is defined as:

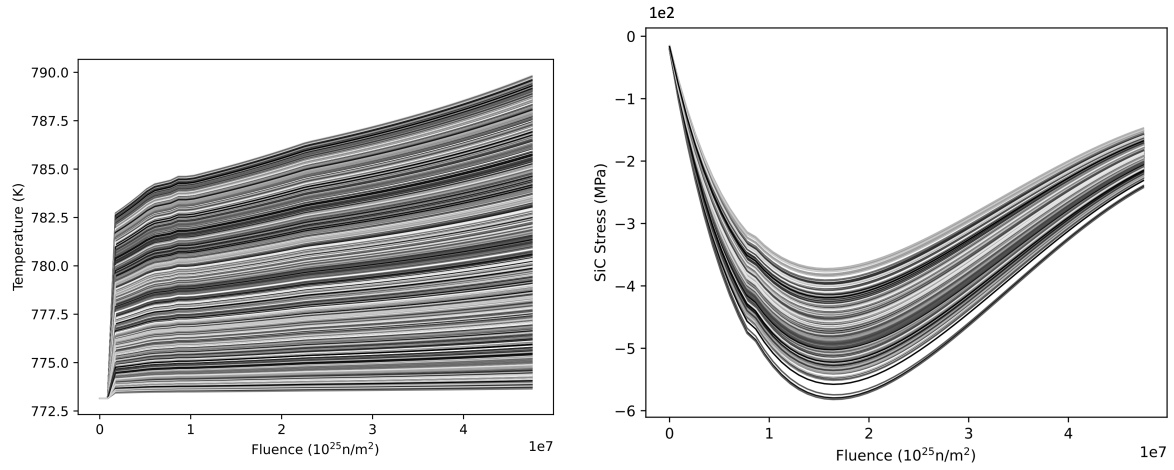
$$\{X\}_{\delta_e} = \delta_e X^+ + (1 - \delta_e) X^-, \quad (38)$$

where δ_e is calculated as:

$$\delta_e = \frac{k_e^-}{k_e^+ + k_e^-}. \quad (39)$$

The harmonic average of diffusion coefficient, k_e , is given as:

$$k_e = \frac{2k_e^+ k_e^-}{k_e^+ + k_e^-}. \quad (40)$$



(a) Temperature history of all particles.

(b) SiC stress history of particles.

Fig. 57. Particle temperature and SiC stress history.

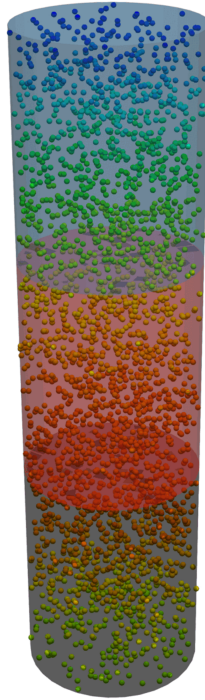


Fig. 58. Three compact modeling.

The interior penalty parameter, β , is a function of polynomial degree approximation, k . h_e is a

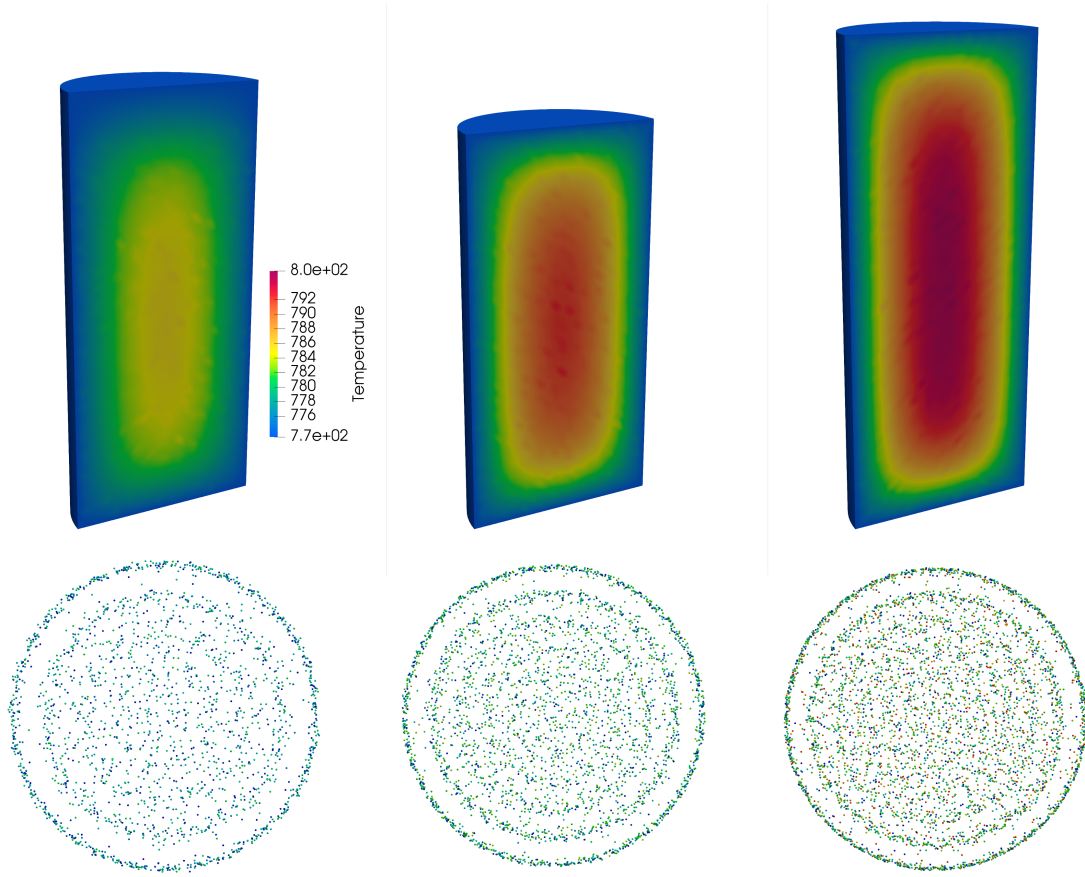


Fig. 59. Compacts with packing fractions of 25, 40, and 48%. The particle locations are directly read from x-ray computed tomography measurement.

characteristic element length, calculated as:

$$h_e = \frac{\text{meas}(T^+) + \text{meas}(T^-)}{2\text{meas}(e)}, \quad (41)$$

where $\text{meas}(\cdot)$ represents a measurement operator for measuring length and area.

The DG was implemented in BISON and then used to simulate fission product diffusion in a 2-D axisymmetric TRISO particle. The fuel properties and irradiation conditions of compact 5-3-1 from AGR-1 were considered (Jiang et al. (2021a)). The cesium diffusion was simulated. As shown in Figure 62, in the presence of a high diffusivity contrast, CG produces large oscillations at the kernel/buffer interface, while DG successfully captures the abrupt concentration jump, without any oscillation. The spikes resulting from CG can eventually be smoothed out by numerical diffusion, but they pose an accuracy issue in the early stages and might generate inaccurate results for accumulated quantities (e.g., release fraction).

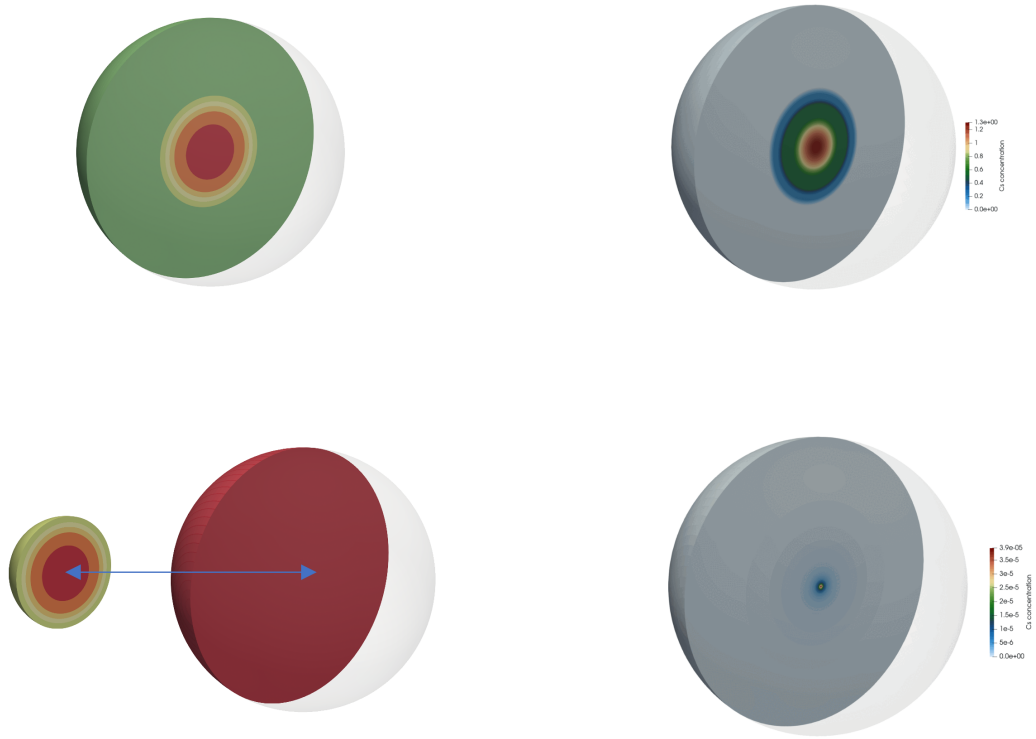


Fig. 60. Particle species diffusion through the matrix. Top row: monolithic approach; bottom row: multi-app approach.

D. Sorption Isotherm Implementation for AGR 3/4 Rings

The BISON compact modeling capability was first applied to the modeling of AGR 3/4 experiments. Each AGR 3/4 compact contains driver fuel particles and 20 designed-to-failed (DTF) particles placed along its axis. The fuel compacts are surrounded by three concentric annular rings of a test material consisting of fuel-compact matrix material and fuel-element graphite. Figure 63 shows a BISON 3-D model, with the DTF particles placed in the center line, and randomly distributed driver particles hosted in the fuel compact. The four regions of the BISON model are the fuel compact, matrix, graphite, and sink. They are separated blocks that do not share nodes between their interfaces. Their height is 12.5 mm, with a compact radius of 6.15 mm and ring wall thicknesses of 6.05, 6.30, and 13.14 mm, respectively.

The temperature boundary conditions at the outer fuel compact surface, inner/outer matrix surface, inner/outer graphite surface, and inner/outer sink surface were obtained from prior numerical analysis. The presence of gaps results in discontinuities in the fission product concentration across rings. Established sorption isotherms are used to determine the surface concentration between the two surfaces (subscripts 1 and 2) via:

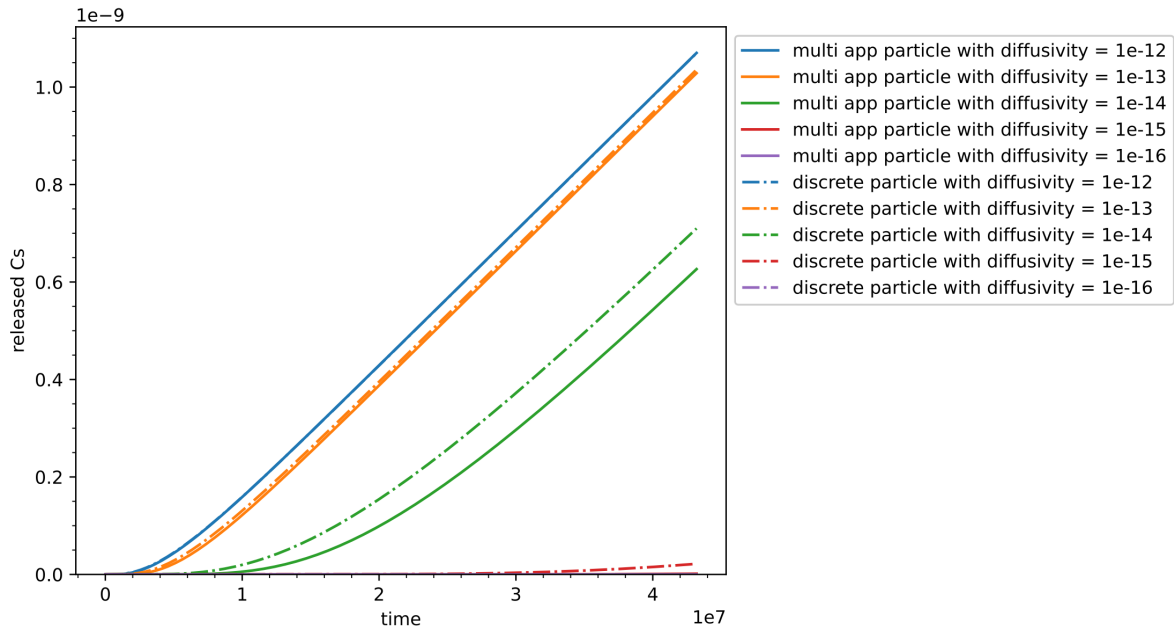


Fig. 61. Species release from the matrix with different particle diffusivities.

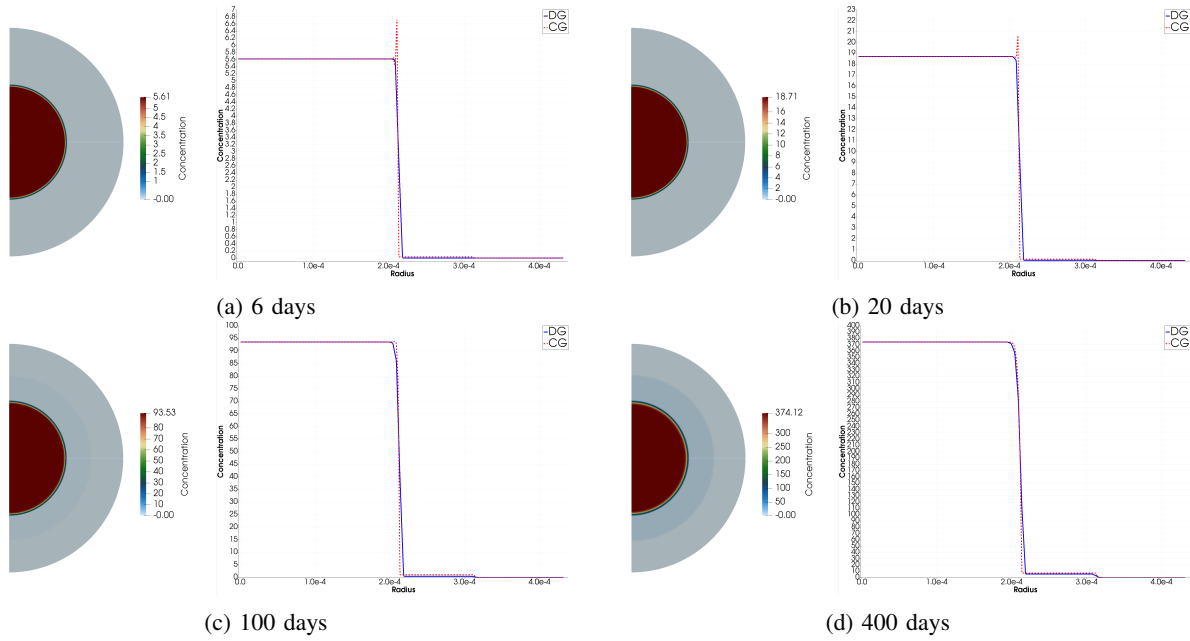


Fig. 62. Cesium concentration along the radial direction at time = 6, 20, 100, and 400 days.

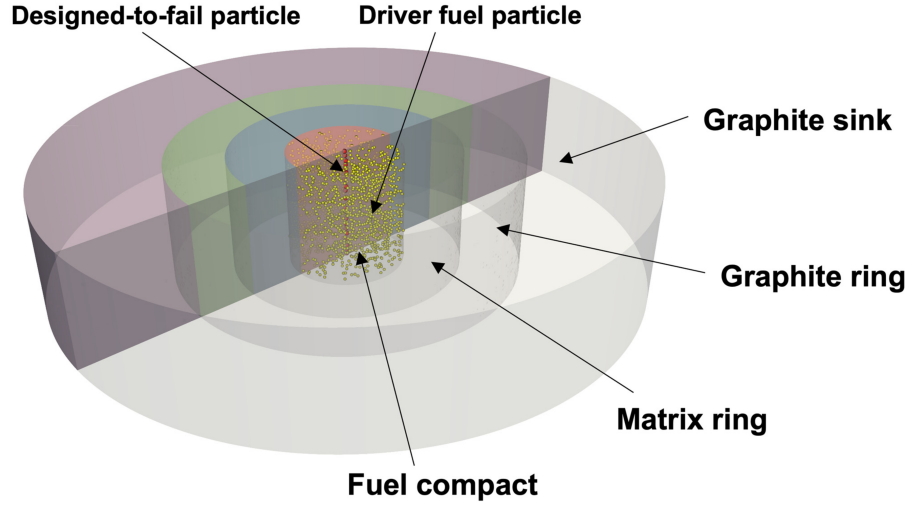


Fig. 63. AGR 3/4 BISON representation. The four regions of the BISON model are the fuel compact, matrix ring, graphite ring, and graphite sink.

$$\begin{aligned} & \exp\left(A_1 + \frac{B_1}{T_1}\right) C_1^{(D_1 + \frac{E_1}{T_1})} + \exp\left[\left(A_1 + \frac{B_1}{T_1}\right) + \left(D_1 - 1 + \frac{E_1}{T_1}\right)(d_{11} - d_{21}T_1)\right] C_1 \\ & = \exp\left(A_2 + \frac{B_2}{T_2}\right) C_2^{(D_2 + \frac{E_2}{T_2})} + \exp\left[\left(A_2 + \frac{B_2}{T_2}\right) + \left(D_2 - 1 + \frac{E_2}{T_2}\right)(d_{12} - d_{22}T_2)\right] C_2 \end{aligned} \quad (42)$$

The values A , B , D , E , d_1 , and d_2 are sorption isotherm constants, and their values for cesium and strontium are provided in Skerjanc and Jiang (2022).

The interfacial conditions are completed by enforcing mass flux balance across the gap:

$$D_{01} \exp\left(-\frac{Q_1}{RT_1}\right) \nabla C_1 \cdot \mathbf{n}_1 = D_{02} \exp\left(-\frac{Q_2}{RT_2}\right) \nabla C_2 \cdot \mathbf{n}_2. \quad (43)$$

Equation 42 and Equation 43 were implemented in BISON by using a penalty method as an `InterfaceKernel`. To verify its implementation, BISON's simulation results were compared against the previous COMSOL simulation results for the AGR 3/4 experiment. The cesium concentration profile is shown in Figure 64. The concentration variation across the “gaps” seems to match very well when comparing BISON and COMSOL, thus verifying the BISON implementation of the interfacial isotherm sorption conditions. The minor discrepancy seems to be attributable to the different diffusion coefficients used by the two codes.

The 1-D BISON model was used to calculate the fission product concentration profiles across selected capsules' rings under daily as-run irradiation conditions, and compare them to measured PIE data. The detailed results are found in Skerjanc and Jiang (2021, 2022).

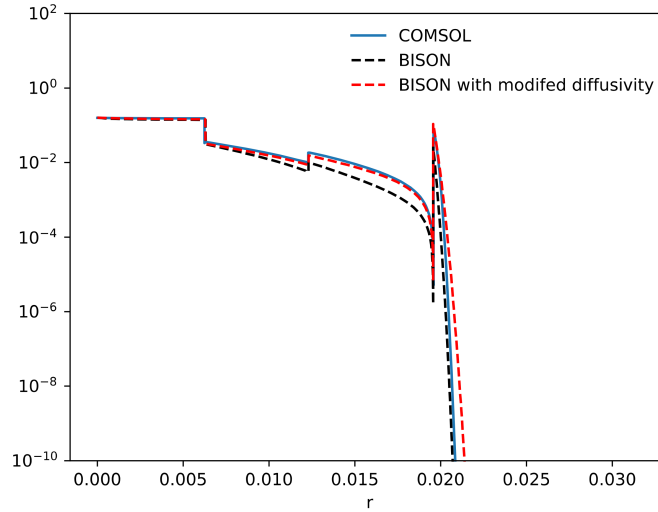


Fig. 64. Radial (r in m) cesium concentration profile of the COMSOL benchmark, as compared to BISON.

E. AGR-1 Fission Product Release Calculation with Compact Modeling

Finally, we reran AGR-1 cases to calculate fission product release by considering the compact diffusion. There are two major differences between the new calculation and the old one. First, we consider a batch of particles in a compact along with their statistical variations in fuel properties and dimensions. Second, the diffusion inside the compact is simulated, and potential retention of fission products by a compact can be evaluated. Compared to the old BISON prediction method (Hales et al., 2021), the new prediction method based on compact modeling does not significantly affect the release fraction of silver and cesium, due to their high diffusivity in the graphite matrix. However, the BISON compact simulation predicts some amount of strontium retention in the graphite matrix as a result of its relatively low diffusivity. This is more consistent with PARFUME's results in considering graphite matrix diffusion.

F. Summary

BISON's compact modeling capability was significantly improved to enable two-way coupling between TRISO particles and the matrix. Our approach treats particles as point sources that are obtained from a MC particle simulation using MOOSE's multi-app capability. The convergence study on solving point sources with MOOSE's `DiracKernel` was carefully performed. The compact modeling was applied to the AGR-1 and 3/4 experiments, and the resulting predictions were compared against the PIE measurements.

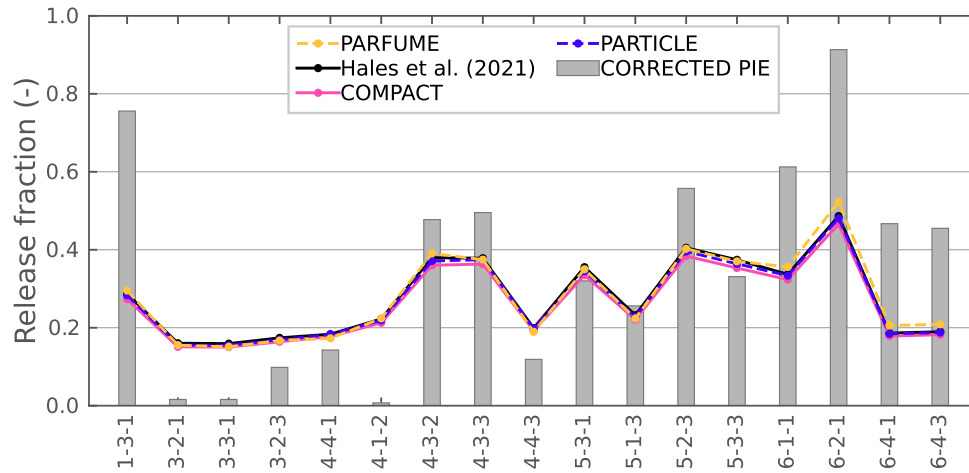


Fig. 65. Silver release of AGR-1 compacts.

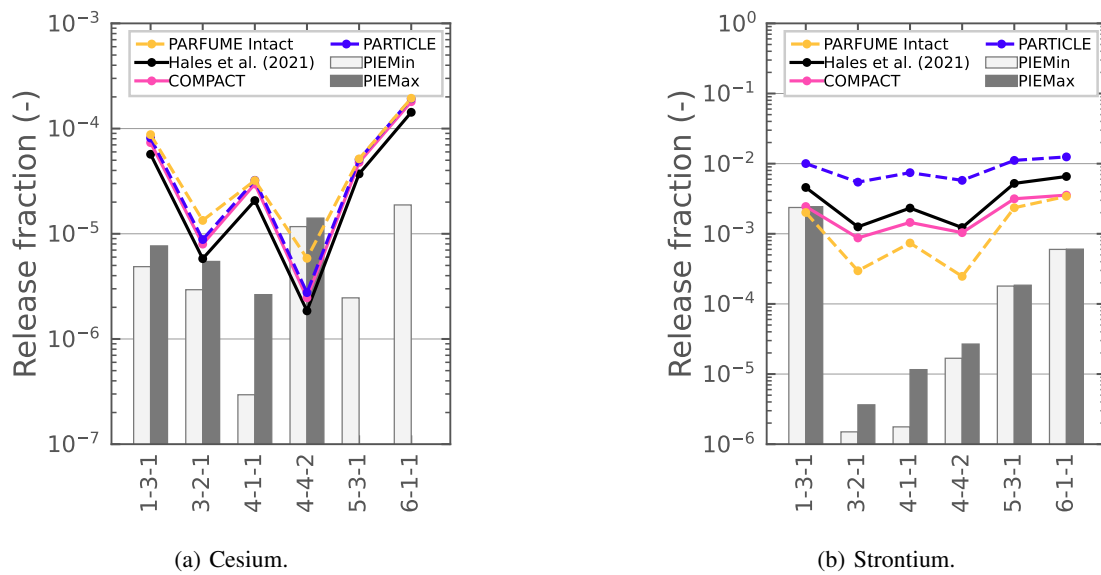


Fig. 66. Cesium and strontium release of AGR-1 intact compacts.

VII. ACCELERATED STATISTICAL FAILURE ANALYSIS OF MULTI-FIDELITY TRISO MODELS

A. Preliminaries

Statistical failure analysis and information on the geometrical and material properties that cause failure is important for TRISO fuel fabrication and design. The standard method of computing the TRISO failure probability is the MC method, discussed in Jiang et al. (2021a). In MC, the failure probability, (\hat{P}_f), is estimated via:

$$\hat{P}_f = \frac{1}{N} \sum_{i=1}^N \mathcal{I}_i, \quad (44)$$

where N is the number of samples or model evaluations and \mathcal{I} is an indicator function for model failure. The coefficient of variation (COV) estimate ($\hat{\delta}$), which quantifies the accuracy of the failure probability estimate, is given by:

$$\hat{\delta} = \sqrt{\frac{1 - \hat{P}_f}{\hat{P}_f N}}. \quad (45)$$

The lower the COV, the more accurate the failure probability estimate. For practical purposes, a COV value of 0.05–0.1 is desirable. However, given that TRISO failure probabilities are small, ranging from 1×10^{-3} to 1×10^{-6} , achieving a COV of 0.05–0.1 can require tens of millions of TRISO model evaluations. This is computationally prohibitive in practice, especially when using 2-D models. Therefore, this section summarizes recent developments in BISON/MOOSE for conducting accelerated failure analysis of TRISO fuel in terms of both 1-D and 2-D models. The accelerated methods summarized herein are divided into two classes: variance reduction methods and Weibull theory approach. Variance reduction methods are a class of MC methods that use intelligent sampling schemes to sample the model failure region, and usually result in ~ 2 orders of magnitude in computational efficiency compared to the standard MC. The Weibull theory approach assumes that the TRISO model predominantly fails through the Weibull failure mode, and it thus computes the failure probability directly, given a set of uncertain TRISO geometrical and material parameters. However, if more advanced failure modes of TRISO fuel are considered, which may not follow the Weibull failure mode, the Weibull theory approach cannot be used in an exact sense—unlike the MC and MC variance reduction methods. The presentation herein of the methods, implementations in BISON/MOOSE, and results can basically be considered a summary of the following papers: Dhulipala et al. (2022a,b)^a.

B. Methods for Accelerated Failure Analysis

1) Variance Reduction Method: Adaptive Importance Sampling

Adaptive Importance Sampling (AIS) has two phases: (1) a learning phase in which the AIS algorithm learns the importance distribution of input parameters likely to cause model failure; and (2) a sampling phase to sample from the learned importance distribution. The version of AIS proposed by Au and Beck (1999) is implemented in BISON through MOOSE, with a slight modification. Instead of using kernel density to characterize the importance distribution, a normal density is used, due to its simplicity and robustness. Figure 67 presents a schematic of the AIS method.

^aThe methodology for accelerated failure estimation described herein was funded by the INL Laboratory Directed Research & Development program, project number 21A1050-114FP.

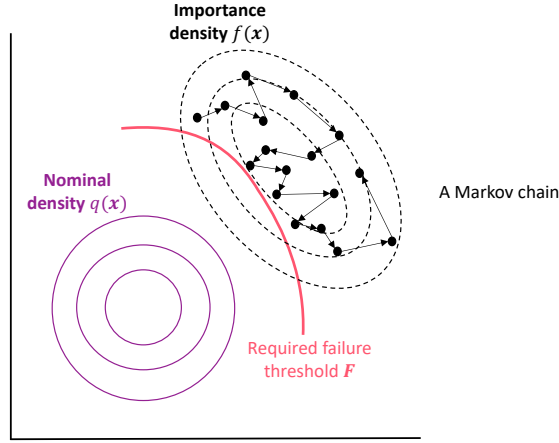


Fig. 67. Schematic of the AIS method for accelerated failure probability estimation.

For learning the importance distribution of the input parameters, a Markov Chain Monte Carlo (MCMC) algorithm known as the Metropolis algorithm (Au and Beck, 1999) is used. The user supplies an `initial_values` vector of input parameters that would result in model failure. Next, a Markov chain is initiated to sufficiently sample from the failure region. The Markov chain operates in standard normal space, where all the input parameters are transformed to have a normal distribution with a mean of 0 and a standard deviation of 1. Centered around the current sample (\mathbf{x}), a new sample (\mathbf{x}^*) is proposed considering the proposal distribution to be normal, and an acceptance ratio is computed:

$$\alpha = \frac{\mathcal{N}(\mathbf{x}^*)}{\mathcal{N}(\mathbf{x})}, \quad (46)$$

where $\mathcal{N}(\cdot)$ is a standard normal distribution. The proposed sample is then accepted with probability α . In this manner, sufficient samples are generated from the failure region.

Once enough samples that result in model failure have been simulated, an importance distribution is fit to these samples. A normal distribution is fit to each input parameter independently, and sampling from this importance distribution is conducted. Use of an independent normal distribution differs from the work by Au and Beck (1999), who use a multi-dimensional kernel density distribution. However, experience suggests that a normal distribution is more robust under a wide variety of cases. Once the samples from the importance distribution are obtained, the failure probability can be estimated using:

$$\hat{P}_f = \frac{1}{N} \sum_{i=1}^N \mathcal{I} \frac{q(\mathbf{x})}{f(\mathbf{x})}, \quad (47)$$

where N is the number of samples during the evaluation phase, \mathcal{I} is an indicator function for model failure, $q(\cdot)$ is the nominal density, and $f(\cdot)$ is the importance density. The variance over \hat{P}_f is estimated using:

$$\text{Var}(\hat{P}_f) = \frac{1}{N} \left\{ \frac{1}{N} \sum_{i=1}^N \left[\mathcal{I} \frac{q(\mathbf{x})}{f(\mathbf{x})} \right]^2 - (\hat{P}_f)^2 \right\}. \quad (48)$$

The COV is estimated via:

$$\hat{\delta} = \frac{\sqrt{\text{Var}(\hat{P}_f)}}{\hat{P}_f}. \quad (49)$$

2) Variance Reduction Method: Parallel Subset Simulation

parallel subset simulation (PSS) is used for efficiently estimating small failure probabilities when dealing with computationally expensive numerical models. In BISON, we implemented the PSS proposed by Au and Beck (2001). PSS works by creating intermediate failure thresholds to efficiently transition from sampling from the nominal input space to sampling from input spaces that result in model failure. Use of MCMC is key to the PSS algorithm. In fact, PSS uses hundreds of Markov chains to efficiently propagate to the regions of the input space that are most important with respect to model failures. Since these Markov chains are independent of each other, they can be run in parallel on a different set of processors.

To efficiently sample from regions of input parameter spaces that are crucial for failure evaluation of the model, PSS creates intermediate failure thresholds defined via the following equation:

$$P_f = P_1 \prod_{i=2}^{N_s} P_{i|i-1}, \quad (50)$$

where P_f is the failure probability of interest, P_1 and $P_{i|i-1}$ ($i \in \{2, \dots, N_s\}$) are the intermediate failure probabilities defining the intermediate failure thresholds, and N_s is the number of subsets. Through the intermediate failure probabilities P_1 and $P_{i|i-1}$, PSS creates intermediate failure thresholds that enable an efficient transition to sampling from input spaces that cause numerical model failure or numerical model optimal output. These intermediate failure thresholds are created with the aid of numerous Markov chains. Figure 68 presents a schematic of the PSS method.

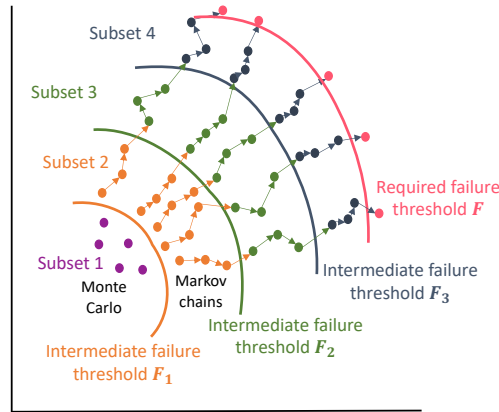


Fig. 68. Schematic of the PSS method for accelerated failure probability estimation.

In practice, PSS is implemented in the following manner. If N is the total number of numerical model evaluations, each subset will have $M = N/N_s$ samples. A MC is first used to generate M samples. If the intermediate failure probabilities (except $P_{N_s|N_s-1}$) are all fixed to 0.1, then the first intermediate

failure threshold F_1 is estimated as the 90th percentile value of all the M numerical model outputs. The outputs that do not exceed \mathcal{F}_1 constitute Subset 1. To determine the next failure threshold \mathcal{F}_2 , conditional samples should be generated such that the numerical model outputs always exceed \mathcal{F}_1 . An MCMC method—particularly a component-wise Metropolis method—is used to estimate \mathcal{F}_2 by simulating numerous Markov chains. From the M MC samples in the first subset, those that exceeded the threshold \mathcal{F}_1 are used as seeds (or starting values) for these Markov chains. If M samples need to be simulated such that the outputs exceed \mathcal{F}_1 , there will be $0.1 M$ Markov chains, with each chain simulating $1/0.1$ samples. In general, if the intermediate failure probabilities (except $P_{N_s|N_{s-1}}$) are fixed to p_o instead of 0.1, there will be $p_o M$ Markov chains, with each chain simulating $1/p_o$ samples. Once M samples are generated from $p_o M$ Markov chains, the second intermediate failure threshold F_2 is the $(1 - p_o) \times 100$ percentile value of all the samples' outputs. Samples between F_1 and F_2 comprise the second subset. A similar procedure of simulating $(p_o M)$ Markov chains is repeated for determining the subsequent failure thresholds until the final required failure threshold F is reached. An approximate COV estimate to the intermediate failure probability in subset i is given by Au and Beck (2001):

$$\hat{\delta}_i = \begin{cases} \sqrt{\frac{1 - \hat{P}_1}{\hat{P}_1 M}}, & \forall i = 1 \\ \sqrt{\frac{1 - \hat{P}_{i|i-1}}{\hat{P}_{i|i-1} M}}, & \forall 1 < i \leq N_s \end{cases} \quad (51)$$

The overall COV estimate over the required failure probability (\hat{P}_f) is:

$$\hat{\delta} = \sqrt{\sum_{i=1}^{N_s} \hat{\delta}_i^2}. \quad (52)$$

Since the PSS method consists of numerous Markov chains in each subset, the TRISO evaluations for separate Markov chains can be conducted in parallel using multiple processors. It is important to note that parallelization is only feasible across Markov chains, and not within a given chain. A single processor should be used to completely evaluate an entire Markov chain consisting of $\text{int}(1/p_o)$ samples. Also, subset $i + 1$ cannot begin before simulating subset i , which means that a single processor should at least evaluate $\text{int}(1/p_o) N_s$ samples. If there are P processors and $\text{int}(p_o M) N_s$ samples across all the subsets, each processor evaluates the following number of samples:

$$N_P^{\text{PSS}} = \max \left\{ \frac{\text{int}(p_o M) N_s}{P}, \text{int}(1/p_o) N_s \right\} \quad (53)$$

3) Weibull Approach

IPyC cracking and SiC failure due to IPyC cracking are the dominant failure modes for TRISO fuel. If only these failure modes are of interest, it is possible to directly estimate the failure probability, since these modes are governed by the Weibull criterion. That is, for a given set of random input parameters and the computed stresses in the IPyC or SiC layers, we can estimate the Weibull failure probability by using the cumulative distribution function of a Weibull distribution:

$$W_i(\mathbf{x}) \sim 1 - \exp \left(- \frac{\sigma_c(\mathbf{x})^m}{(\sigma_{ms})^m} \right), \quad (54)$$

Listing 1. Main input file block for transferring the QoI from the sub file to the main file.

```
[Transfers]
[reporter_transfer]
  type = SamplerReporterTransfer
  # IPyC failure:
  from_reporter = 'failure_indicator_IPyC/value'
  # SiC cracked IPyC failure:
  # from_reporter = 'failure_indicator_SiC_crackedIPyC/value'
  stochastic_reporter = 'constant'
  from_multi_app = sub
  sampler = sample
[]
[]
```

where $\sigma_c(\mathbf{x})$ is the stress in either the IPyC or SiC layers, σ_{ms} is the mean strength of either IPyC or SiC, m is the Weibull modulus of either IPyC or SiC, and $W_i(\mathbf{x})$ is a realization of the Weibull failure probability. $W_i(\mathbf{x})$ will be random due to the randomness in the input parameters. The mean failure probability of either the IPyC or SiC layer cracking is given by:

$$\hat{P}_f = \frac{1}{N} \sum_{i=1}^N W_i(\mathbf{x}). \quad (55)$$

The COV over the failure probability estimate is given as:

$$\hat{\delta} = \frac{1}{\hat{P}_f} \sqrt{\frac{\sum_{i=1}^N W_i(\mathbf{x})^2}{N^2} - \frac{(\hat{P}_f)^2}{N}}. \quad (56)$$

Note that, in Equations (55) and (56), unlike when using the other MC approaches, the strengths of the IPyC and SiC layers are not part of the input parameter vector \mathbf{x} .

Although the Weibull theory is computationally inexpensive for estimating failure probabilities, it does not directly provide information on the distributions of input parameters that cause IPyC and/or SiC failures. Such information can be crucial for optimizing fuel design and fabrication. Also, TRISO fuel can have other failure modes not characterized by the Weibull failure criterion. The Weibull theory cannot accommodate these additional failure criteria, unlike the other MC approaches.

C. Usage in BISON with Parallel Computing and BISON Website Documentation

To use the above-described accelerated methods for failure probability estimation in BISON, two input files are required: (1) a primary file that defines the uncertainties in the TRISO model inputs and drives the MC-type simulation, and (2) a sub file that is the TRISO model and takes the uncertain inputs from the main file. For each evaluation, the sub file returns the QoI (e.g., the layer failure indicator, layer stress and strength difference, or layer Weibull failure probability) to the main file with the aid of `transfers` in BISON. Listing 1 presents an example of this transfers block in the main file for the failure indicator of the IPyC layer. Other QoI such as the layer stress and strength difference and the layer failure probability can be transferred from the sub file to the main file in similar fashion.

1) Variance Reduction Method: Adaptive Importance Sampling

Using AIS in BISON requires defining three blocks in the main input file: (1) `Samplers`, (2) `Reporters`, and (3) `Executioner`. These three blocks are explained below.

Listing 2. The Samplers block in the main input file for defining the AIS method.

```
[Samplers]
[Sample]
  type = AdaptiveImportance
  distributions = 'normal_kernel_r normal_buffer_t normal_ipyc_t normal_sic_t normal_opyc_t uniform'
  execute_on = PRE_MULTIAPP_SETUP
  proposal_std = '1.0 1.0 1.0 1.0 1.0 1.0'
  output_limit = 0.999
  num_samples_train = 500
  std_factor = 0.9
  seed = 100
  # IPyC failure:
  initial_values = '2.1793e-04 9.42e-05 4.07e-05 3.69e-05 4.71e-05 0.05'
  # SiC cracked IPyC failure:
  # initial_values = '0.00022037925793227898 9.796957949991696e-05 4.608583870089675e-05 3.7752632994271156e-05 5.2783
  inputs_reporter = 'adaptive_MC/inputs'
[]
[]
```

The Samplers block, as presented in Listing 2, defines the AIS method and the corresponding inputs. `distributions` are the distributions of the input parameters. `proposal_std` contain the proposal standard deviations for the Markov chain for each input parameter. `output_limit` is the threshold for model failure; herein, the IPyC layer fails when its stress and strength difference exceeds zero. `num_samples_train` is the number of Markov chain samples during the training phase of AIS. `std_factor` is a factor multiplied to the standard deviation of the importance density to ensure that most samples during the evaluation phase result in model failure. A value of 0.9 is recommended. `initial_values` are the starting values for the Markov chain which should result in model failure. `inputs_reporter` is explained subsequently.

When simulating a Markov chain, a proposal step and an acceptance/rejection step are employed in simulating samples that result in model failure. The `AdaptiveMonteCarloDecision` class is a reporter class that makes the accept/reject decision based on the model output corresponding to the sample proposed by the `AdaptiveImportanceSampler` class.

In Listing 3, the Reporters block is presented. The first reporter is of type `StochasticReporter`, which stores sub application output. The second reporter is an `AdaptiveMonteCarloDecision` reporter. It takes the `output_value` from the `StochasticReporter` reporter and defines a new vector reporter called `inputs`. Furthermore, it also requires the sampler. The final reporter is of type `AdaptiveImportanceStats`, which computes statistics of interest such as the failure probability (\hat{P}_f), coefficient of variation $\hat{\delta}$, and the moments of the importance distributions (e.g., mean and standard deviation).

Listing 4 defines the Executioner block for AIS. The `num_steps` in the Executioner block below specifies the total number of samples. Of the `num_steps` samples, the first `num_samples_train` should be discarded because they are only used for constructing the importance densities. The next `num_steps - num_samples_train` should be used for estimating the failure probability.

Since the AIS method relies on a single Markov chain that must be executed sequentially, it cannot be parallelized. However, each model evaluation can be run on a set of multiple processors. More documentation on using the AIS method for TRISO failure probability estimation is provided on the BISON website at: AIS_1DTRISO.

Listing 3. The Reporters block in the main input file for using the AIS method.

```
[Reporters]
[constant]
  type = StochasticReporter
[]
[adaptive_MC]
  type = AdaptiveMonteCarloDecision
  # IPyC failure:
  output_value = constant/reporter_transfer:failure_indicator_IPyC:value
  # SiC cracked IPyC failure:
  # output_value = constant/reporter_transfer:failure_indicator_SiC_crackedIPyC:value
  inputs = 'inputs'
  sampler = sample
[]
[ais_stats]
  type = AdaptiveImportanceStats
  # IPyC failure:
  output_value = constant/reporter_transfer:failure_indicator_IPyC:value
  # SiC cracked IPyC failure:
  # output_value = constant/reporter_transfer:failure_indicator_SiC_crackedIPyC:value
  sampler = sample
[]
[]
```

Listing 4. The Executioner block in the main input file for using the AIS method.

```
[Executioner]
  type = Transient
  num_steps = 1500
[]
```

2) Variance Reduction Method: Parallel Subset Simulation

As with the AIS method, the PSS method requires defining three blocks in the main input file: (1) Samplers, (2) Reporters, and (3) Executioner. These three blocks are explained below.

In Listing 5, the PSS sampler block is presented. `distributions` are the distributions of the input parameters. `num_samplesub` is the number of samples per subset. `num_parallel_chains` is the number of Markov chains to be executed in parallel. `inputs_reporter` and `output_reporter` are the input and output values returned to the Sampler class from the Reporter class to facilitate the proposal of the next samples in the Markov chains.

Listing 5. The Samplers block in the main input file for defining the PSS method.

```
[Samplers]
[sample]
  type = ParallelSubsetSimulation
  distributions = 'normal_kernel_r normal_buffer_t normal_ipyc_t normal_sic_t normal_opyc_t uniform'
  num_samplesub = 4000
  num_parallel_chains = 5
  output_reporter = 'constant/reporter_transfer:SiC_crackedIPyC_stressminusstrength:value'
  inputs_reporter = 'adaptive_MC/inputs'
  seed = 100
  execute_on = PRE_MULTIAPP_SETUP
[]
[]
```

Listing 6. The Reporters block in the main input file for using the PSS method.

```
[Reporters]
[constant]
  type = StochasticReporter
  outputs = none
[]
[adaptive_MC]
  type = AdaptiveMonteCarloDecision
  output_value = constant/reporter_transfer:SiC_crackedIPyC_stressminusstrength:value
  inputs = 'inputs'
  sampler = sample
[]
[]
```

Listing 7. The Executioner block in the main input file for using the PSS method.

```
[Executioner]
  type = Transient
  num_steps = 3200
[]
```

When simulating a Markov chain, a proposal step and an acceptance/rejection step are employed in simulating samples that result in model failure. The `AdaptiveMonteCarloDecision` class is a Reporter class that makes the accept/reject decision based on the model output corresponding to the sample proposed by the `ParallelSubsetSimulationSampler` class.

In Listing 6, the Reporters block is presented. The first reporter is of type `StochasticReporter`, which stores sub application output. The second reporter is an `AdaptiveMonteCarloDecision` reporter. It takes the `output_value` from the `StochasticReporter` reporter and defines a new vector reporter called `inputs`. Furthermore, it also requires the `sampler`.

The `num_steps` in the Executioner block in Listing 7 specifies the total number of samples to be run per processor. This value should be equal to the `num_samplessub` in the Samplers block times the number of subsets the user desires, divided by the number of processors (or the `num_parallel_chains` in the Samplers block).

Since the PSS method relies on hundreds of independent Markov chains, it can be run in parallel on separate sets of processors. To give more information about the parallelization capability of PSS, consider that we have four subsets, each with 4000 samples. By default, BISON/MOOSE simulates 10 samples per Markov chain. Thus, each subset will have 400 (i.e., 4000/10) independent Markov chains that can be parallelized. This means, if we select 800 processors for evaluation so that each model evaluation is run by a set of two processors, each set of two processors will run 10 model evaluations (or samples) per subset. Since we have four subsets, each set of two processors will run 40 model evaluations (or samples) in total. More documentation on using the PSS method for TRISO failure probability estimation is provided on the BISON website at:

https://mooseframework.inl.gov/bison/tutorials/statistical_failure/variance_reduction/PSS_1DTRISO.html.

3) Weibull Approach

For using the Weibull approach to estimate failure probability given a set of random inputs to the TRISO model, the `WeibullFailureProbability` postprocessor should be used in the sub file. The main file will then be a MC driver that randomizes the TRISO geometry and material parameters.

Listing 8. The `WeibullFailureProbability` postprocessor block in the sub input file for using the Weibull approach. The main file will be a Monte Carlo driver that randomizes the TRISO geometry and material parameters.

```
[Weibull_failure_probability_IPyC]
  type = WeibullFailureProbability
  block = IPyC
  weibull_modulus = 6
  characteristic_strength = characteristic_strength_IPyC
[]
```

Listing 8 presents an example of this postprocessor for computing the IPyC layer failure probability. When computing the failure probability of the SiC layer, given IPyC layer cracking and using a 1-D model, the `WeibullFailureProbabilityUsingCorrelation` postprocessor must be used to account for the stress modification factors. More documentation on using the Weibull approach is provided on the BISON website at: [WeibullFailureProbability](#) and [WeibullFailureProbabilityUsingCorrelation](#).

D. Results

To demonstrate the accelerated statistical failure analysis methods implemented in BISON, we considered 1-D and 2-D versions of four TRISO models. We also considered the IPyC failure and SiC failure caused due to IPyC cracking modes. These four models differ in terms of the geometrical and material properties of the fuel and their associated uncertainties. Table VI summarizes these properties for the four TRISO models considered. The four models also differ in terms of the input irradiation temperatures, which are summarized in Table VII.

TABLE VI. Input parameters for the four TRISO models considered.

Category	Parameter	Models 1 & 2	Models 3 & 4
Particle geometry	Kernel radius (μm)	$\mathcal{N}(213.35, 4.4)$	$\mathcal{N}(212.5, 5.0)$
	Buffer thickness (μm)	$\mathcal{N}(98.9, 8.4)$	$\mathcal{N}(100.0, 10.0)$
	IPyC thickness (μm)	$\mathcal{N}(40.4, 2.5)$	$\mathcal{N}(40.0, 3.0)$
	SiC thickness (μm)	$\mathcal{N}(35.2, 1.2)$	$\mathcal{N}(35.0, 2.0)$
	OPyC thickness (μm)	$\mathcal{N}(43.4, 2.9)$	$\mathcal{N}(40.0, 3.0)$
	Asphericity ratio	1.0	1.04
Fuel properties	Kernel density (g/cm^3)	10.966	11.0
	Kernel theoretical density (g/cm^3)	11.37	11.4
	Buffer density (g/cm^3)	1.05	1.05
	Buffer theoretical density (g/cm^3)	2.25	2.25
	IPyC density (g/cm^3)	1.89	$\mathcal{N}(1.9, 0.02)$
	OPyC density (g/cm^3)	1.907	$\mathcal{N}(1.9, 0.02)$
	IPyC anisotropy factor	1.0465	$\mathcal{N}(1.05, 0.005)$
	OPyC anisotropy factor	1.0429	$\mathcal{N}(1.05, 0.005)$
Layer strengths	IPyC strength	$\mathcal{W}(\sigma_{ms}, 9.5)$	$\mathcal{W}(\sigma_{ms}, 9.5)$
	SiC strength	$\mathcal{W}(\sigma_{ms}, 6.0)$	$\mathcal{W}(\sigma_{ms}, 6.0)$

Notations: $\mathcal{N}(x, y)$: normal distribution with mean x and standard deviation y ; σ_{ms} : mean strength, which is dependent on the characteristic strength; $\mathcal{W}(\sigma_{ms}, m)$: Weibull distribution with mean strength σ_{ms} and Weibull modulus m .

TABLE VII. Irradiation temperatures in the nuclear reactor for the four TRISO fuel models.

Model 1	Model 2	Model 3	Model 4
Type = Daily varying Max. = 1226.84°C Min. = 207.4°C	Type = Daily varying Max. = 1281.84°C Min. = 195.84°C	Type = Constant Value = 700.0°C	Type = Constant Value = 1000.0°C

1) 1-D TRISO models

Table VIII summarizes the failure analysis results for the four models, considering the three accelerated methods: AIS, PSS, and the Weibull approach. For reference, the MC results are also presented. Note that the failure probability estimates computed using the accelerated methods compare satisfactorily to the MC results. Moreover, the number of model evaluations per processor using PSS and the Weibull approach are much smaller than for MC. In addition, the three accelerated methods result in a lesser COV over the failure probability estimate, as compared to MC. The PSS method was executed on 1000 processors in parallel, since it uses hundreds of Markov chains that can be run independently. The AIS method uses only a single Markov chain, and it cannot be parallelized. However, the AIS method mostly samples from the model failure region, thus it may not be necessary to run the full transient evaluation, thereby reducing the computational burden.

A by-product of the PSS method is that it can provide information on the distributions of the TRISO inputs that cause model failures. This information can be crucial for TRISO fuel design and fabrication. The other two methods (i.e., AIS and the Weibull approach) cannot provide such information. Figure 69 presents a grid plot of the TRISO-failure-causing input parameter distributions and correlations obtained using the PSS method, and compares them to the MC results for model 1. While the plot diagonals compare the kernel density distributions of PSS and MC, the off-diagonals compare the correlations of the parameters in terms of scatter plots (lower off-diagonal) and kernel contour plots (upper off-diagonal). Note that all distributions were transformed into a standard normal space using a one-to-one mapping. Overall, good agreement between the PSS and MC methods is observed.

2) 2-D TRISO models

The advantage of the PSS method and the Weibull approach is that we can directly consider 2-D models for TRISO failure evaluation. The traditional MC method can be computationally prohibitive for use with 2-D models, especially when the failure probabilities are small. Even the AIS method, which cannot be parallelized, can be computationally prohibitive with 2-D models. Table IX presents the 2-D model results considering the PSS method and the Weibull approach. For the 2-D models, there is good agreement between the failure probabilities estimated using these two methods. Also presented for comparison in Table IX are the corresponding 1-D model results. While models 1 and 2 show good agreement between the 1-D and 2-D model results compiled by both methods, models 3 and 4 seems to slightly underestimate the failure probabilities for the 1-D model in comparison to the 2-D model. Since the 1-D model approximates the IPyC and SiC layers by using stress modification factors, the quality of this approximation can influence the failure probability estimates.

As mentioned earlier, the PSS method can provide information on the distributions of the TRISO inputs that cause model failures. Since for a 2-D model, this type of information is not available from MC, due to the computational expense, Figure 70 compares the grid plot of the TRISO-failure-causing input parameter distributions and correlations obtained using the PSS method, considering 2-D and 1-D

TABLE VIII. Failure probabilities, COVs, and number of 1-D TRISO evaluations for four different statistical methods across four models.

	QoI	MC	AIS [†]	PSS	Weibull approach
Model 1 (Spherical)	\hat{P}_f	1.05×10^{-4}	1×10^{-4}	1.27×10^{-4}	1.01×10^{-4}
	$\hat{\delta}$	0.098	0.073	0.056	0.042
	N	1×10^6	1×10^4	4×10^4	100
	T^\ddagger	3.06 hrs	—	0.12 hrs	0.31 hrs
	P	1000	1	1000	1
Model 2 (Spherical)	\hat{P}_f	3.84×10^{-5}	3.29×10^{-5}	4.52×10^{-5}	3.29×10^{-5}
	$\hat{\delta}$	0.102	0.042	0.059	0.041
	N	2.5×10^6	1×10^4	4×10^4	100
	T^\ddagger	7.64 hrs	—	0.12 hrs	0.31 hrs
	P	1000	1	1000	1
Model 3 (Aspherical)	\hat{P}_f	9.26×10^{-4}	7.69×10^{-4}	8.92×10^{-4}	8.33×10^{-4}
	$\hat{\delta}$	0.085	0.073	0.052	0.045
	N	1.5×10^5	1×10^4	4×10^4	100
	T^\ddagger	0.46 hrs	—	0.12 hrs	0.31 hrs
	P	1000	1	1000	1
Model 4 (Aspherical)	\hat{P}_f	1.45×10^{-5}	1.6×10^{-5}	1.87×10^{-5}	1.39×10^{-5}
	$\hat{\delta}$	0.083	0.15	0.063	0.061
	N	1×10^7	1×10^4	4×10^4	100
	T^\ddagger	30.6 hrs	—	0.12 hrs	0.31 hrs
	P	1000	1	1000	1

Notations \hat{P}_f : failure probability estimate; $\hat{\delta}$: COV estimate; N : number of TRISO evaluations across all the processors; T : average elapsed time; and P : number of processors used

[‡] Computed by multiplying the average time for each model evaluation (i.e., 11 seconds) with the number of evaluations per processor

[†] AIS samples mostly from the model failure region, and each model evaluation takes less than the average time. These simulation times were not recorded and are hence not reported in this table.

models. Overall, there is good agreement between the 2-D and 1-D model results in both the individual parameter distributions (the diagonals in Figure 70) and their correlations (the off-diagonals in Figure 70).

E. Summary

This section discussed recently implemented methods for accelerated failure analysis of TRISO in BISON/MOOSE, their documentation on the BISON website, and application to the failure analysis of several 1-D and 2-D models. These accelerated methods included two MC variance reduction methods (i.e., AIS and PSS) and the Weibull approach. In regard to 1-D TRISO models, these accelerated methods produced failure probability estimates that compared satisfactorily to the standard MC method. In addition,

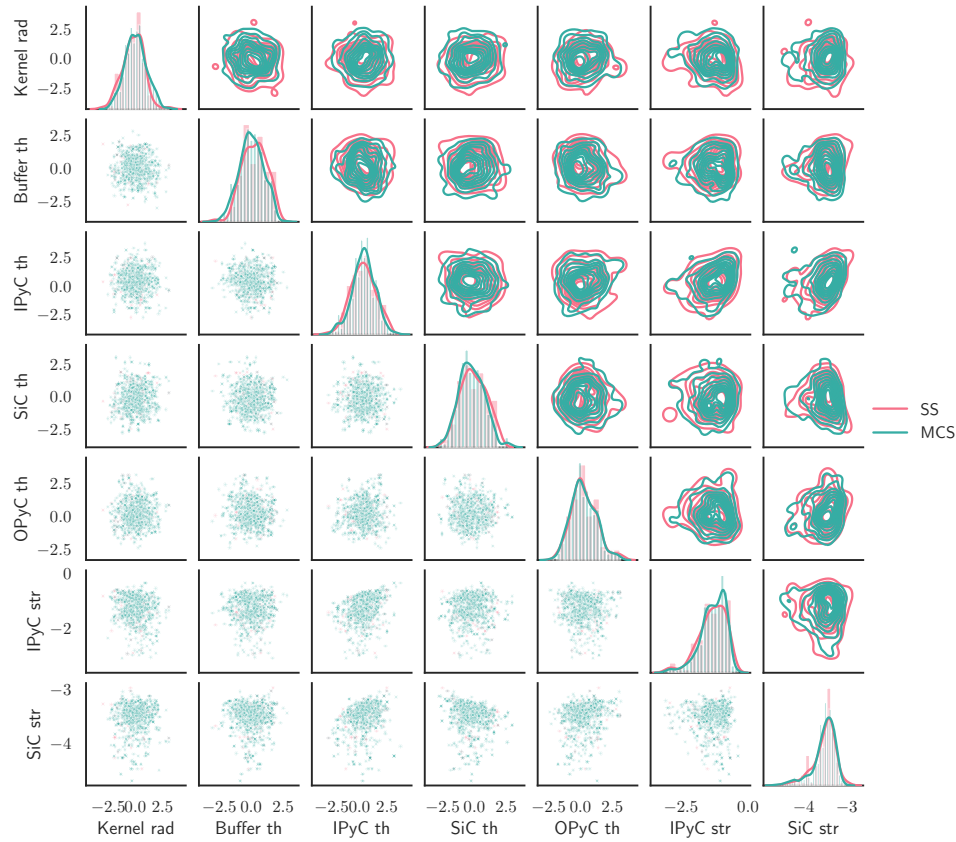


Fig. 69. Pair grid plot of failure-causing input parameter distributions for TRISO Model 1 (1-D), using the PSS and MC methods. The diagonals represent kernel densities, and the upper and lower diagonals represent kernel contour plots and scatter plots of input parameter pairs, respectively. All distributions are transformed into a standard normal space. (**Abbreviations** rad: radius; th: thickness; and str: strength)

the PSS method is capable of providing information on the distribution of the TRISO inputs that result in model failure, and this information also compared satisfactorily to MC. Moreover, the PSS method and the Weibull approach are capable of estimating failure probabilities using the 2-D model, whereas the MC method is computationally prohibitive in this case. The PSS method and Weibull approach failure probability estimations considering the 2-D model matched satisfactorily. Since PSS also characterizes the distribution of parameters that cause TRISO failures, can consider failure modes not described by the Weibull criterion, and is amenable to massively parallel computing, it may, in practice, be preferred over the other methods. Future work includes investigation of the influence anisotropy in the particle layers on the failure probability estimates, and the use of active learning—studied in Dhulipala et al. (2022c,d)—for even more computational gains when estimating the failure probabilities.

TABLE IX. Failure probabilities, COVs, and number of 2-D TRISO evaluations for the PSS and Weibull methods across four models. The corresponding 1-D model results are also presented for comparison.

	QoI	PSS	Weibull approach	PSS	Weibull approach
		2-D TRISO model		1-D TRISO model	
Model 1 (Spherical)	\hat{P}_f	1.19×10^{-4}	0.99×10^{-4}	1.27×10^{-4}	1.01×10^{-4}
	$\hat{\delta}$	0.055	0.04	0.056	0.042
	N	5×10^4	200	4×10^4	100
	T^\dagger	27.5 hrs	27.5 hrs	0.12 hrs	0.31 hrs
	P	1000	4	1000	1
Model 2 (Spherical)	\hat{P}_f	3.4×10^{-5}	5.86×10^{-5}	4.52×10^{-5}	3.29×10^{-5}
	$\hat{\delta}$	0.06	0.041	0.059	0.041
	N	5×10^4	200	4×10^4	100
	T^\dagger	27.5 hrs	27.5 hrs	0.12 hrs	0.31 hrs
	P	1000	4	1000	1
Model 3 (Aspherical)	\hat{P}_f	2.49×10^{-3}	2.42×10^{-3}	0.89×10^{-3}	0.83×10^{-3}
	$\hat{\delta}$	0.045	0.052	0.052	0.045
	N	4×10^4	200	4×10^4	100
	T^\dagger	22 hrs	27.5 hrs	0.12 hrs	0.31 hrs
	P	1000	4	1000	1
Model 4 (Aspherical)	\hat{P}_f	3.75×10^{-5}	3.84×10^{-5}	1.87×10^{-5}	1.39×10^{-5}
	$\hat{\delta}$	0.067	0.055	0.063	0.061
	N	5×10^4	200	4×10^4	100
	T^\dagger	27.5 hrs	27.5 hrs	0.12 hrs	0.31 hrs
	P	1000	4	1000	1

Notations \hat{P}_f : failure probability estimate; $\hat{\delta}$: COV estimate; N : number of TRISO evaluations across all the processors; and P : number of processors used

† Parallel computing was used

‡ Computed by multiplying the average time for each model evaluation (i.e., 33 minutes) with the number of evaluations per processor

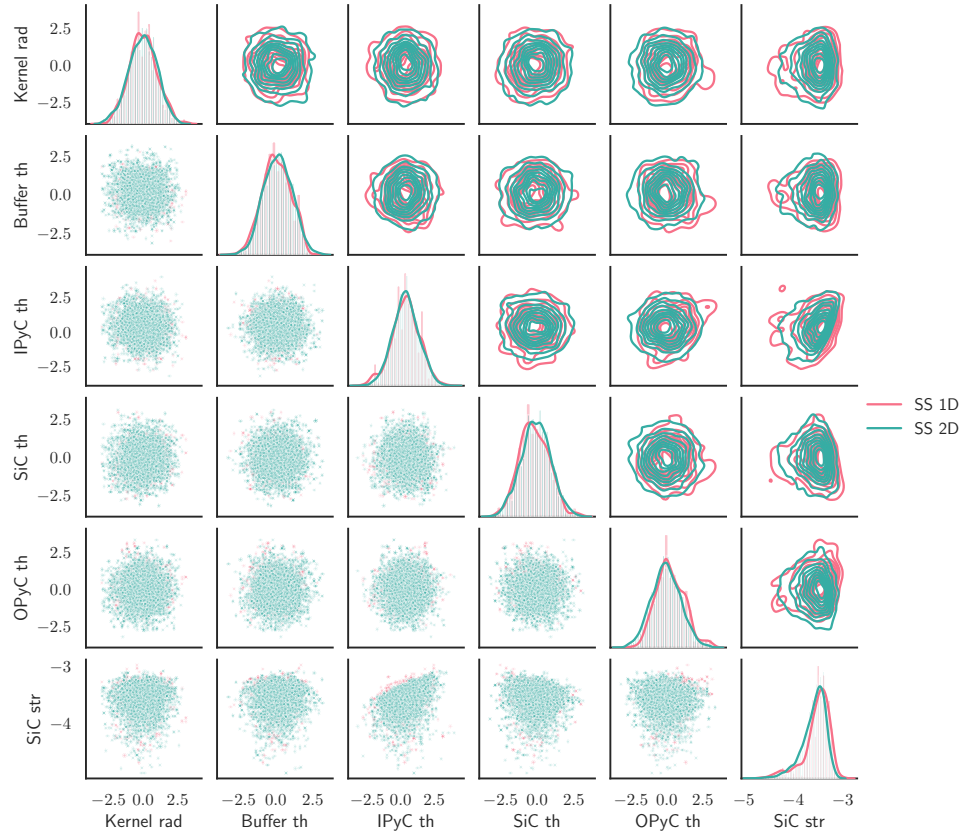


Fig. 70. Pair grid plots of the SiC failure conditional on IPyC distributions of failure-causing input parameters for TRISO Model 1, in light of PSS for 1-D and 2-D models. The diagonals represent kernel densities, and the upper and lower diagonals represent kernel contour plots and scatter plots of input parameter pairs, respectively. All distributions are transformed into a standard normal space. (**Abbreviations** rad: radius; th: thickness; and str: strength)

VIII. CONCLUSION

The capabilities of BISON were significantly expanded to enable it to model the fission product diffusion in TRISO particles and the matrix. First, the ability to model anisotropic thermal behavior and diffusion was developed in BISON. Specifically, this capability enables users to define the thermal conductivity and diffusion coefficient as a second-order tensor whose components correspond to the magnitude in the radial and tangential directions. This capability was demonstrated via analyses conducted on both spherical and aspherical TRISO particles. Next, code verification was performed on 1-D spatiotemporal problems, evaluating the conservation of fission product species. The BISON predictions agree well with the analytical results in terms of concentration profiles, release rate and R/B, and fractional release from a solid sphere under in-pile conditions for both decaying and stable fission products, and under out-of-pile conditions for the preexisting isotopes. These verification problems were made available in the BISON verification test suite and can be found within the BISON verification documentation. Next, the availability and reliability of diffusion coefficients were investigated for key radioactive species in the particle. The diffusion coefficients were estimated based on the AGR-1 and -2 experiments during both base irradiation and safety heating tests. The estimated diffusion coefficients and surveyed empirical coefficients of the key radioactive species in the kernel, PyC, and SiC layers were provided. In addition, homogenization was performed on a compact level to calculate fission product diffusivity. The homogenized diffusivity can be used to model fission product diffusion with source terms calculated from a MC particle simulation. A two-way coupling capability was developed to transfer the compact temperature to each particle, based on their spatial location. The compact modeling was applied to the AGR-1 and 3/4 experiments and the model's predictions were compared against the PIE measurements. Finally, recently implemented methods for conducting accelerated failure analysis of TRISO was documented online. Application of these methods to the failure analysis of several 1-D and 2-D models were provided as examples on the BISON website.

REFERENCES

- W. Amian and D. Stöver. Diffusion of silver and cesium in silicon-carbide coatings of fuel particles for high-temperature gas-cooled reactors. *Nucl. Technol.*, 61(3):475–486, 1983. doi:10.13182/NT61-475.
- W. Amian et al. Results of fission product and actinide studies in coated fuel particles and matrix graphite. In *Gas-cooled reactors today, Proceedings of the British Nuclear Energy Society Conference*, pages 153–160, London, 1982.
- S. K. Au and J. L. Beck. A new adaptive importance sampling scheme for reliability calculations. *Struct. Saf.*, 21(2):135–158, 1999. doi:10.1016/S0167-4730(99)00014-4.
- S. K. Au and J. L. Beck. Estimation of small failure probabilities in high dimensions by subset simulation. *Probabilistic Eng. Mech.*, 16(4):263–277, 2001. doi:10.1016/S0266-8920(01)00019-4.
- C. A Baldwin, J. D. Hunn, R. N. Morris, F. C. Montgomery, C. M. Silva, and P. A. Demkowicz. First elevated-temperature performance testing of coated particle fuel compacts from the AGR-1 irradiation experiment. *Nucl. Eng.*, 271:131–141, 2014. doi:10.1016/j.nucengdes.2013.11.021.
- P. E. Brown and R. L. Faircloth. Metal fission product behaviour in high temperature reactors – UO₂ coated particle fuel. *J. Nucl. Mater.*, 59(1):29–41, 1976. doi:10.1016/0022-3115(76)90005-2.
- D. A. G. Bruggeman. Berechnung verschiedener physikalischer konstanten von heterogenen substanzen. i. dielektrizitätskonstanten und leitfähigkeiten der mischkörper aus isotropen substanzen. *Annalen der Physik*, 416(7):636–664, 1935. doi:10.1002/andp.19354160705.
- R. E. Bullock. Fission-product release during postirradiation annealing of several types of coated fuel particles. *J. Nucl. Mater.*, 125(3):304–319, 1984. doi:10.1016/0022-3115(84)90558-0.
- A. S. Chernikov et al. Fission product diffusion in fuel element materials for HTGR. In *Fission product release and transport in gas-cooled reactors, Proceedings of the IAEA specialists meeting*, pages 170–181, Vienna, 1985.
- A. Christ. Nachrechnung von ausheizexperimenten. Technical Note HBK-5125-BF-GHRA 001555, HRB Mannheim, Research Center Jülich, 1985.
- B. P. Collin. AGR-1 irradiation test final as-run report. Tech. Rep. INL/EXT-10-18097, Revision 3, INL, Idaho Falls, ID (United States), 1 2015.
- B. P. Collin. Diffusivities of Ag, Cs, Sr, and Kr in TRISO fuel particles and graphite. Tech. Rep. INL/EXT-16-39548, INL, Idaho Falls, ID United States, 9 2016. URL <https://inldigitallibrary.inl.gov/sites/sti/sti/7245704.pdf>.
- B. P. Collin. AGR-2 irradiation test final as-run report. Tech. Rep. INL/EXT-14-32277, Revision 4, INL, Idaho Falls, ID (United States), 2 2018.
- B. P. Collin, D. A. Petti, P. A. Demkowicz, and J. T. Maki. Comparison of fission product release predictions using perfume with results from the AGR-1 safety tests. *Nucl. Eng.*, 301:378–390, 2016. doi:10.1016/j.nucengdes.2016.03.023.
- P. A. Demkowicz, D. V Laug, D. M Scates, E. L. Reber, L. G. Roybal, J. B. Walter, J. M. Harp, and R. N. Morris. The fuel accident condition simulator (FACS) furnace system for high temperature performance testing of VHTR fuel. *Nucl. Eng.*, 251:164–172, 2012. doi:10.1016/j.nucengdes.2011.10.048.
- F. Deng and Q. Zheng. Interaction models for effective thermal and electric conductivities of carbon nanotube composites. *Acta Mech. Solida Sin.*, 22(1):1–17, 2009. doi:10.1016/S0894-9166(09)60085-9.
- S. L. N. Dhulipala, W. Jiang, B. W. Spencer, J. D. Hales, M. D. Shields, A. E. Slaughter, Z. M. Prince, V. M. Labouré, C. Bolisetti, and P. Chakroborty. Accelerated statistical failure analysis of multifidelity

- TRISO fuel models. *J. Nucl. Mater.*, 563:153604, 2022a. doi:10.1016/j.jnucmat.2022.153604.
- S. L. N. Dhulipala, Z. M. Prince, A. E. Slaughter, L. B. Munday, W. Jiang, B. W. Spencer, and J. D. Hales. Monte carlo variance reduction in MOOSE stochastic tools module: accelerating the failure analysis of nuclear reactor technologies. In *ANS International Conference on Physics of Reactors*, Pittsburgh, PA United States, May 15-20 2022b.
- S. L. N. Dhulipala, M. D. Shields, P. Chakroborty, W. Jiang, B. W. Spencer, J. D. Hales, V. M. Labouré, Z. M. Prince, C. Bolisetti, and Y. Che. Reliability estimation of an advanced nuclear fuel using coupled active learning, multifidelity modeling, and subset simulation. *Reliab. Eng. Syst.*, 226:108693, 2022c. doi:10.1016/j.ress.2022.108693.
- S. L. N. Dhulipala, M. D. Shields, B. W. Spencer, C. Bolisetti, A. E. Salugther, V. M. Labouré, and P. Chakroborty. Active learning with multifidelity modeling for efficient rare event simulation. *J. Comput. Phys.*, 468:111506, 2022d. doi:10.1016/j.jcp.2022.111506.
- EPRI. Uranium oxycarbide (UCO) tristructural isotropic (TRISO) coated particle fuel performance. Topical Report EPRI-AR-1(NP), EPRI, 5 2019. URL <https://www.nrc.gov/docs/ML1915/ML19155A173.pdf>.
- J. A. Evans, R. A. Lebensohn, J. R. Harter, and K. D. Weaver. Anisotropic temperature-dependent elastic constants and thermal conductivities of TRISO particle coatings. *J. Nucl. Mater.*, 565:153718, 2022. doi:10.1016/j.jnucmat.2022.153718.
- R. Förthmann and E. Gyarmati. Investigations on the transport behaviour of strontium in coated particles at high temperatures. *J. Nucl. Mater.*, 58(2):189–195, 1975. doi:10.1016/0022-3115(75)90105-1.
- E. Friedland, J.B. Malherbe, N.G. van der Berg, T. Hlatshwayo, A.J. Botha, E. Wendler, and W. Wesch. Study of silver diffusion in silicon carbide. *J. Nucl. Mater.*, 389(2):326–331, 2009. ISSN 0022-3115. doi:10.1016/j.jnucmat.2009.02.022.
- E. Friedland, N.G. van der Berg, J.B. Malherbe, J.J. Hancke, J. Barry, E. Wendler, and W. Wesch. Investigation of silver and iodine transport through silicon carbide layers prepared for nuclear fuel element cladding. *J. Nucl. Mater.*, 410(1):24–31, 2011. doi:10.1016/j.jnucmat.2010.12.243.
- K. Fukuda and K. Iwamoto. Diffusion and evaporation of fission products in coated fuel particles. *J. Nucl. Sci. Technol.*, 12(3):181–189, 1975. doi:10.1080/18811248.1975.9733088.
- K. Fukuda and K. Iwamoto. Xenon diffusion behaviour in pyrolytic SiC. *J. Mater. Sci.*, 11:522–528, 1976. doi:10.1007/BF00540933.
- K. Fukuda and K. Iwamoto. Diffusion behavior of fission product in pyrolytic silicon carbide. *J. Nucl. Mater.*, 75(1):131–144, 1978. doi:10.1016/0022-3115(78)90037-5.
- K. Fukuda et al. Research and development of HTGR fuels. Report M-89-007, Japan Atomic Energy Research Institute, 1989.
- F. Gao and L. Han. Implementing the Nelder-Mead simplex algorithm with adaptive parameters. *Comput. Optim. Appl.*, 51(1):259–277, 2012. doi:10.1007/s10589-010-9329-3.
- P. E. Gethard and L. R. Zumwalt. Diffusion of metallic fission products in pyrolytic carbon. *Nuclear Applications*, 3(11):679–685, 1967. doi:10.13182/NT67-A27903.
- D. T. Goodin and H. Nabielek. The performance of HTR fuel in accidents. Technical Note KFA-HBK-TN-19/85, Research Center Jülich, 1985.
- A. N. Gudkov et al. Behavior of solid fission products in coated fuel particles of a high-temperature gas-cooled reactor. *Atomnaya Energiya*, 67:93–97, 1989.
- J. D. Hales, S. R. Novascone, B. W. Spencer, R. L. Williamson, G. Pastore, and D. M.

- Perez. Verification of the BISON fuel performance code. *Ann. Nucl. Energy*, 71:81–90, 2014. doi:10.1016/j.anucene.2014.03.027.
- J. D. Hales, W. Jiang, A. Toptan, and K. A. Gamble. BISON TRISO modeling advancements and validation to AGR-1 data. Tech. Rep. EXT-20-00297, INL, 7 2020.
- J. D. Hales, W. Jiang, A. Toptan, and K. A. Gamble. Modeling fission product diffusion in TRISO fuel particles with BISON. *J. Nucl. Mater.*, 548:152840, 2021. doi:10.1016/j.jnucmat.2021.152840.
- J. D. Hales, A. Toptan, W. Jiang, and B. W. Spencer. Numerical evaluation of AGR-2 fission product release. *J. Nucl. Mater.*, 558:153325, 2022. doi:10.1016/j.jnucmat.2021.153325.
- K. Hayashi and K. Fukuda. Diffusion coefficients of fission products in the UO_2 kernel and pyrocarbon layer of BISO-coated fuel particles at extremely high temperatures. *J. Nucl. Mater.*, 174(1):35–44, 1990. doi:10.1016/0022-3115(90)90418-M.
- R. G. Hills, W. R. Witkowski, W. J. Rider, T. G. Trucano, and A. Urbina. Development of a fourth generation predictive capability maturity model. Technical Report SAND2013-8051, Sandia National Laboratories, Albuquerque, NM United States, 2013.
- W. Jiang, J. D. Hales, B. W. Spencer, B. P. Collin, A. E. Slaughter, S. R. Novascone, A. Toptan, K. A. Gamble, and R. Gardner. TRISO particle fuel performance and failure analysis with BISON. *J. Nucl. Mater.*, 548:152795, 2021a. doi:10.1016/j.jnucmat.2021.152795.
- W. Jiang, G. Singh, J. D. Hales, A. Toptan, B. W. Spencer, and S. R. Novascone. Efficient failure probability calculations and modeling interface debonding in TRISO particles with BISON. Tech. Rep. INL/EXT-21-64589, INL, Idaho Falls, ID (United States), 9 2021b.
- W. Jiang, A. Toptan, J. D. Hales, B. W. Spencer, A. Casagrande, and S. R. Novascone. Fission product transport in TRISO particles and pebbles. Tech. Rep. INL/EXT-21-63549, INL, United States, 6 2021c.
- W. Jiang, G. Singh, J. D. Hales, A. Toptan, B. W. Spencer, S. R. Novascone, S. L. N. Dhulipala, and Z. M. Prince. Efficient high-fidelity TRISO statistical failure analysis using bison: Applications to AGR-2 irradiation testing. *J. Nucl. Mater.*, 562:153585, 2022. doi:10.1016/j.jnucmat.2022.153585.
- K. M. Kalayeh, J. S. Graf, and M. K. Gobbart. Fem convergence for pdes with point sources in 2-d and 3-d. URL http://hpcf-files.umbc.edu/research/papers/PointSource_COMSOL2015.pdf.
- J. J. Kane, D. W. Marshall, N. L. Cordes, W. C. Chuirazzi, B. Kombaiyah, I. van Rooyen, and J. D. Stempien. 3D analysis of TRISO fuel compacts via X-ray computed tomography. *J. Nucl. Mater.*, 565: 153745, 2022. doi:10.1016/j.jnucmat.2022.153745.
- E. López-Honorato, P. J. Meadows, and P. Xiao. Fluidized bed chemical vapor deposition of pyrolytic carbon—I. Effect of deposition conditions on microstructure. *Carbon*, 47(2):396–410, 2009. doi:10.1016/j.carbon.2008.10.023.
- E. López-Honorato, D. Yang, J. Tan, P. J. Meadows, and P. Xiao. Silver diffusion in coated fuel particles. *J. Am. Ceram. Soc.*, 93(10):3076–3079, 2010. doi:10.1111/j.1551-2916.2010.04055.x.
- P. J. Meadows, E. López-Honorato, and P. Xiao. Fluidized bed chemical vapor deposition of pyrolytic carbon—II. Effect of deposition conditions on anisotropy. *Carbon*, 47(1):251–262, 2009. doi:10.1016/j.carbon.2008.10.003.
- K. Minato, T. Ogawa, K. Fukuda, H. Sekino, H. Miyanishi, S. Kado, and I. Takahashi. Release behavior of metallic fission products from HTGR fuel particles at 1600 to 1900°C. *J. Nucl. Mater.*, 202(1): 47–53, 1993. doi:10.1016/0022-3115(93)90027-V.
- R. Moormann and K. Verfondern. Methodik umfassender probabilistischer Sicherheitsanalysen für zukünftige HTR-Anlagenkonzepte – Ein Statusbericht (Stand 1986), Band 3: Spaltproduktfreisetzung.

- Tech. Rep. Jül-Spez-388/Bd.3, Research Center Jülich, 1987.
- R. N. Morris, C. A. Baldwin, P. A. Demkowicz, J. D. Hunn, and E. L. Reber. Performance of AGR-1 high-temperature reactor fuel during post-irradiation heating tests. *Nucl. Eng. Des.*, 306:24–35, 2016. doi:10.1016/j.nucengdes.2016.04.031.
- D. Mu, ZS. Liu, C. Haung, and N. Djilali. Prediction of the effective diffusion coefficient in random porous media using the finite element method. *J. Porous Mater.*, 14:49–54, 2007. doi:10.1007/s10934-006-9007-0.
- A. Müller. Freisetzung gasförmiger spaltprodukte (Kr, Xe, J) aus brennelementen für gasgekühlte hochtemperaturreaktoren. Report, Research Center Jülich, 1976.
- B. F. Myers. Cesium diffusion in silicon carbide during post irradiation anneals. Technical Note KFA-HBK-TN-01/84, Research Center Jülich, 1984.
- B. F. Myers. Fuel design data manual. Technical Report 901866, Issue F, General Atomics, 1987.
- B. F. Myers and W. E. Bell. Strontium transport data for HTGR systems. Report GA-A13168, General Atomic Company, 1974.
- B. F. Myers and W. E. Bell. Cesium transport data for HTGR systems. Report GA-A13990, General Atomic Company, 1979.
- H. Nabielek, H. Hick, M. Wagner-Löffler, and E. H. Voice. Performance limits of coated particle fuel, Part III: Fission product migration in HTR fuel. Tech. Rep. DP-Report-828(Pt.3), O.E.C.D High Temperature Reactor Project Dragon, 6 1974.
- H. Nabielek, P. E. Brown, and P. Offermann. Silver release from coated particle fuel. *Nucl. Technol.*, 35 (2):483–493, 1977. doi:10.13182/NT35-483.
- National Research Council. *Assessing the Reliability of Complex Models*. The National Academies Press, Washington, DC United States, 2012.
- J. A. Nelder and R. Mead. A simplex method for function minimization. *The Computer Journal*, 7(4): 308–313, 1965. doi:10.1093/comjnl/7.4.308.
- L. E. Nielsen. The thermal and electrical conductivity of two-phase systems. *Ind. Eng. Chem. Fundam.*, 13(1):17–20, 1974. doi:10.1021/i160049a004.
- W. L. Oberkampf and C. J. Roy. *Verification and Validation in Scientific Computing*. Cambridge University Press, Cambridge, UK, first edition, 11 2010.
- W. L. Oberkampf, M. Pilch, and T. G. Trucano. Predictive capability maturity model for computational modeling and simulation. Technical Report SAND2007-5948, Sandia National Laboratories (SNL), Albuquerque, NM United States, 2007.
- P. Offermann. Ag-diffusion in PyC. *J. Nucl. Mater.*, 64(3):249–253, 1977. doi:10.1016/0022-3115(77)90076-9.
- T. Ogawa, K. Fukuda, and S. Kashimura. Release of metal fission products from coated particle fuel - Swept-gas capsule 74F9J, 75F4A and 75F5A. Report M-85-041, Japan Atomic Energy Research Institute, 1985.
- N. W. Porter. *Development of a Novel Residual Formulation of CTF and Application of Parameter Estimation Techniques*. PhD thesis, North Carolina State University, Nuclear Engineering Department, 2018.
- P. J. Roache. *Verification and Validation in Computational Science and Engineering*. Hermosa Publishing, 1998.
- S. B. Seo, N. R. Brown, G. Pastore, and B. D. Wirth. Systematic sensitivity analysis of Ag release from

- TRISO particle during AGR-1 irradiation test and high temperature annealing safety test. *J. Nucl. Mater.*, 558:153346, 2022. doi:10.1016/j.jnucmat.2021.153346.
- P.-C.A. Simon, L. K. Agesen, C. Jiang, W. Jiang, and J.-H. Ke. Mechanistic calculation of the effective silver diffusion coefficient in polycrystalline silicon carbide: Application to silver release in AGR-1 TRISO particles. *J. Nucl. Mater.*, 563:153669, 2022. ISSN 0022-3115. doi:10.1016/j.jnucmat.2022.153669.
- W. F. Skerjanc and W. Jiang. Bison as-run agr-3/4 irradiation test predictions. Tech. Rep. INL/EXT-21-65160, INL, Idaho Falls, ID (United States), 11 2021.
- W. F. Skerjanc and W. Jiang. Comparison of fission product release predictions using PARFUME and BISON with results from the AGR-3/4 irradiation experiment. Tech. Rep. INL/RPT-22-69003, INL, Idaho Falls, ID (United States), 9 2022.
- A. Toptan. *A Novel Approach to Improve Transient Fuel Performance Modeling in Multi-Physics Calculations*. PhD thesis, North Carolina State University, Nuclear Engineering Department, 2019.
- A. Toptan, D J Kropaczek, and M N Avramova. On the validity of dilute gas assumption for gap conductance calculations in nuclear fuel performance codes. *Nucl. Eng. Des.*, 350:1–8, 2019. doi:10.1016/j.nucengdes.2019.04.042.
- A. Toptan, N. W. Porter, J. D. Hales, B. W. Spencer, M. Pilch, and R. L. Williamson. Construction of a code verification matrix for heat conduction with finite element code applications. *J. Verif. Valid. Uncertain. Quantif.*, 5(4), 11 2020a. doi:10.1115/1.4049037.
- A. Toptan, N. W. Porter, J. D. Hales, R. L. Williamson, and M. Pilch. FY20 verification of BISON using analytic and manufactured solutions. Tech. Rep. CASL-U-2020-1939-000; SAND2020-3887R, CASL, Albuquerque, NM United States, 3 2020b.
- A. Toptan, W. Jiang, J. D. Hales, B. W. Spencer, A. Casagrande, and S. R. Novascone. FEA-aided investigation of the effective thermal conductivity in a medium with embedded spheres. *Nucl. Eng. Des.*, 381:111355, 2021. doi:10.1016/j.nucengdes.2021.111355.
- A. Toptan, W. Jiang, and J. D. Hales. Analytical homogenization techniques applied to the fickian diffusion: Effective diffusivity coefficient. In *ANS Winter Meeting and Technology Expo: Materials Science and Technology (MSTD), Nuclear Fuels*, Phoenix, AZ United States, November 13-17 2022a.
- A. Toptan, N. W. Porter, J. D. Hales, W. Jiang, B. W. Spencer, and S. R. Novascone. Verification of MOOSE/Bison’s heat conduction solver using combined spatiotemporal convergence analysis. *J. Verif. Valid. Uncertain. Quantif.*, 7(2):021006, 2022b. doi:10.1115/1.4054216.
- A. Toptan, W. Jiang, J. D. Hales, B. W. Spencer, and S. Novascone. Verification of Bison fission product species conservation under TRISO reactor conditions. *J. Nucl. Mater.*, page 154105, 2023. doi:10.1016/j.jnucmat.2022.154105.
- J. J. van der Merwe. Evaluation of silver transport through SiC during the German HTR fuel program. *J. Nucl. Mater.*, 395(1):99–111, 2009. doi:10.1016/j.jnucmat.2009.09.024.
- K. Verfondern and D. Müller. FRESCO-II, program zur berechnung der spaltproduktfreisetzung aus einem HTR-brennelement im normalbetrieb (bestrahlungsexperiment) und kernaufheizstörfall (heizexperiment) – benutzerhandbuch. Internal Report KFA-ISR-IB-4/91, Research Center Jülich, 1991.
- Y. Wang, D. H. Hurley, E. P. Luther, M. F. Beaux II, D. R. Vodnik, R. J. Peterson, B. L. Bennett, I. O. Usov, P. Yuan, X. Wang, and M. Khafizov. Characterization of ultralow thermal conductivity in anisotropic pyrolytic carbon coating for thermal management applications. *Carbon*, 129:476–485, 2018. doi:10.1016/j.carbon.2017.12.041.

- R. L. Williamson, J. D. Hales, S. R. Novascone, G. Pastore, K. A. Gamble, B. W. Spencer, W. Jiang, S. A. Pitts, A. Casagrande, D. Schwen, A.X. Zabriskie, A. Toptan, R. Gardner, C. Matthews, W. Liu, and H. Chen. BISON: A flexible code for advanced simulation of the performance of multiple nuclear fuel forms. *Nucl. Technol.*, 207(7):954–980, 2021. doi:10.1080/00295450.2020.1836940.
- M. Wright. Direct search methods: Once scorned, now respectable, in numerical analysis. In *Proceedings of the 1995 Dundee Biennial Conference in Numerical Analysis* (Eds. D. F. Griffiths and G. A. Watson), pages 191–208, Addison Wesley Longman, Harlow, UK, 1996.
- H. Zhang, E. López-Honorato, and P. Xiao. Fluidized bed chemical vapor deposition of pyrolytic carbon-III. Relationship between microstructure and mechanical properties. *Carbon*, 91:346–357, 2015. doi:10.1016/j.carbon.2015.05.009.